Damage Evolution and Characterization of SiC/SiC Ceramic Matrix Composites using Micro-Computed Tomography Techniques

by

Ashley Hilmas

A dissertation submitted in partial fulfillment
of the requirements for the degree of
Doctor of Philosophy
(Materials Science and Engineering)
in the University of Michigan
2020

Doctoral Committee:

Professor John Halloran, Co-Chair
Dr. Kathleen Sevener, Co-Chair
Professor Ashwin Shahani
Professor Michael Thouless

Ashley Hilmas
amhilmas@umich.edu
ORCID iD: 0000-0001-7323-1588

Dedication

“Love for all who have love for all” – Stephen Jackson

Acknowledgements

Wow.. It's been four and a half years. It feels liked just yesterday that I left the comfort of my well acquainted hometown and home of my undergraduate alma mater of Rolla, Missouri and decided to return to my birthplace of Ann Arbor, Michigan. Throughout my years at the University of Michigan I have grown immensely as a scientist, an engineer, a leader, and a person due to the encouragement and support of my mentors, friends, and colleagues.

First, I would like to start by saying thank you to my co-advisors Professor John Halloran and Dr. Kathleen Sevener. John instantly welcome me to Ann Arbor and his limitless guidance made me a better scientist/engineer and for this I am grateful. Our conversations about ceramic materials and Rolla bond will forever be fond memories. I would almost definitely not be completing this journey if it were not for the support and guidance of Kathy. There was a time when I was unsure of my future but Kathy was also available for the difficult conversations and continually pushed me to better myself. I truly will never be able to thank you!

Second, I would like to give a special acknowledgement to graduate coordinator Renee Hilgendorf. She does so much for the department and I honestly don't know where I would've been without her knowledge and guidance.

Third, I would like to acknowledge all of the organizations and groups I have been a part throughout the last four years for supporting me in my graduate school endeavors. I would like to especially acknowledge the American Ceramics Society ACerS President's Council of Student Advisors, PCSA (I did not invent these acronyms). This organization not only offered opportunities for me to grow within my technical field but it introduced me to so many people who I have grown so close with. Special acknowledgements to my PCSA baes: Victoria Christensen, Chris Kassner, Lavina Backman, and Scotty McCormack. I would also like to thank Lisa Rueschhoff who I have become so close with for her constant advice and guidance.

Fourth, I have to acknowledge all of the friendships I made in Ann Arbor both within and outside of the department. To my girls: Lauren, Lori, and Kelsey, thanks for all of the fun memories, I will forever cherish the memories we made! Kathleen, thank you for always being there to discuss research, grab a beer, or just relax. To Sid and Brain, the crew. We had so much together and I will always remember our adventures. My cubicle buddy and pseudo lab-mate, Maya, I appreciate for your continued guidance and advice. I could always count on you to brighten my day! Avi, thank you for constantly being someone I could come talk to. To everyone at the wolverine den: thank you for being my home away from home. I will be back for football games.

Last, but certainly not least, my family. I truly do not have the words to thank you for your unconditional love and support. I would not be the person I am today if it were not for each and every one of you.

Table of Contents

List of Figures

List of Tables

List of Equations

List of Acronyms and Symbols

E_c: Elastic modulus of the composite
E_f: Elastic modulus of the fiber
E_m: Elastic modulus of the matrix
E_L: Elastic modulus of the longitudinal ply
E_T: Elastic modulus of the transverse ply
I: intensity transmitted through the specimen
I_0: specific incident x-ray intensity
ℓ: debond length
m: Weibull modulus
r: fiber radius
S_c: characteristic strength
t: thickness
v_f: volume fraction of fiber
v_m: volume fraction of matrix
z: distance
Γ_d: debonding toughness
Γ_m: matrix toughness
σ: applied composite stress
σ_d: debonding stress
σ_f: stress in the fiber
σ_m: stress in the matrix
σ_r: residual stress
μ: x-ray attenuation coefficient
τ: interfacial sliding stress

Abstract

In situ x-ray computed tomography was performed on melt infiltrated (MI) SiC/SiC ceramic matrix composites under tension in order to observe and quantify damage progression. The advanced light source (ALS) at Lawrence Berkeley National Lab was utilized to test two types of composite architectures, unidirectional and cross-ply, where each specimen was imaged at increasing tensile stress increments. Damage such as matrix cracking and fiber fragmentations were detected and measured for each specimen at each imaged stress increment. From the x-ray tomography observations, three different types of matrix cracks were observed including partial cracking, bifurcating cracks, and joining cracks. The onset of matrix cracking that was observed using in situ x-ray computed tomography was compared to mechanical model predictions. The comparison between the experimental observations and the mechanical models were similar, within the range of 100 MPa. The final matrix crack spacing was also compared to predicted debond lengths and shear lag distances. Fiber fragmentations were observed within the volume of each specimen and the breaks were quantified. The number of fiber fragmentations within a composite specimen continued to increase until the specimen broke. The opening height of each fiber fragmentation was qualitatively examined and two main observations were determined. First, as applied stress continued to increase, the initial fiber fragmentation opening also continued to increase. Second, fiber fragmentations that occurred at higher applied stresses have larger fiber fragmentation openings than ones that occurred at lower stresses. Using x-ray computed tomography allowed for the study of the relationship between fiber damage and the microstructure in terms of fiber locations and fiber clustering.

Chapter I. Introduction

1.1 Introduction to Ceramic Matrix Composites

Ceramic materials often have high elastic moduli, exhibit high hardness, good chemical resistance and the ability to maintain properties at high temperatures and are therefore often utilized within the aerospace industry. Ceramic matrix composites (CMCs) are ceramic materials that exhibit higher toughness when compared to monolithic ceramic materials due to the addition of reinforcements usually in the form of fibers. Different types of reinforcements that could potentially be used for ceramic composites include particulates, short fibers or whiskers, and continuous fibers. All of these types of reinforcements can be made out of a variety of different ceramic materials depending on what the CMC is going to be utilized for.[1-2] In addition to the variety of types of fibers, there are also many ways the fibers can be oriented, i.e., randomly dispersed, unidirectional (all fibers oriented in one direction, usually parallel to the loading direction), 45° angled plies, alternating 0°/90° plies, and woven composites are just a few ways the fiber architecture can be laid up to form a full composite. This work will focus on laminated unidirectional and alternating 0°/90° cross-ply SiC/SiC ceramic matrix composites comprised of a dense silicon carbide matrix reinforced with continuous SiC fibers utilized for the hot section in gas turbine engines. An image depicting the cross-section of both a unidirectional and cross-ply SiC/SiC CMC specimen using x-ray computed tomography is shown in Figures 1.1a and 1.1b respectively.

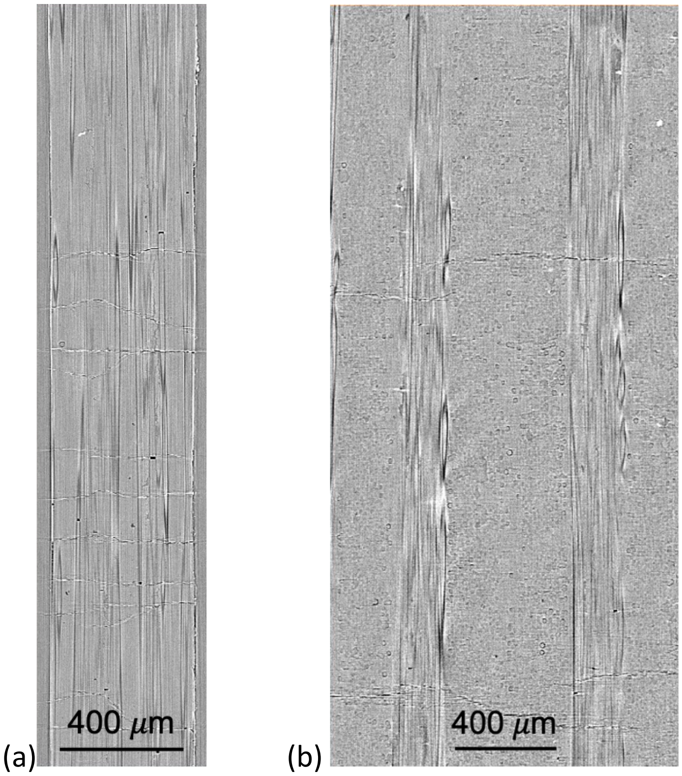

Figure 1.1 2D slices taken within the 3D volume of (a) a unidirectional specimen with fibers running parallel to the loading direction 0° and (b) 2D image of a cross-ply specimen [0°/90°]s symmetric around a matrix rich region. There are a total of 8 plies with alternation 0°/90° plies with the 0° degree plies parallel to the tensile loading direction and the 90° degree plies perpendicular to the loading direction

SiC/SiC CMCs have impressive properties such as high temperature strength, creep resistance, low porosity, low density, high thermal conductivity and low thermal expansion that make them particularly suited for use in gas turbine engines.[3-9] The use of ceramic composites in gas turbine engines results in a decrease in the required cooling flow and therefore an increase in overall efficiency. GE aviation is currently using SiC/SiC CMCs (HiPerComp^{TM}) for static parts in their LEAP engine which has shown a fuel burn reduction of 2%. Using SiC/SiC composite parts that have a lower density than their super-alloy counterparts, results in a 50% weight reduction in the turbine engine component weight.[4]

1.1.1 Processing of CMCs

Ceramic matrix composites often consist of three main constituents: fibers, matrix and a fiber/matrix interphase coating. Ceramic matrix composites can be manufactured using a number of different processes including hot pressing techniques, chemical vapor processes, melt-infiltration, and polymer infiltration and pyrolysis (PIP).[3,5] GE's HiPerComp^{TM} melt infiltrated (MI) SiC/SiC composites contain continuous Hi-Nicalon Type S SiC fibers, coated with a boron nitride (BN) interphase, embedded in a dense SiC matrix also consisting of residual Si left from processing. An image depicting the melt infiltration reaction process that was published in the Bulletin of the American Ceramic Society is shown in Figure 1.2. The melt infiltration process used to create the samples used for testing consists of using a prepreg method. Prepregs are created by coating the Hi-Nicalon Types S SiC fibers with a multi-layer BN coating via chemical vapor deposition and running the fibers through a matrix slurry containing SiC, carbon, binders and solvents. The fiber coating is utilized to provide a weak interphase between the fiber and matrix in order to increase mechanical toughness and the coating also prevents chemical attack of the fiber during processing. Once the fibers are coated, they are wound into unidirectional preform tapes and the tapes are stacked to form the desired laminate architecture.[3] After the prepreg is formed, a dense composite is developed through the infiltration of liquid silicon or silicon alloy into the porous preform which reacts with the carbon in the preform to create a SiC matrix with 5 to 15 vol% residual silicon.

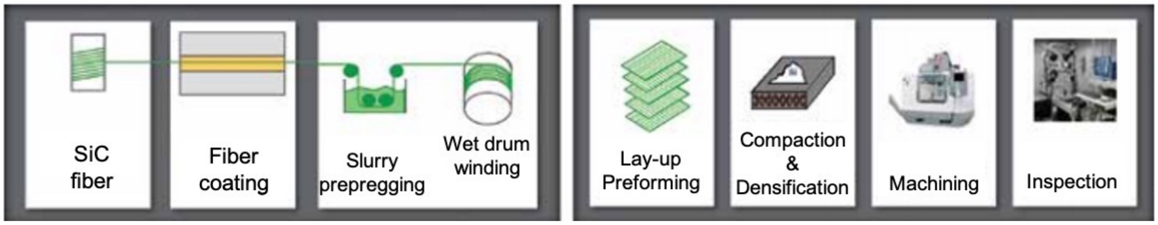

Figure 1.2 Melt Infiltration process used to produce GE's HiPercompTM SiC/SiC CMCs starting with the fiber coating, the slurry prepreg process into wet drum winding, the layup of the preforms (here is where the architecture is determined), next the compaction and densification, and lastly machining and inspection. This figure was published in 2019 in the American Ceramic Society Bulletin.

1.2 Mechanics of Ceramic Matrix Composites

Typical monolithic ceramic materials under uniaxial tension experience brittle catastrophic failure as a result of one single crack that will propagate due to a large flaw in the material. Alternatively, ceramics reinforced with ceramic fibers, such as CMCs exhibit improved toughening due to small cracks initiating throughout the matrix.[10-12] Figure 1.3 shows the non-linear stress-strain behavior on the left where the non-linearity exhibited in a ceramic matrix composite is due to matrix cracking, depicted on the right.

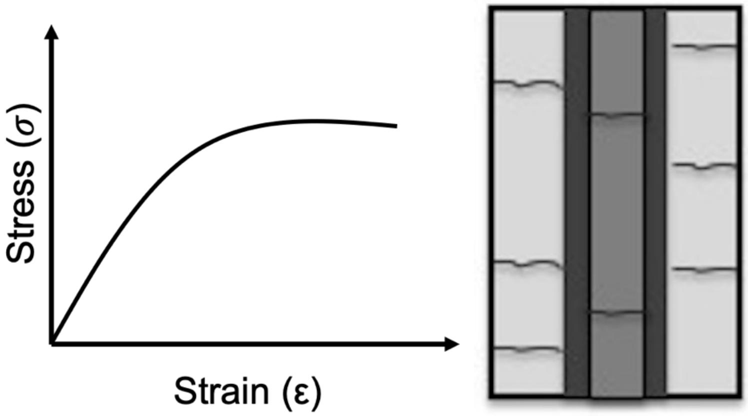

Figure 1.3 Fracture behavior a fiber reinforced ceramic matrix composite with weakly coated fibers where the non-linearity is due to matrix cracking depicted by the composite image on the right. If the fiber coating is strongly bonded between the fibers and matrix then the material will have similar fracture behavior to that of a pure monolithic ceramic

When a uniaxial tensile load is applied to a CMC with uniaxial fibers, initially the specimen will act linear elastically and the axial elastic modulus of a CMC with uniaxial fibers is expected to follow the rule of mixtures described by Equation (1.1) which is governed by the fiber and matrix elastic moduli where E is the elastic modulus, v is the volume fraction of each constituent, and the subscripts f, m, and c refer to the fibers, matrix, and composite respectively. The distribution of applied composite stress before damage occurs is shown in Equation (1.2) and depends on the strength of the matrix (σ_m) and fiber (σ_f) materials. When the CMC is still undamaged, the far-field strain in the fibers and matrix are equivalent and can be described by a statement of isostrain in Equation (1.3) where strain (ε) has been replaced by Hooke's Law.

$$E_c = v_f E_f + v_m E_m \tag{1.1}$$

$$\sigma = v_f \sigma_f + v_m \sigma_m \tag{1.2}$$

$$\frac{\sigma}{E_c} = \frac{\sigma_f}{E_f} = \frac{\sigma_m}{E_m} \tag{1.3}$$

This linear elastic behavior is observed up until damage is initiated with the weaker matrix cracking first. The main damage mechanisms that occur in ceramic matrix composites include matrix cracking, fiber debonding, and fiber fragmentations. Figure 1.4 is taken from Evans and Zok and depicts the fundamental damage mechanisms that occur in a ceramic matrix composite.[13] The stress in fibers at the matrix crack plane can be determined by dividing the applied stress by the volume fraction of the fibers. The stress at which steady-state matrix cracking occurs has been derived from energy arguments and has also been extended to account for residual stresses and fiber/matrix debonding.[14-18]

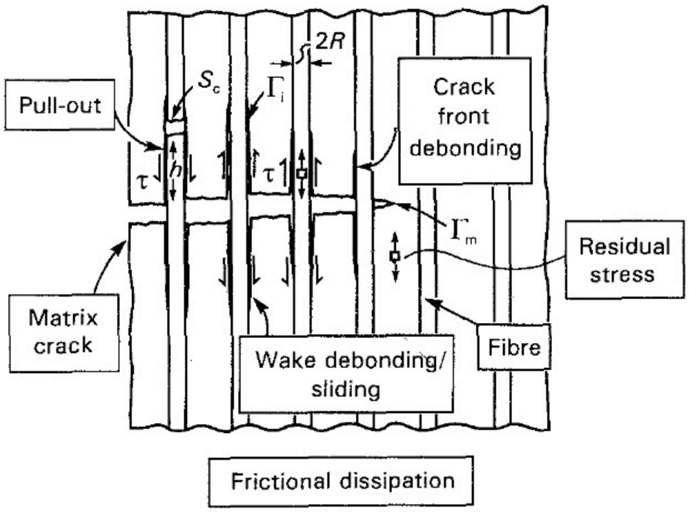

Figure 1.4 The damage mechanisms that occur in a unidirectional ceramic matrix composites after the onset of matrix cracking. Image taken from Evans and Zok manuscript.[13]

Each mechanism has been studied extensively in the literature both experimentally and theoretically. It is predicted and has been observed that once a matrix crack initiates, the matrix crack will deflect along the fiber interface (assuming a weak fiber coating) and frictional dissipation occurs as a result of debonding between the fiber/matrix interface and a sliding resistance or shear stress, τ, that occurs along the interface. At the plane of the matrix crack, the matrix no longer carries any load and the load is transferred equally to each bridging, or intact, fiber where the fibers will in turn carry all the applied load.

After the onset of the first matrix crack, the number of matrix cracks will continue to grow steadily until the matrix is saturated with through-thickness matrix cracks and no more cracking can develop. Figure 1.5 represents the general stress profile in both the matrix in the fiber around the plane of a matrix crack which is represented by a dashed line. As stated previously, the fibers carry all of the load at the plane of the matrix crack and thus the stress in the bridging fibers at the location of the matrix crack is at a maximum while the matrix carries no stress and therefore the stress in the matrix at the matrix crack plane is zero. The stress in both the fibers and the matrix will continue to change with distance from the matrix crack plane until eventually both the fiber and matrix will achieve their initial far-field stress-strain. The distance from the matrix crack plane that it takes for the fiber and matrix constituents to experience their initial far-field stress-strain is often referred to as the shear lag distance.

The onset of matrix cracking and the matrix crack spacing are parameters often used to help describe the mechanics of these composite specimens. The spacing of matrix cracks was first correlated to the first matrix cracking stress and the interfacial shear stress by Aveston et al.[10] However, this model assumed an unbonded fiber/matrix interface which means that the debonding mechanism wasn't considered and therefore the energy analysis was lacking in the energy required for debonding which has been determined to occur in most SiC/SiC CMC systems. As a result, subsequent models have been developed to account for the weakly bonded interfaces that debond between the fiber and the matrix during loading. Debonding occurs simultaneously with matrix cracking and also accounts for the interactions between neighboring matrix cracks.[19-22] The properties and characteristics of the composite material, such as coating thickness of the interface between the fiber and matrix, can also dictate how cracks1 propagate through the composite and there are damage models that are solely concerned with the mechanics of this interface.[23-24]

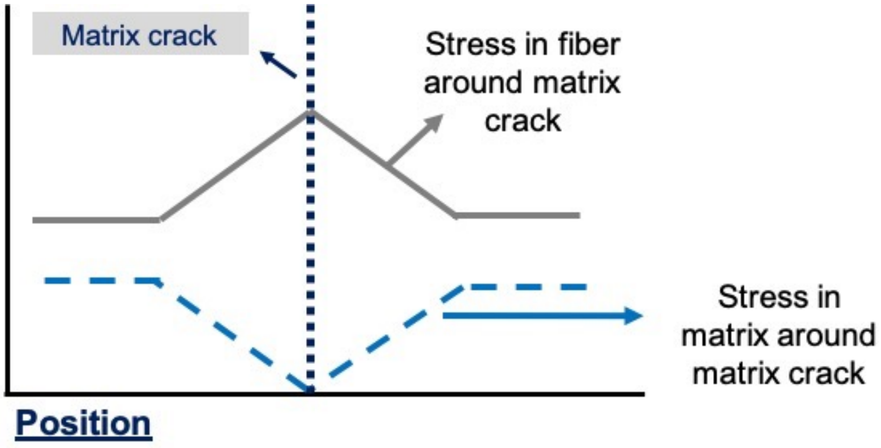

Figure 1.5 The stress/strain profile in both the intact bridging fiber (gray curve) and the matrix (blue curve) as a function of distance from the matrix crack plane. At the matrix crack plane, the stress in the fiber is at a maximum because it is carrying all of the applied load while the stress in the matrix is at a minimum because it is carrying no load.

As applied stress continues to increase after matrix cracking and fiber/matrix debonding have initiated, additional non-linearity will occur in the form of fiber fragmentations. Fiber fracture occurs after the onset of matrix cracking and can occur simultaneously with concurrent matrix cracking. There has been an extensive amount of work in the literature on the statistical considerations of fiber failure. Once a fiber fractures, the load it was carrying is then transferred equally to all of the other intact fibers in a process known as global load sharing.[25-32] Once enough fibers have fragmented and the remaining fibers can no longer carry load the composite specimens fail. Although the consideration of fiber fragmentations has previously been studied and incorporated into mechanical models, there have been limited experimental observations of fiber fragmentations due to experimental limitations. Characterization studies involving surface measurements require polishing the surface which damages the SiC fibers preventing observation of in-situ fiber fragmentations. Fiber fragmentations have been detected using AE but these observations do not provide accurate spatial resolution of fiber fragmentations and their corresponding position. The work presented here is one of the first to document in situ fiber fragmentation observations within a melt-infiltrated laminated SiC/SiC CMC showing both size and location within the microstructure.

Cross-ply laminate composites experience essentially the same damage mechanisms as occur in the unidirectional composites. Damage mechanisms that occur in cross-ply composites, such as matrix crack bridging and fiber debonding, are depicted in Figure 1.6, taken from Evans et al. Due to the similarities, most mechanical analyses utilized for unidirectional composites can be directly used or slightly adapted to describe the cross-ply composites tensile response. One of the major differences is that the cross-ply composite specimens are comprised of two different plies with different fiber orientations (0° and 90° to the loading direction) and each ply will exhibit different elastic moduli. The elastic modulus of the longitudinal ply is expected to follow a simple rule of mixtures shown in Equation (1.4). Assuming the effective modulus of the fibers in the transverse plies is zero, then the transverse composite ply modulus can bet determined using Equations (1.5) and (1.6).[33]

$$E_L = v_f E_f + v_m E_m \tag{1.4}$$

$$E_T = \left[\frac{\left(1 + 2\eta v_f\right)}{\left(1 - \eta v_f\right)}\right] E_m \tag{1.5}$$

$$\eta = \frac{\dfrac{E_f}{E_m} - 1}{\dfrac{E_f}{E_m} + 2} \tag{1.6}$$

When comparing the stress profiles between the two types of composite architectures, one of the main disparities is that cross-ply composites exhibit matrix cracking at lower stresses which in turn results in a lower proportional limit.[34] In cross-ply composites, the 0°, or longitudinal plies, act as a toughening mechanism because the fibers, parallel to the loading direction, directly carry load, compared to 90°, or transverse plies where the fibers are perpendicular to the applied load and therefore the fibers do not experience load and as a result do not experience fiber fragmentation. Matrix cracking will first occur as "tunnel cracks" in the transverse plies and eventually the matrix crack will penetrate into the longitudinal plies.[13,33-38] The fiber fragmentation process that controls the ultimate strength is similar to the process observed in the unidirectional specimens except the fiber fragmentations only occurs in the longitudinal plies.

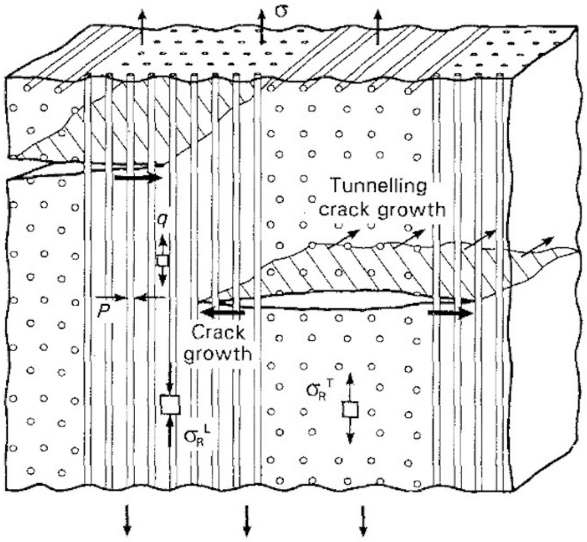

Figure 1.6 View of tunneling crack in cross-ply laminate along with the damage mechanisms that occur in this system. This image was taken from Evans and Zok manuscript[13]

1.2.1 Previous Work Performed to Study on SiC/SiC CMCs (Literature Review)

Typically, damage accumulation in CMCs is directly observed using surface microscopy techniques either in situ or post fracture.[39-44] For example, in-situ tensile testing in collaboration with Scanning Electron Microscopy (SEM) and Digital Image Correlation (DIC) has been utilized to observe and track the progression of matrix cracking in woven SiC/SiC CMCs by Sevener et. al.[40] Using the SEM allowed for not only the visualization of the matrix crack opening, an important variable in the mechanics of these materials, but also the opportunity to measure the crack opening displacement (COD). DIC was then used to observe and track changes in the local strain on the surface of the specimen including strain near damage as the applied load was incrementally increased. Other nondestructive methods, such as acoustic emission (AE) and electrical resistance (ER) have been utilized to study types of damage that occur in CMCs under various types of loading and environmental conditions.[45-49] Almansour et al used AE to look at how various fiber fractions in minicomposites affected the mechanical properties of the composite.[48] Using AE allowed for the stress at which the onset of matrix cracking occurred to be experimentally determined in each type of specimen and the experimental values were then compared to the predicted models. It was found that the onset of matrix cracking in the minicomposite specimens had excellent agreement with both the first loud AE event and predictions from models that accounted for interface debond energy. Morscher et al have also performed matrix crack studies on GE's HiPerComp™ SiC/SiC CMC materials using AE where they found consistent relationships for strain and matrix crack density with AE activity.[46]

The use of x-ray micro-computed tomography (μ-CT) to observe damage in various types of CMCs has proven to be a valuable non-destructive technique.[50-56] Bale et al utilized synchrotron tomography to observe damage progression in mini composites and a woven textile composite at high temperature (1600 °C).[50] Mini composites were imaged with a resolution of 0.65 μm per voxel due to their smaller dimensions being more complimentary to the micro-CT set-up. However, due to the need for larger specimens to get a representative textile volume, textile composites were also imaged with a lower resolution of 1.3 µm per voxel. They determined that matrix crack observations at room temperature (25 °C) often differ from the types of matrix cracking that occurred at high temperatures due to material oxidation effects. Minicomposites were also studied under tensile load using synchrotron radiation at the European Synchrotron Radiation Facility (ESRF) by Chateau et al where they were able to use observed distribution of matrix fragment lengths and fiber break densities to fit and appropriate interfacial parameter.[52]

The use of micro-CT is beneficial in regard to damage progression observations in SiC/SiC CMCs under tensile load and it should also be stated that testing can be performed in various environments. Micro-CT has the advantage that damage can be tracked in-situ through the entire volume, as opposed to typical surface measurements that often occur post-fracture. These micro-CT volumetric observations enable a better understanding damage accumulation relates to the microstructure of ceramic matrix composites.

1.3 Micro-CT Tomography

X-ray computed tomography is a non-destructive imaging technique where x-rays penetrate through the specimen and then a series of 2D projections is combined into a 3D cross-sectional map of the specimen through reconstruction algorithms. The specimen is typically rotated around a single rotation axis of either 180° or 360° and projections are recorded. Next, a reconstruction algorithm uses the projections to produce a 3D volume set.[57-62] The generated x-rays used for imaging can interact with the specimen in various manners depending on the x-ray energies. For example, elastic scattering and the photoelectric effect govern low-energy x-rays and can modify the incident x-ray beam intensity and direction whereas higher x-ray energy, often result in Compton scattering and can affect the x-rays passing through the specimen.[57] The way the x-rays interact with the specimen is important because tomographic reconstruction of the specimen relies on comparing the incident beam and the beam exiting the specimen. Different materials will interact with the x-rays in different ways and in order to understand the contrast within the x-ray reconstruction it is necessary to understand how an x-ray interacts with a single material. The interaction of a x-rays through the specimen can be studied by looking at the intensity transmitted through the specimen, I, at a specific incident x-ray intensity I_0 using Equation (1.7). Where t is the thickness of the specimen, and μ is the x-ray attenuation coefficient which depends on the element being imaged. The linear attenuation coefficient increases with increasing atomic number and increasing physical density of the absorbing material. For imaging composite materials with different compounds, each beam is attenuated by $\mu(z)$ from z=0 to z=t and the final tomography imaging is done by algorithms that combine many beams in many directions to infer the spatial distribution of μ.

$$I = I_0 e^{-\mu t} \tag{1.7}$$

Synchrotron radiation is produced by electron bunches accelerating at high speeds, nearly the speed of light, moving in a curved path due to bending magnets. The wavelengths of synchrotron radiation span the electromagnetic spectrum from infrared to x-rays. Synchrotron radiation is often more advantageous than tube sources when it comes to x-ray imaging due to its higher flux and brightness. Also due to beamline set-ups, it is often easier to perform in situ experiments using synchrotron radiation rather than lab scale instruments as a result of faster scan times. Synchrotron facilities consist of three main components: (1) the mechanism where electrons are first accelerated by a linear accelerator of low energy (2) the circular accelerator , or synchrotron and (3) the storage ring which uses an assembly of bending magnets to deflect the electrons and force them to circulate within the ring.[58-61] Figure 1.7a represents the components of a synchrotron facility while Figure 1.7b represents the electrons within a storage ring.

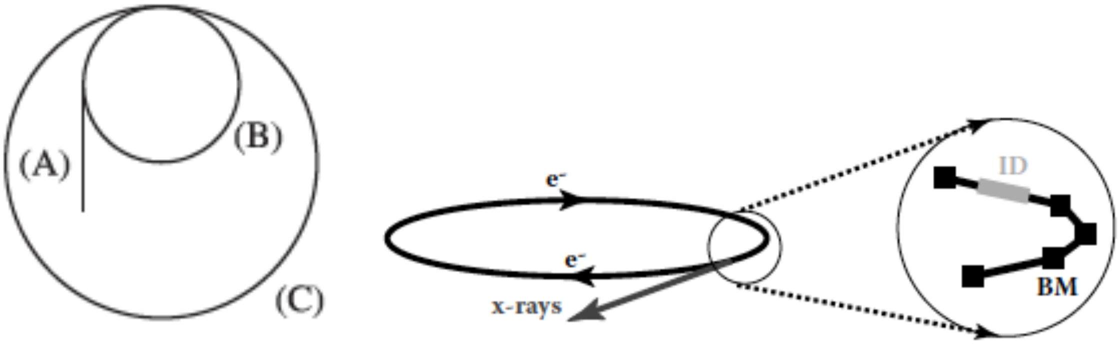

(a) (b)

Figure 1.7 Schematic of (a) the components of a synchrotron facility where A) is the linear accelerator B) is the synchrotron, and C) is the storage ring. Figure taken from Grangeat tomography chapter.[61] (b) the electron bunches circulating around a storage ring in a synchrotron facility. Figure taken from Orhan MicroComputed Tomography Chapter.[58]

For SiC/SiC CMCs the matrix material and the reinforcement material are made of, nominally, the same compound, SiC, resulting in little contrast between the fibers and matrix. However, the boron nitride (BN) interface between the fiber/matrix has a very low attenuation coefficient (μ) and so in turn appears dark and can be used to differentiate between the matrix and the reinforcing fibers. Phase enhanced imaging can also be used to better differentiate between the SiC fibers and the SiC matrix. Phase-enhanced imaging is a result of sharp changes in refractive index where the intensity can be emphasized, in this case at the boron nitride fiber/matrix interface coatings. The phase contrast can operate as an enhancement of the absorption contrast. The effect of phase contrast varies for the sample to detector distance however, it is also known that a smaller sample-to-detector distance leads to a better spatial resolution.[63] As a result there is often a give and take between the phase contrast and the desired spatial resolution in order to produce the optimum imaging.

1.3.1 Advanced Light Source (ALS)

All of the synchrotron tomography imaging shown in this body of work was performed on beamline 8.3.2 at the Advance Light Source (ALS) at Lawrence Berkeley National Lab. The samples tested were HiPerComp^{TM} composite specimens with 28 volume % SiC Hi-Nicalon Type S fibers and were imaged using the full spectrum of the x-ray beam while under tensile load. The cell at the end of the beamline that was used consists of a 7 mm tall and 300 µm thick aluminum window which allows for x-rays to penetrate through the sample to a scintillator where radiographs are converted to visible light and then recorded on a high-resolution camera. The camera had multiple objective lens systems available for use, but a 3x lens was used which resulted in a resolution of 1.3 µm/pixel and a field of view of 3.3 mm x 2.8 mm (width x height). A commercial reconstruction algorithm (Octopus v8; IIC UGent, Zwijnaarde) was used to create the tomography slices from the recorded radiographs.[63] The sample stage and detector were set a particular distance such that a component of phase contrast was present along with absorption contrast in the images, as evident by the bright edges of the sample. The phase-contrast helps to highlight small discontinuities in the sample and provides the ability to see incipient cracks and the tips of long cracks clearly.[63] The resolution achieved due to the phase-contrast effect has not been measured, and accurate quantification would require a systematic study. In the present study, the detection limit in terms of the matrix crack opening is assumed to be 1.3 µm (nominal voxel size) but smaller crack openings are likely detected due to enhanced visibility caused by phase-contrast effect.

In order to obtain a full 3D tomography dataset, the sample stage, which consisted of the specimen loaded in tension, had to be able to rotate up to 180°. Radiographs were recorded at increasing angles of rotation and were then used to recreate the 3D image of the specimen within the field of view. For the specimen to be constantly under load and also have the ability to rotate, the loading system was mounted on an air-bearing rotation stage and the load was applied to the sample using a stepper motor. The force and displacement were measured using an in-line load cell and a linear variable differential transformer (LVDT) sensor.[50] The tensile testing in this work was also accompanied with acoustic emissions (AE) to identify when damage was occurring to conserve scan time and to be able to compare the damage detected using AE to the damage observed using the synchrotron tomography.

1.4 Thesis Objective and Organization

The goal of this research is to be able to observe in real-time, how damage evolves within a melt-infiltrated HiPerComp^{TM} SiC/SiC ceramic matrix composite and then to use the observations to compare to mechanics models and eventually relate the observations back to the microstructure. Ceramic composite specimens were imaged under tensile loads at increasing stress increments. Two types of specimens were studied: unidirectional specimens with fibers running parallel to the loading direction and cross-ply laminates with alternating 0°/90° plies symmetric around a matrix rich region. The first half of the thesis extensively describes matrix evolution within the unidirectional specimen and fiber fragmentation accumulation. The location of fiber fragmentations is correlated to the location each detected matrix crack within the specimen at increasing stress increments. The observed behavior for both damage mechanisms was compared to theoretical mechanical models from the literature. The second half of this thesis focuses on matrix cracking and fiber fragmentation observations for the cross-ply composite architecture. The damage evolution observed and measured in each cross-ply specimen are compared to the observations within the unidirectional specimen. Also, damage characteristics quantified using acoustic emissions (AE) techniques will be compared to damage characteristics quantified using micro-CT imaging. Lastly, preliminary work describing the distribution of fibers within the composite structure and initial results presenting clustering of fiber fragmentations will be discussed.

References

1. M. Balasubramania. Ceramic matrix composites. IN: Composite Materials and Processing. Boca Raton, FL: CRC Press, 2013 p355-462.
2. Chawla KK. Ceramic matrix composites. In: Composite Materials Science and Engineering 4th ed. Cham, Switzerland: Springer Nature, 2019; p 251-296
3. Corman GS, Luthra KL. Silicon melt infiltrated ceramic composites (HiPerComp™). In: Bansal NP, editor. Handbook of ceramic composites. Boston, MA: Springer, 2005; p. 99-115.
4. Steibel J. Ceramic matrix composites taking flight at GE Aviation. Am Ceram Soc Bull 2019; 98(3): 30-33.
5. DiCarlo J.A, Yun H-M, Morscher G.N., Bhatt R.T., SiC/SiC composites for 1200°C and above. In: Bansal NP, editor. Handbook of ceramic composites. Boston, MA: Springer, 2005; p. 77-98.
6. Steyer TE. Shaping the future of ceramics for aerospace applications. Int J Appl Ceram Technol 2013; 10(3): 389-394.
7. Zok FW. Ceramic-matrix composites enable revolutionary gains in turbine engine efficiency. Am Ceram Soc Bull 2016; 95(5): 22-28.

8. Ohnabe H, Masaki S, Onozuka M, Miyahara K, Sasa T. Potential application of ceramic matrix composites to aero-engine components. Composites, Part A. 1999; 30(4):489-496.
9. Corman GS, Dean AJ, Brabetz S, Brun MK, Luthra KL, Tognarelli L, et al. Rig and engine testing of melt infiltrated ceramic composites for combustor and shroud applications. J Eng Gas Turbines Power 2002; 124(3): 459-464.
10. Aveston J, Cooper GA, Kelly A. The properties of fibre composites. Conference Proceedings, National Physical Laboratory 1971;(15).
11. Marshall DB, Cox BN, Evans AG. The mechanics of matrix cracking in brittle-matrix fiber composites. Acta Metall. 1985; 33(11):2013-2021.
12. Domergue J-, Vagaggini E, Evans AG. Relationships between Hysteresis Measurements and the Constituent Properties of Ceramic Matrix Composites: II, Experimental Studies on Unidirectional Materials. J Am Ceram Soc 1995;78(10):2721-2731.
13. Evans A, Zok F, The physics and mechanics of fiber-reinforced brittle-matrix composites. J. Mater. Sci. 1994; 29: 3857–3896.
14. Aveston J, Kelly A, Theory of Multiple Fracture of Fibrous Composites. J. Mater. Sci. 1973; 8: 352-362
15. Marshall DB, Cox BN. Tensile fracture of brittle matrix composites: Influence of fiber strength. Acta Metallurgica 1987;35(11):2607-2619.
16. Evans AG, Marshall DB. The mechanical behavior of ceramic matrix composites. Acta Metallurgica 1989;37(10):2567-2583.
17. Budiansky B, Hutchinson JW, Evans AG. Matrix fracture in fiber-reinforced ceramics. J Mech Phys Solids. 1986; 34(2):167-189.

18. Curtin WA. Theory of Mechanical Properties of Ceramic-Matrix Composites. J Am Ceram Soc 1991;74(11):2837-2845.
19. Zok F, Spearing S. Matrix crack spacing in brittle matrix composites. Acta Metall Mater. 1992; 40:2033–2043.
20. Budiansky B, Hutchinson JW, Evans AG. Matrix fracture in fiber-reinforced ceramics. J Mech Phys Solids. 1986; 34(2):167-189.
21. Budiansky B, Evans AG, Hutchinson JW. Fiber-matrix debonding effects on cracking in aligned fiber ceramic composites. Int J Solids Struct. 1995; 32(3-4):315-328.
22. Curtin WA. Multiple matrix cracking in brittle matrix composites. Acta Metallurgica Et Materialia 1993; 41(5):1369-1377.
23. Hutchinson J, Jensen H Models of fiber debonding and pullout in brittle composites with friction. Mech Mater 1990;9(14):139–164.
24. Gupta V, Yuan J, Martinez d. Calculation, measurement, and control of interface strength in composites. J Am Ceram Soc 1993;76(2):305–315 15. Walter ME, Ravich
25. Thouless MD, Evans AG. Effects of pull-out on the mechanical properties of ceramic-matrix composites. Acta Metallurgica 1988;36(3): 517-522
26. Oh HL, Finnie I. On the location of fracture in brittle solids-I - Due to Static Loading. Int J Fract 1970;6(3):287-300.
27. Curtin WA, Takeda N. Tensile strength of fiber-reinforced composites: I. Model and effects of local fiber geometry. J Compos Mater 1998; 32(22): 2042-2059.
28. Hutchinson JW, Jesen HM. Models of fiber debonding and pullout in brittle composites with friction. Mech Mater 1990; 9(2): 139-163

29. Callaway BE, Zok FW. Tensile response of unidirectional ceramic minicomposites. J Mech Phys Solids. 2020; 138
30. Sutcu M. Weibull statistics applied to fiber failure in ceramic composites and work of fracture. Acta Metallurgica 1989; 37(2): 651-661
31. McNulty JC, Zok FW. Application of Weakest-Link Fracture Statistics to Fiber-Reinforced Ceramic-Matrix Composites. J Am Ceram Soc. 1997; 80(6): 1535-1543
32. Callaway EB, Zok FW. Accurate determination of fiber strength distributions. J Am Ceram Soc. 2017; 100(3): 1202-1211
33. Beyerle DS, Spearing SM, Evans AG. Damage Mechanisms and the Mechanical Properties of a Laminated 0/90 Ceramic/Matrix Composite. J Am Ceram Soc 1992; 75(12): 3321-3330.
34. Sorenson B., Evans R., Analysis of Damage in a Ceramic Matrix Composite. Int J Dam Mech. 1992; 2: 246-271
35. O'Day MP, Curtin WA, Marshall DB. Failure of crossply ceramic-matrix composites. J Am Ceram Soc 2002;85(6):1553-1560.
36. Xia ZC, Hutchinson JW, Evans AG, Budiansky B. On large scale sliding in fiber-reinforced composites. J Mech Phys Solids 1994;42(7):1139-1158.
37. Xia ZC, Carr RR, Hutchinson JW. Transverse cracking in fiber-reinforced brittle matrix, cross-ply laminates. Acta Metllaurgica Et Materialia 1993; 41(8): 2365-2376.
38. Evans AG, Domergue J, Vagaggini E. Methodology for Relating the Tensile Constitutive Behavior of Ceramic-Matrix Composites to Constituent Properties. J Am Ceram Soc 1994; 77(6): 1425-1435.

39. Meyer P, Waas AM. Measurement of in situ-full-field strain maps on ceramic matrix composites at elevated temperature using digital image correlation. Exp Mech. 2015; 55(5): 795-802.

40. Sevener KM, Tracy JM, Chen Z, Kiser JD, Daly S. Crack opening behavior in ceramic matrix compsoites. J Am Ceram Soc. 2017; 100(10):4734-4747.

41. Morscher GN, Ojard G, Miller R, et al. Tensile creep and fatigue of Sylramic-iBN melt-infiltrated SiC matrix composites: retained 4746 | SEVENER ET AL. properties, damage development, and failure mechanisms. Compos Sci Technol. 2008;68:3305-3313.

42. Wing BL, Halloran JW. Microstress in the matrix of a melt-infiltrated SiC/SiC ceramic matrix composite. J Am Ceram Soc. 2017; 100(11) 5286-5294.

43. Lamon J. A micro-mechanics based approach to the mechanical behavior of brittle-matrix composites. Compos Sci Technol. 2001;61:2259-2272. 33. Morscher GN, DiCarlo JA, Kiser JD, Yun HM. Effects of fiber architecture on matrix cracking for melt-infiltrated SiC/SiC composites. Int J Appl Ceram Technol. 2010;7:276-290.

44. McDonald KR, Dryden JR, Zok FW. Effects of matrix cracks on the thermal diffusivity of a fiber-reinforced ceramic composite. J Am Ceram Soc. 2001;84:2015-2021.

45. Morscher GN, Gordon NA. Acoustic emission and electrical resistance in SiC-based laminate ceramic compsoites tested under tensile loading. J Eur Ceram Soc. 2017; 37(13):3861-3872.

46. Smith CE, Morscher GN, Xia Z. Electrical resistance as a nondestructive evaluation technique for SiC/SiC ceramic matrix composites under creep-rupture loading. Int J Appl Ceram Technol. 2011; 8(2):298-307.

47. Almansour A, Maillet E, Ramasamy, S, Morscher GN. Effect of fiber content on single tow SiC minicomposite mechanical and damage properties using acoustic emission. J Eur Ceram Soc. 2014; 35(13): 3389-3399.
48. Whitlow T, Jones E, Przybyla C. In-situ damage monitoring of a SiC/SiC ceramic matrix composite using acoustic emission and digital image correlation. Compos Struct. 2016; 158: 245-251.
49. Bale HA, Haboub A, Macdowell AA, Nasiatka JR, Parkinson DY, Cox BN, et al. Real-time quantitative imaging of failure events in materials under load at temperatures above 1,600°C. Nat Mater. 2013; 12(1): 40-46.
50. Larson NM, Zok FW. In-situ 3D visualization of composite microstructure during polymer-to-ceramic conversion. Acta Mater. 2018; 144: 579-589.
51. Bernachy-Barbe F, Gélébart L, Bornert M, Crépin J, Sauder C. Anisotropic damage behavior of SiC/SiC composite tubes: Multiaxial testing and damage characterization. Composites, Part A. 2015; 76: 281-288.
52. Chateau C, Gélébart L, Bornert M, Crépin J, Caldemaison D, Sauder C. Modeling of damage in unidirectional ceramic matrix composites and multi-scale experimental validation on third generation SiC/SiC minicomposites. J Mech Phys Solids. 2014; 63(1): 298-319.
53. Larson NM, Zok FW. Insights from in-situ x-ray computed tomography during axial impregnation of unidirectional fiber beds. Composites, Part A. 2018; 107:124-134.
54. Mazars V, Caty O, Couégnat G, Bouterf A, Roux S, Denneulin S, et al. Damage investigation and modeling of 3D woven ceramic matrix composites from x-ray tomography in-situ tensile tests. Acta Mater. 2017; 140:130-139.

55. Saucedo-Mora L, Lowe T, Zhao S, Lee PD, Mummery PM, Marrow TJ. In situ observation of mechanical damage within a SiC-SiC ceramic matrix composite. J Nucl Mater 2016; 481:13-23.

56. Thornton J, Arhatari BD, Sesso M, Wood C, Zonneveldt M, Kim SY, et al. Failure Evaluation of a SiC/SiC Ceramic Matrix Composite during In-Situ Loading Using Micro X-ray Computed Tomography. Microsc Microanal 2019 (*In Press*)

57. Kinney JH, Nichols MC. X-ray tomographic microscopy (XTM) using synchrotron radiation. Annu Rev Mater Sci 1992; 22(1): 121-152.

58. Stock S. Fundamentals. In: Orhan K, editor. Microcomputed Tomography. Boca Raton: CRC Press; 2009; p. 9-20

59. Stock S. Micro-CT Systems. In: MicroComputed Tomography. Boca Raton: CRC Press; 2009; p 39-84

60. Haibel A. Synchrotron Tomography In: Seeck OH, Murphy B. X-Ray Diffraction Modern Experimental Techniques. CRC Press: Taylor & Francis Group; 2014. P. 315-339

61. Charvet AM, Peyrin F. Synchrotron Tomography In: Pierre Grangeat, Tomography. John Wiley & Sons, Inc.;2009 p. 197-215

62. Kanitpanyacharoen W, Parkinson DY, Francesco DC, Marone F, et al. A comparative study of X-ray tomographic microscopy on shales at different synchrotron facilities: ALS, APS SLS. J. of Synchrotron Radiation 2013; 20(1): 172-180.

63. Cloetens, P., Pateyron-Salomé, M., Buffiere, J. Y., Peix, G., Baruchel, J., Peyrin, F., Schlenker, M. Observation of microstructure and damage in materials by phase sensitive radiography and tomography. Journal of Applied Physics. 1997; 81(9), 5878-58

Chapter II. Observation of matrix cracking and fiber break openings in unidirectional SiC/SiC CMCs using micro-CT tomography techniques[1]

2.1 Introduction

CMCs can withstand much higher temperatures than the most capable superalloys. Like monolithic ceramics, they remain strong and stiff at very high temperatures, but embedded ceramic reinforcing fibers prevent brittle failure and dissipate energy through a fiber pullout process, resulting in much better damage tolerance[1]. SiC-SiC CMCs are used in the turbine shrouds of turbofan engines and have been evaluated experimentally in many other high-temperature applications.

The CMC failure process is qualitatively different from that in other materials. As with monolithic ceramics, both the fiber and matrix have a size-dependent probability of local failure. However, in the simple case of a CMC loaded monotonically in homogeneous tension in the fiber direction, failure starts with transverse, through-matrix cracks, those cracks being deflected around the fibers by passing through weak fiber coatings. Upon further loading, fibers will move relative to the matrix and then break, with ultimate failure

---

[1] Most of this chapter was published as a paper in Ceramics International on February 15, 2020 and has been reformatted for dissertation format with additional data incorporated

occurring after all fibers at one section have broken.[2-4] This scenario is the one that has been most studied both experimentally and theoretically.[5-9]

A considerable amount of previous work has been focused on unidirectional CMCs in the form of minicomposites; that is, a single tow of about 500 fibers infiltrated with matrix.[10] Minicomposites are well-suited for observations of ultimate failure but differ from laminates in ways that affect matrix crack initiation and progression. In a laminate, the tows are flattened and laid side-by-side, whereas in a minicomposite the tow retains its as-produced cross-sectional arrangement of fibers, which can take on a variety of shapes. This variation causes large discrepancies in the microstructure including fiber spacing and volume fraction of fibers. The microstructure irregularities and fiber-starved areas within the section tend to be filled by the matrix in unpredictable ways and can change along the length of the minicomposite, which will localize matrix cracking differently when compared to laminate composites. For these reasons, a technique for directly testing unidirectional laminate specimens was created. In the present study, microtomography was used to observe damage progression and ultimately the failure of CMC laminates composed of a melt-infiltrated siliconized SiC matrix around Hi-Nicalon Type S SiC fibers coated with a multilayer, BN-based interphase.

2.1 Methods and Materials

2.2.1 Unidirectional SiC/SiC CMC Specimens

Unidirectional specimens were produced from [0°/90°] cross-ply specimens fabricated at GE Research using the manufacturing methods utilized for commercial HiPerComp^{TM}. The unidirectional specimens were fashioned from the original cross-ply architecture by a two-step process: (1) dogbones were cut from cross-ply laminate panels with the long axis oriented along the panel 0° direction (2) the outer plies were removed from the gauge section until only the two center plies remained. The outer plies were ground off using a 25.4-mm diameter diamond grinding wheel, leaving an approximately 9-mm-long, uniform-thickness gauge section as shown in Figure 2.1. These may be thought of as double-reduced dogbones. The main challenge in tensile testing of unidirectional laminates, whether polymer-matrix or ceramic-matrix, is avoiding the ends being crushed or sheared off by the grips before the gauge section fails. By reducing the cross-sectional area in the gauge by about 75%, the force needed to fail the specimen, and thereby the risk of grip failure, is reduced accordingly.

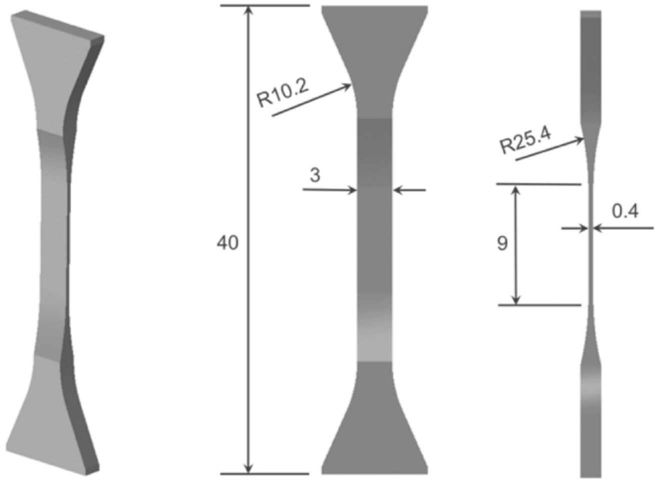

Figure 2.1 Un-notched double-reduced unidirectional specimen. Dimensions are in mm

2.2.2 ALS Beamline and Tensile Test Set-Up

The two unidirectional specimens were imaged and tested at the Advanced Light Source at Lawrence Berkeley National Lab. There has been previous work done on SiC/SiC composite materials utilizing the same beamline hot cell that was used for the present study. Bale et al used the hot cell to characterize the damage and failure process in SiC-SiC minicomposites and a C-SiC textile composite plate in tension.[11,12] Studies have been done on the beamline to observe *in situ* 4D (3D + time) PIP processing of SiC/SiC CMCs using preceramic polymers.[13] Also, additional discussion of CMC damage processes and efforts to observe them with the combination of synchrotron work and acoustic emissions was reported by Maillet et al.[14]

Two unidirectional specimens were imaged under tension using the full spectrum of the X-ray beam, in a continuous tomography scan mode. The loading stage allowed the specimen to be translated up and down during the experiment in order to move areas of interest into the field of view. As more cracks appeared, the loading stage was translated vertically so that as many interesting cracks as possible were captured in the field of view. The *in situ* hot cell described by Bale et al was utilized for this work in which the load is provided by a stepper motor driving a lead screw that advances in the vertical direction.[11] The hot cell has high-temperature capability via heat lamps; however, the heat lamps were not used for these experiments. The load cell was designed to operate at forces up to 2 kN. The samples were gripped in custom water-cooled, Inconel 718 grips (PulseRay, Inc., Beaver Dams, New York). A thin layer of ceramic powder of low thermal conductivity was applied between the sample and the grips to prevent sticking. All of the tensile experiments were carried out in displacement control mode, and the load was read by a load cell (Model 9820, Interface Advanced Force Measurement, Scottsdale, Arizona). During the experiment, the stage displacement and load were recorded once per second.

The unidirectional specimens were loaded in monotonic tension at room temperature and tomography images were obtained while interrupting the loading by holding the displacement during imaging. During the tests, acoustic emission (AE) data were displayed in real time in order to guide image collection. Using this technique, it was possible to interrupt and scan the specimen after a single transverse matrix crack had formed therefore capturing the onset of matrix cracking. It is important to note that the imaging system provided a 3.3 mm × 2.8 mm (width x height) field of view, so only a part of the gauge section of any specimen could be seen at one time. A total of 1025 projection images were acquired for each tomography data set, over a rotation range of 180°, and the total time for each tomography scan was about five minutes. An sCMOS camera (pco.edge, Kelheim, Germany) was used with a 3× lens for magnification. The resultant spatial resolution of the image is 1.3 μm/voxel. Tomographic slices were generated using the commercial reconstruction algorithm Octopus v8 (IIC UGent, Zwijnaarde, Belgium) integrated with image processing tools in ImageJ (US National Institutes of Health, Bethesda, Maryland) and visualized using VG Studio MAX 2.2 (Volume Graphics GmbH, Heidelberg, Germany). The data was reconstructed using a standard filtered-back projection method, taking approximately 1.5 hours for each data set, i.e. each imaged stress increment. The tomography data was collected over a two days of beamtime in both June and November 2016 in collaboration with engineers from GE Research and GE Aviation. However, the interpretation and analyzing of the dataset occurred over the next three years at the University of Michigan.

2.3 Results

2.3.1 Synchrotron Tomography of Unidirectional SiC/SiC CMCs

The resulting stress versus crosshead displacement for both of the imaged unidirectional specimens is shown in Figure 2.2. Stress is meaningful for these un-notched specimens, but the micro-stress field certainly becomes inhomogeneous when fibers begin to break. Because of load train compliance and the lack of use of an extensometer, there is no meaningful measure of strain. It is also important to note that the second unidirectional specimen was weaker than the first by 100 MPa; multiple matrix cracks were seen at 305 MPa in the weaker specimen, whereas the first specimen had no observed matrix cracks at a similar stress of 305 MPa and only one at 340 MPa. The second specimen had an ultimate tensile strength (UTS) of almost 500 MPa, about 16% lower than the 600 MPa sustained by the first specimen. This could well be due to variations in the cross-sectional area along the length of each tensile dogbone, or from the stresses introduced during the processing of the unidirectional specimens.

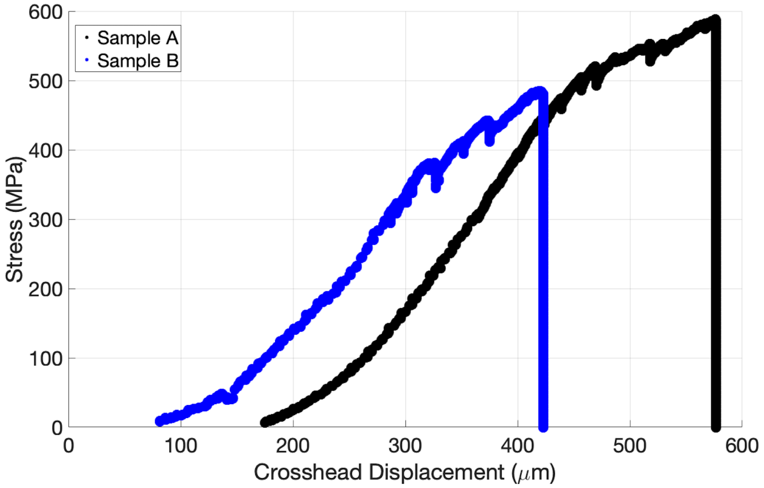

Figure 2.2 Stress vs. crosshead displacement for each unidirectional specimen

In order to create 3D volumes of the specimens, 2D tomographic images, or slices, are stacked together. In generating these tomographic images of laminated composite specimens, three perpendicular planes are of natural interest. These planes are referred to as transverse, sagittal and coronal, as identified in Figure 2.3.

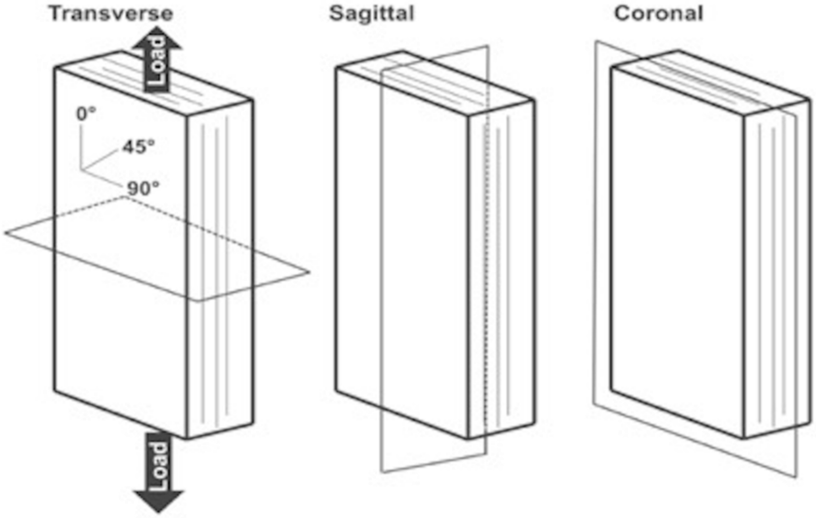

Figure 2.3 Definition of material directions and three natural planes on which to generate cross-sectional images

An unedited coronal tomographic slice from near the center of Specimen 1 before any damage had occurred, at an applied stress of 305 MPa, is depicted in Figure 2.4a. Figure 2.4b shows the same slice at 490 MPa after the onset of matrix cracking. The reconstructed 2-D computed tomography (CT) slices have some phase contrast effect, which enhances the surface of the crack such that it appears bright when the crack opening is very small. Using these tomographic slices allowed for the tracking matrix crack evolution throughout the volume of the specimen as applied load was increased.

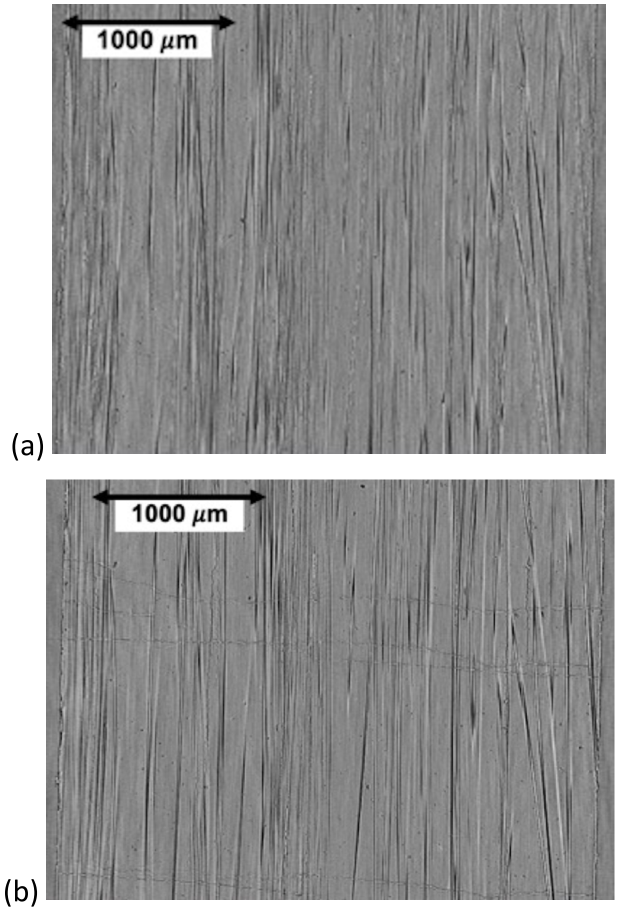

Figure 2.4 (a) Coronal section of Specimen 1 before any known damage (matrix cracking) had occurred at a stress of 305 MPa. This image is unedited in order to depict a general slice out of the 3D volume of the unidirectional specimen (b) Coronal section of Specimen 1 at a stress of 490 MPa where multiple matrix cracks can be observed.

The matrix crack opening wasn't large enough to use segmentation techniques to isolate a single crack through the 3D volume. As a result, a single matrix crack was traced within every individual 2D slice and each slice was then stacked together to create a 3D view of a matrix crack plane. This 3D crack plane is shown in Figure 2.5a, and the specific matrix crack that was manually segmented is shown in Figure 2.5b, depicted by the blue arrows pointing to the top matrix crack in the field of view. It is important to note that most of the figures moving forward were enhanced, such as increasing the contrast and brightness, in order to better see the damage within the images such as the matrix cracks that occurred. If all of the pixels related to a matrix crack were to be segmented it wouldn't be a dense plane as shown in Figure 2.5a but would rather appear discontinuous across the width of the specimens due to the fact that there would be intact, bridging fibers across the crack plane that wouldn't be segmented. Nonetheless, from Figure 2.5a it can be determined that the crack is more complex than a simple linear plane as assumed by many theoretical models. There was significant topography for all of the matrix cracks that appeared in both of the unidirectional specimens. Note that the vertical dimension in Figure 2.5a is different from the horizontal dimensions, to visualize the vertical meandering of the crack over the 400-by-3000 μm nominal crack plane. From the 3D matrix crack, it was measured that the matrix crack extends above and below the average matrix crack measurement location by as much as 150 μm.

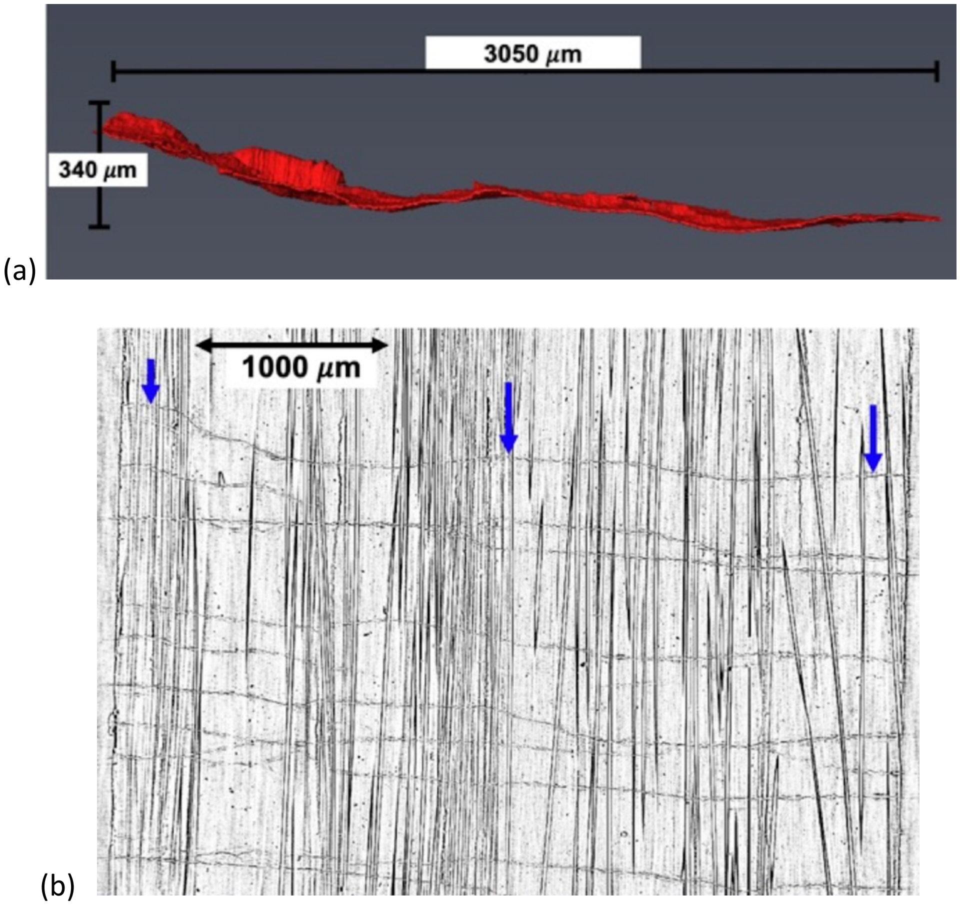

Figure 2.5 (a) 3D matrix crack produced from tracing the matrix crack in every slice within the entire volume of the of the specimen. (b) a single slice from the coronal plane at 550 MPa, with the blue arrows depicting the matrix crack that was traced throughout the volume of Specimen 1 at 550 MPa

2.3.2 Detailed Observations of Damage Evolution Using Micro-CT

Matrix crack measurements were taken along the length of the composite in order to determine an average matrix crack location for each matrix crack and average crack spacing for the specimen within in the imaged field of view. As previously shown, tortuous matrix cracks were observed throughout the 3D volume of the unidirectional specimens. Due to the irregularity of the cracks, the average position of the crack was measured by taking five different measurements in the X direction for every 100 slice increment in the Y direction. Figure 2.6 depicts how the matrix cracks were measured for the UD specimens at one particular slice within the first unidirectional specimen at 550 MPa. The bold line in Figure 2.6 represents a single matrix crack across the through thickness of the specimen, while the five dashed arrows represent the five measurements that were taken to get an average crack position for that crack in that slice.

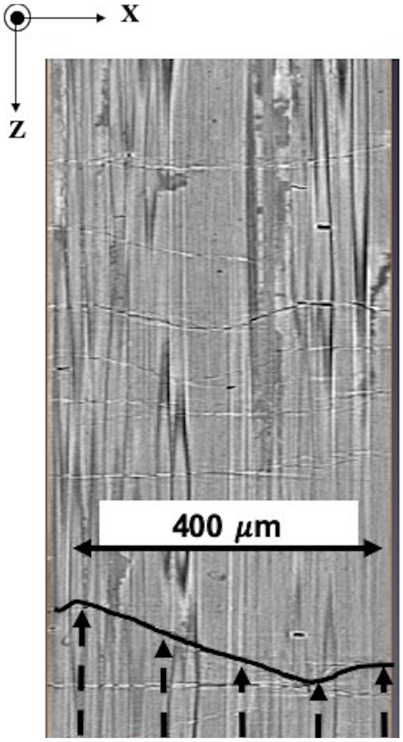

Figure 2.6 Depiction of matrix crack location and measurement

Measuring the matrix crack at multiple locations allowed for the average matrix location to be determined. The number of matrix cracks at each applied stress increment for each specimen is shown in Figure 2.7a along with the measured matrix crack spacing in Figure 2.7b. The number of matrix cracks is presented as a function of each specimen's % failure stress. This was done in order to have a direct comparison between the two specimens since one specimen was weaker than the other and failed at a much lower applied stress. As expected, the number of matrix cracks continues to increase as a function of increasing applied stress due to new matrix cracks appearing within the composite.

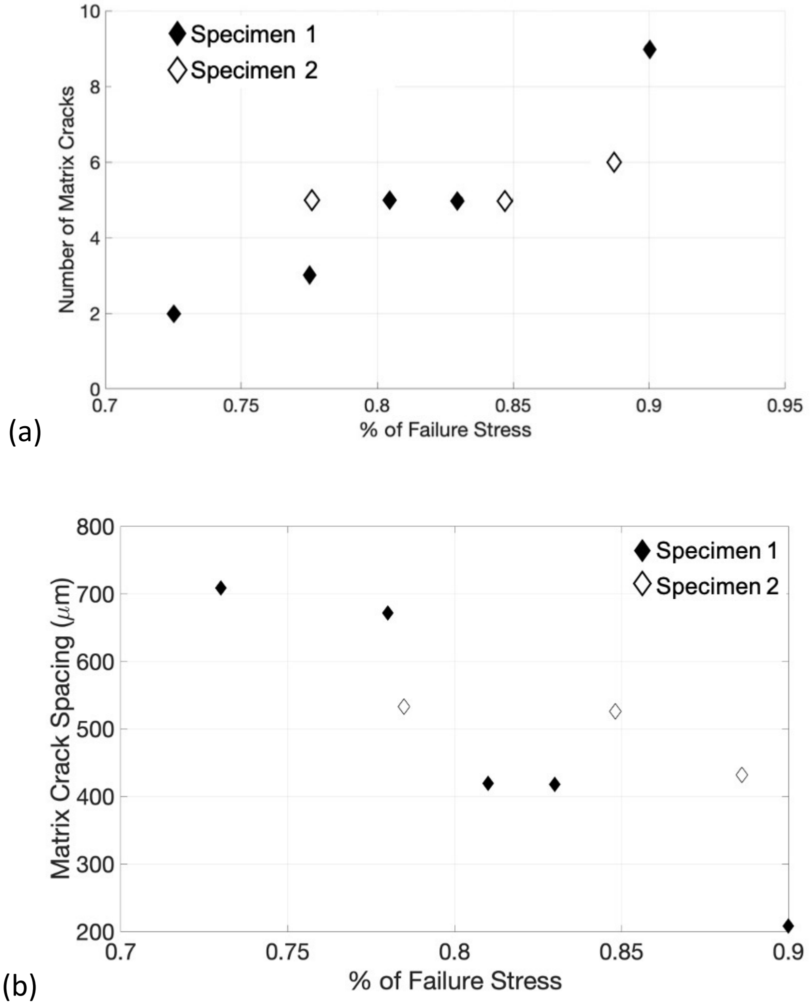

Figure 2.7 (a) The number of matrix cracks at each stress increment for Specimen 1 and Specimen 2 as a function of % of each specimen's failure stress (b) the average matrix crack spacing within each specimen

Individual fiber fragmentations (breaks) and their respective volumes were identified within the volume of the specimen using segmentation techniques. Fiber break openings were calculated from the segmented break volumes determined at each applied stress increment in Avizo assuming 16 μm fiber diameter. Figure 2.8a shows the overall fracture surface of Specimen

1 where fiber pullout is visible in a representative slice. Figure 2.8b represents a region with Figure 2.8b where fiber breaks can be seen. The fragmentation openings appear to be within the same range as the fiber pullout lengths.

(a)

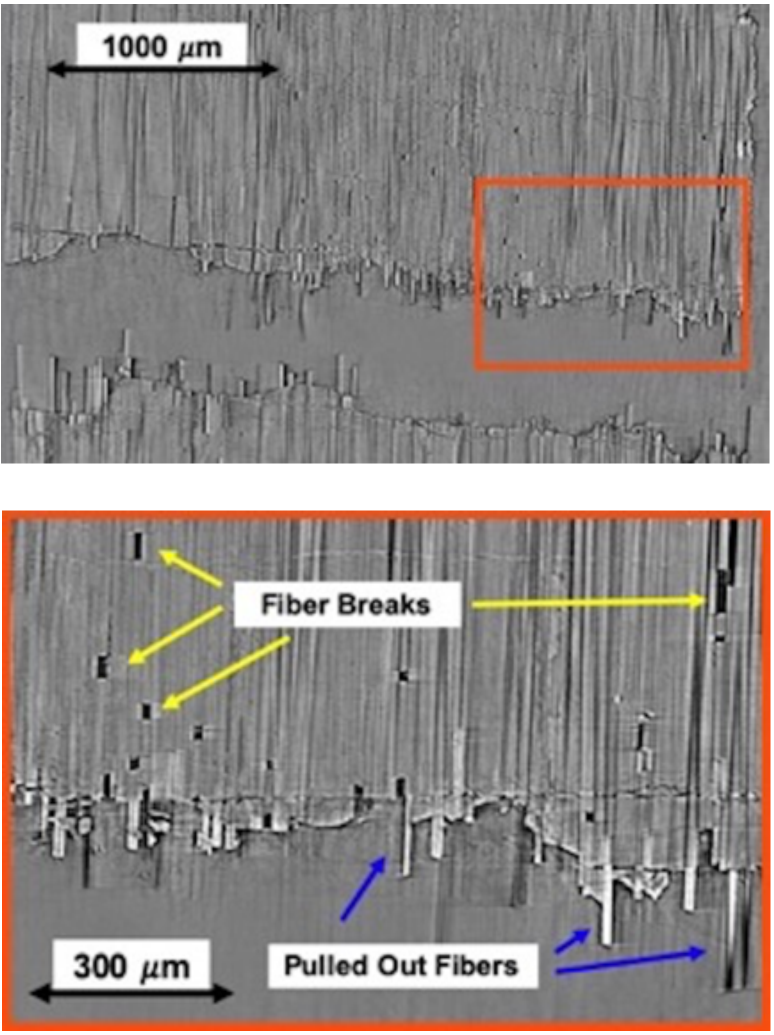

(b)

Figure 2.8 (a) Image of fracture surface shown from slice 131 out of 470, ~92 μm away from the front face of Specimen 1, viewed in coronal plane at 375 MPa where fiber pullout can be observed at the fracture surface (b) Shows the fiber breaks and pulled out fibers with a region where the fiber break opening in relation to fiber pullout can be observed in Specimen 1

For each of the unidirectional specimens, the average fiber break opening as a function of % of their total failure stress is shown in Figure 2.9 with the range bars representing the range of break opening values. Though the fiber break opening appears to increase with stress, the fiber break openings have a large range, with the largest opening being more than ten times larger than the average. At the lower stresses, the fiber break openings are near the resolution value of 1.3 μm/pixel and therefore there is uncertainty in the small fiber break opening values.

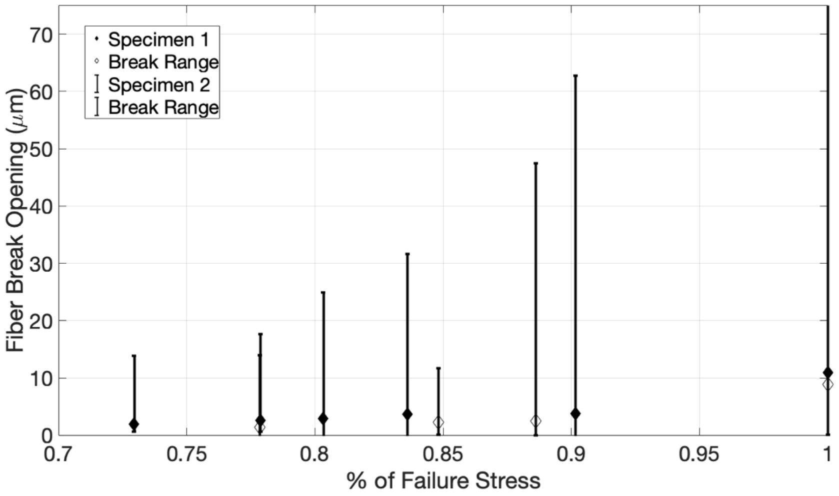

Figure 2.9 Fiber break opening values for each unidirectional specimen as a function of % of failure stress for each specimen with the bars representing the range of fiber break opening values.

In order to better understand the range of fiber fragmentation openings, the distribution of fiber break opening values is shown in Figures 2.10a and 2.10b. for Specimen 1 and Specimen 2 respectively. From these distribution curves it can be seen that the fiber break opening continues to increase as applied stress increases.

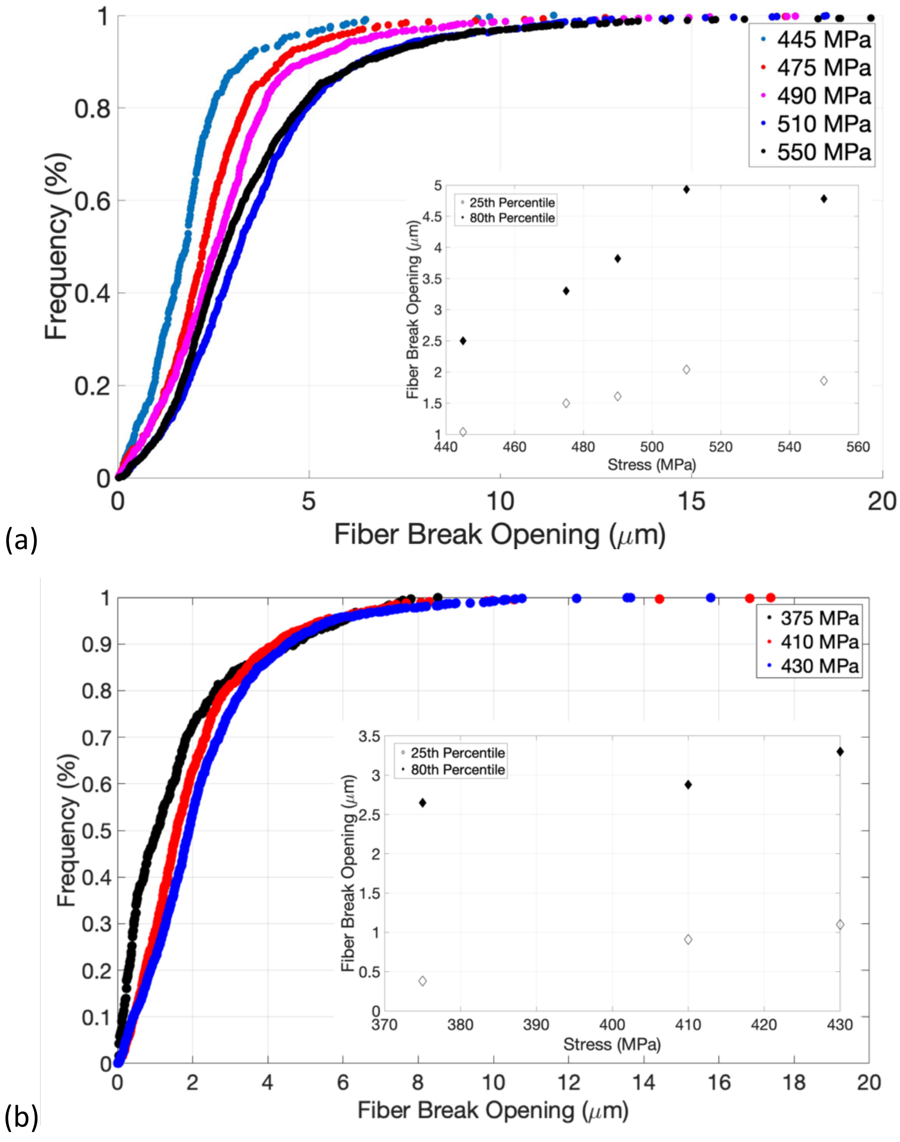

Figure 2.10 (a) Fiber break opening distribution at each stress increment for Specimen 1 with the smaller graph representing the 25th and 80th percentile of fiber break opening at each stress increment (b) Fiber break opening distribution at each stress increment for Specimen 2 with the smaller graph representing the 25th and 80th percentile of fiber break opening at each stress increment

2.4 Discussion

2.4.1 Detailed Behavior of Matrix Cracks

X-ray tomography imaging combined with in situ tensile testing allowed for damage, such as matrix cracking, to be tracked through the volume of each specimen with increasing stress. Matrix cracks first appeared well before the coupon stress/displacement response became visibly nonlinear and matrix cracking continued to appear as long as the specimen was able to carry load. This widespread and continually growing distribution of matrix damage in the form of matrix cracks accounts for the toughness and strain capability of the composite. The specimen failed when enough fiber fragmentations near the location of one crack accumulated to the point where the remaining fibers could not support the load, even though the coupon was being held under displacement control. This process occurred quickly but not instantaneously which is probably due to frictional sliding resistance; the final, isolated load point on the stress-displacement curve shown in Figure 2.2 shows that a full second after the coupon began to lose load-carrying capacity, it was still holding a small amount of load.

For both of the unidirectional specimens, each individual matrix crack was labeled with a letter in order to better track the matrix cracking both through the volume of the specimen and to compare the matrix cracks between each stress increment. For instance, the same crack is labeled A in Figures 2.11 -2.13. The labels do not necessarily indicate the order in which the cracks occurred. Labels are placed at the ends of the cracks (so that the ends can be discerned in the figures) and at several intermediate points.

The first matrix crack appeared in Specimen 1 between 305 and 470 MPa, but likely occurred just below 470 MPa based on AE data collection. By the time the images were taken, the matrix crack had progressed in a translaminar mode across the entire section of the specimen. Figure 2.11 is just one 2D slice out of approximately 550 total slices in the coronal plane of the specimen. This image reveals a normal amount of free silicon in the matrix and very few pores within the volume of the specimen.

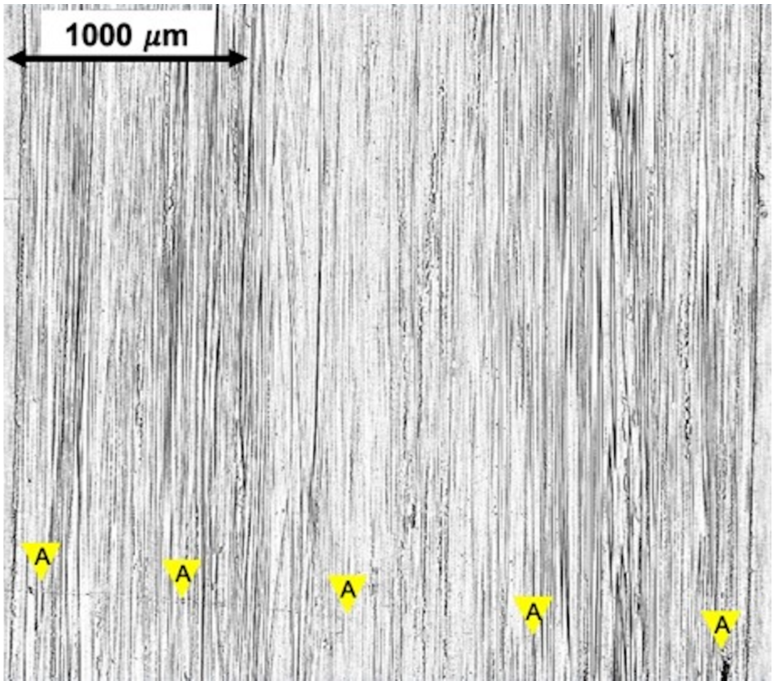

Figure 2.11 First matrix crack, labelled A, that appeared in Specimen 1 between 305 and 470 MPa; slice 197 of 548, shown in the coronal plane ~110 μm from the front

The next image depicted by Figure 2.12 is taken at a stress of 475 MPa. Six more cracks have now formed, and additionally, a pre-existing, silicon-filled process crack oriented along the fiber direction (Crack H) becomes visible. Of the six new translaminar matrix cracks, four of the cracks traverse all the way across the width of the specimen, and Crack F has grown from the right-hand side of the specimen less than halfway across. Crack C has a branch (labeled D) that forms about halfway across the section. Both C and D are through-thickness cracks.

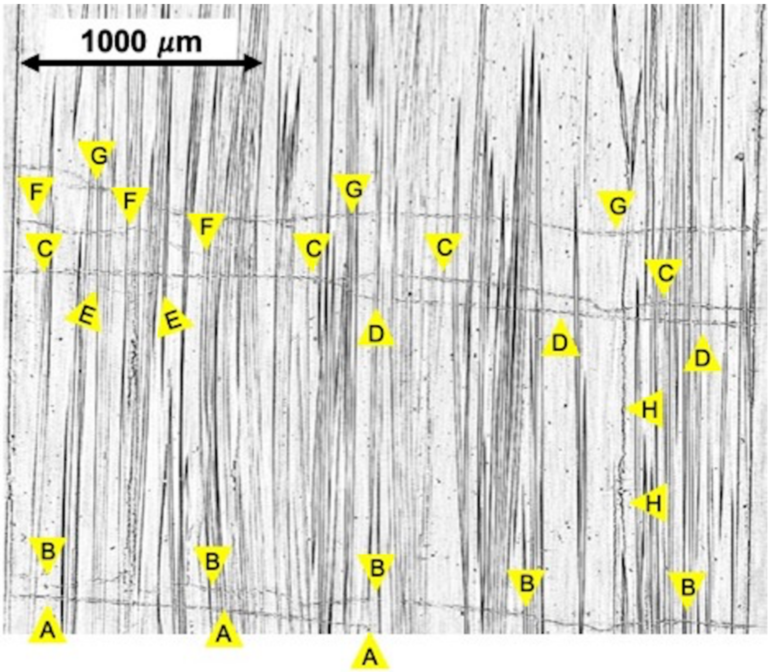

Figure 2.12 Coronal section of Specimen 1 at 475 MPa (slice 181 of 548, ~120 μm from the front face) with cracks marked by lettered arrowheads. The letters do not necessarily indicate the order in which the cracks occurred.

Specimen 1 broke into two pieces at approximately 600 MPa, after which a final imaged dataset was obtained. The final fracture occurred on the left end of Crack B, which had multiple fiber breaks at 445 MPa. A slice depicting the specimen post fracture is shown in Figure 2.13 from the coronal view. There are five new transverse cracks (I through M) that can be seen in detail and occurred directly before failure. Cracks I and J traverse the entire section, while Crack K's path has been obscured by Crack B, which is the crack on which complete fracture occurred. Crack A, which was the first to form, can still be seen beneath Crack B, but its path is also disrupted by the final fracture surface. Part-width cracks E and F do not appear to have lengthened since the previous image at 490 MPa, but E has a bigger opening. Two new through-thickness cracks, L and M, have grown from the left surface but not across the entire section. All of the cracks, including the final fracture, are complex and tortuous but in general are nearly perpendicular to the loading direction. The cracks remain visible after failure and unloading, whereas in optical microscopy, residual fiber tension often causes unloaded matrix cracks to close to a small enough opening that they can no longer be detected. Substantial pullout (up to 0.1 mm) can also be seen between Cracks B and J.

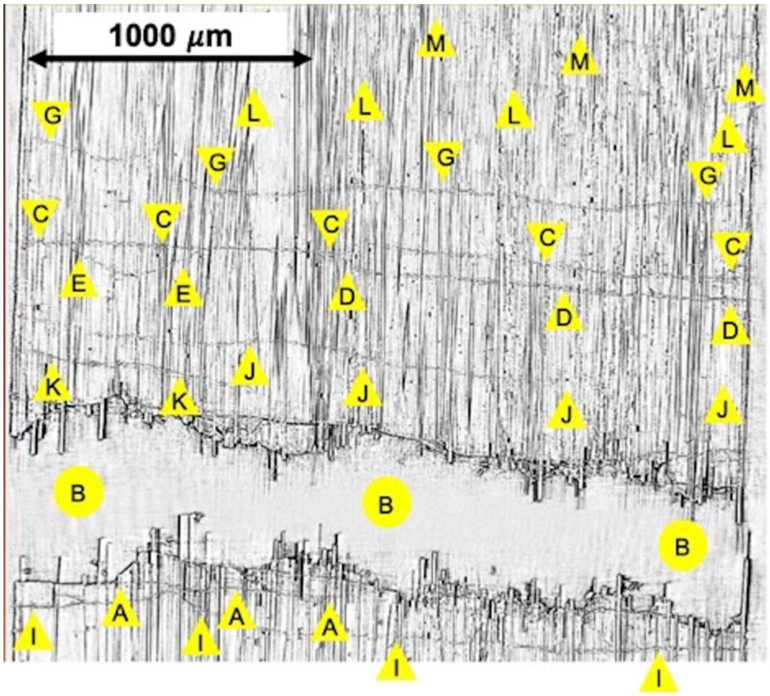

Figure 2.13 Coronal section of Specimen 1 after failure at 610 MPa; slice 404 of 548, ~280 μm away from the front face.

Most analytical models assume that in an un-notched unidirectional specimen such as this, transverse matrix cracks propagate across the entire section in a brittle, near-instantaneous manner.[15] However, there are matrix cracks shown in both Figures 2.12 and 2.13 that do not traverse the entire section, which indicates some departure from this assumption. Still, most of the cracks observed throughout the volume had propagated through the entire thickness of the specimen by the first time they were imaged.

For the second specimen, images of the side-by-side coronal and sagittal sections are presented so that the progression of the cracks in two different planes can be observed. Figure 2.14a, about 92 μm away from the front face, shows that five matrix cracks occurred at a stress of 430 MPa. Cracks A, B and C completely traverse the specimen, while Crack D has grown from the left about halfway across and Crack E has done the same from the right but at a slightly higher location. Referring to the sagittal section in Figure 2.14b (slice 1208 of 2555 that is about 1600 μm from the front of the sagittal face), it can be seen that although Cracks A and D propagated across the coronal face they had not penetrated through the entire thickness. Crack E cannot be seen at all, because the sagittal section was taken slightly left of center at the location indicated by the vertical dotted line in Figure 2.14a.

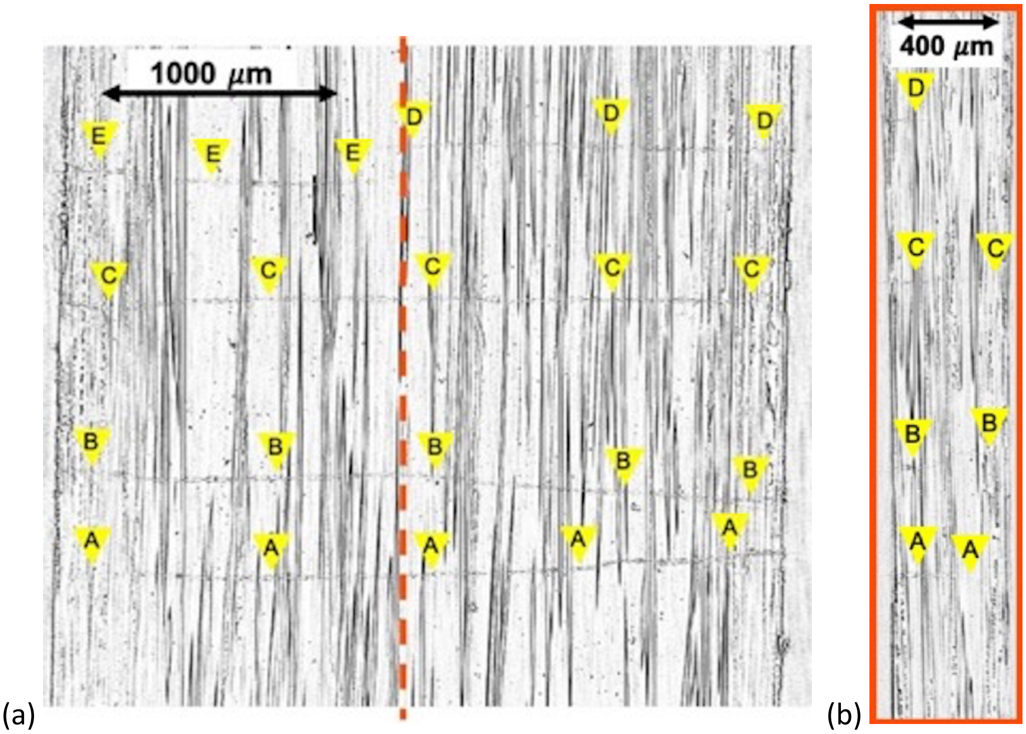

Figure 2.14 (a) Matrix cracking shown in slice 131 out of 470, ~92 μm away from the front face of Specimen 2, viewed in coronal plane at 375 MPa with the dashed line representing the location the second image. (b) Matrix cracking shown in slice 1208 out of 2555, ~1414 μm away from the side face of Specimen 2, viewed in the sagittal plane at 375 MPa.

Figures 2.15a and 2.15b show the crack pattern at 430 MPa. Seven more cracks have appeared (Cracks F through L) and some of the cracks seen at the previously imaged load level have progressed. Crack D is now visible not only across the entire coronal section, but it has also penetrated the entire thickness shown in the sagittal section image. However, Crack E does not appear to have progressed. Of the new cracks, only Crack J traverses the entire coronal section. Cracks F and K grow from the left, while Cracks E, G and H grow from the right. Cracks G and L appear not to intersect either edge. Cracks M and N can be seen in the sagittal section but not the coronal one.

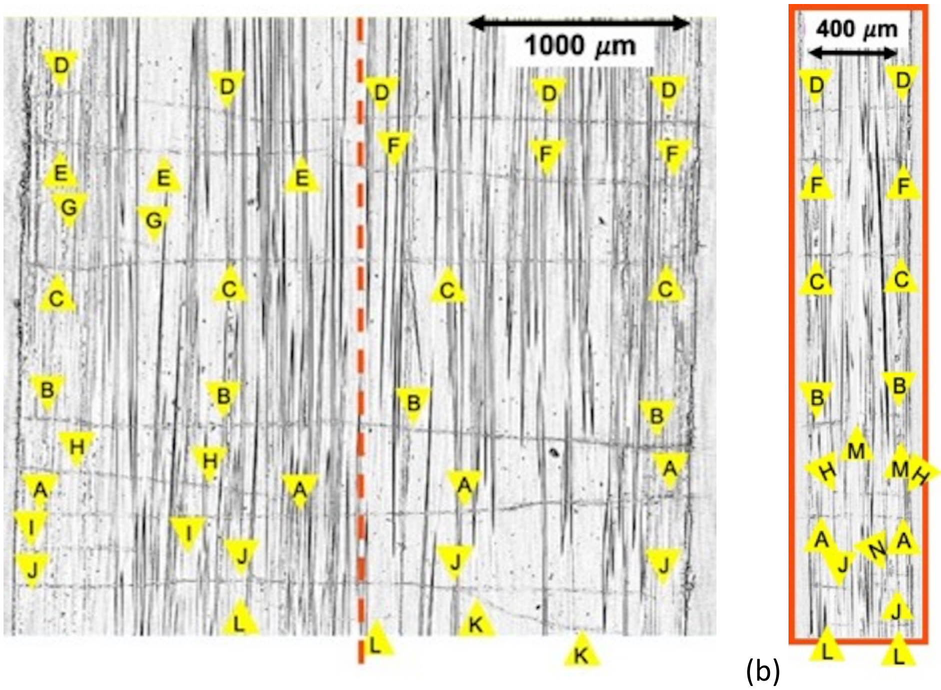

(a) (b)

Figure 2.15 (a) Matrix cracking shown in slice 146 out of 501, ~85 μm away from the front face of Specimen 2, viewed in the coronal plane at 430 MPa with the dashed line representing the location of the second image. (b) Matrix cracking shown in slice 1277 out of 255, ~1009 μm away from the side face of Specimen 2, viewed in the sagittal plane at 430 MPa.

The first unidirectional specimen had a clean fracture surface caused by one distinct matrix crack. The second unidirectional specimen's fracture surface, shown in Figures 2.16a and

2.16b, shows that fracture follows Crack B about halfway across the section, where it then takes a sharp downward turn along the fiber direction and then continues translaminarly until it leaves the field of view. Of note, during its downward turn it passes four pre-existing cracks (H, A, I and J) any one of which seems like it could have provided a path for the fracture to continue rightward. But the failure surface does not turn back translaminarly until it reaches an area of matrix that apparently was still intact at 430 MPa in Figure 2.16. Crack turning along the fiber direction is usually an undesirable characteristic of unidirectional composite tensile testing, but with the double-reduced specimen, it was seen that the cracking in the fiber direction was delayed until multiple matrix cracks had already propagated.

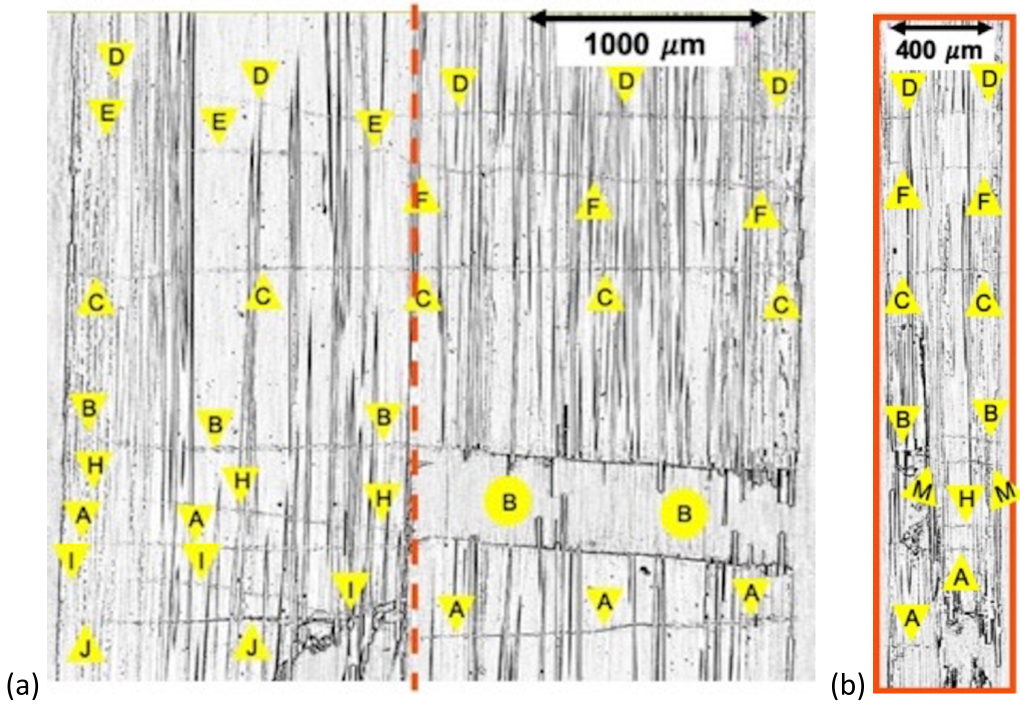

Figure 2.16 (a) Matrix cracking shown in slice 141 out of 501, ~92 μm away from the front face of Specimen 2, viewed in the coronal plane after failure with the dashed line representing the location of the second image (b) Matrix cracking shown in slice 857 out of 2555, ~1023 μm away from the side face of Specimen 2, viewed in the sagittal plane after failure

The vertical crack in the fracture surface shown in Figure 2.17a can be observed looking down on the transverse plane highlighted by the yellow horizontal line. Examining this single transverse slice in Figure 2.17b, the vertical crack from the transverse plane did not reveal any clear microstructural cause for the vertical turn in the crack. There is a large vein of free silicon running through the thickness several fiber diameters to the left of the crack, but the silicon vein does not intersect the crack in this view and in general, there has been no correlation between free silicon and matrix cracks. Broken fibers are easily identifiable as dark holes in the transverse plane as also shown in Figure 2.17b. The vertical jog likely happened because the resistance to matrix cracking is significantly lower along the fiber axis than across the fiber diameter. If one imagines the crack proceeding translaminarly from the left, secondary shear stresses build up the longer the crack gets, and eventually these are high enough to cause the crack to run along the fibers. However, it is less clear as to why the crack only jogged a short distance before turning translaminar again, and why the crack in this specimen turned but the one in the previous specimen did not. It is possible that a translaminar crack below Crack J was already approaching from the right and intersected the vertical crack before it could run to the end of the specimen.

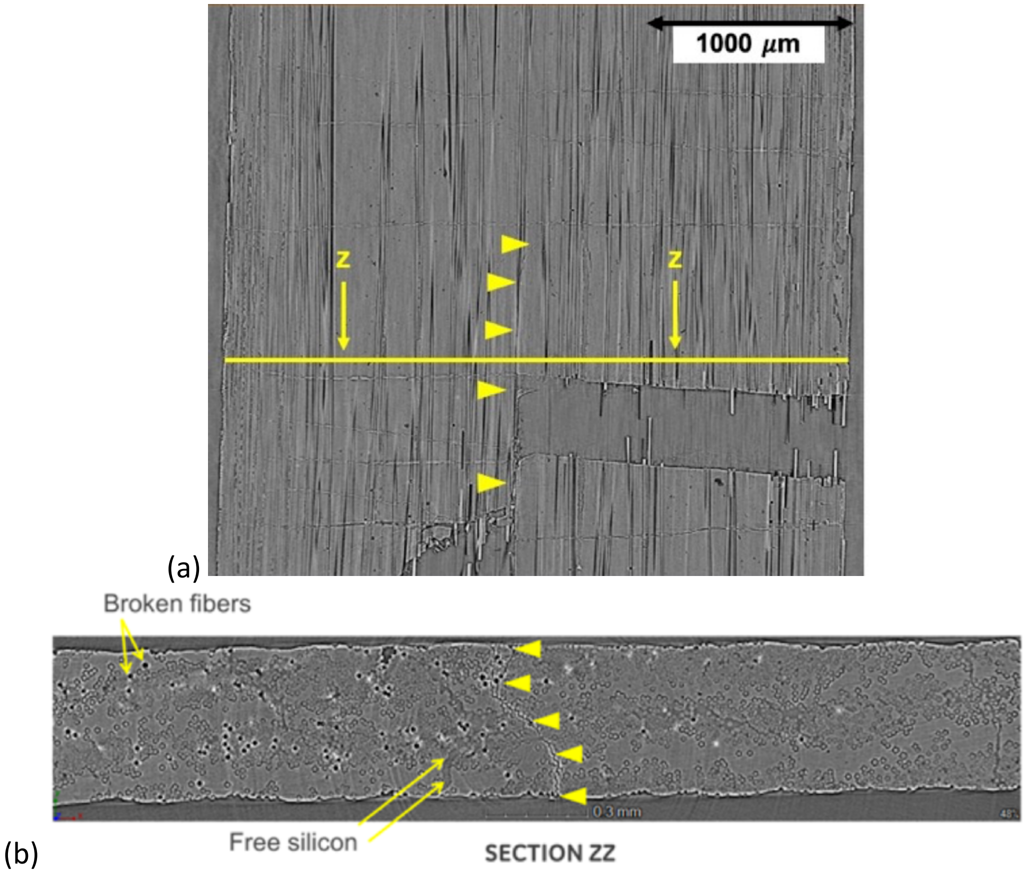

Figure 2.17 (a) Vertical crack and location of transverse section. (b) Transverse section through vertical crack, showing broken fibers (which appear as holes) and a vein of free silicon near, but not intersecting, the vertical crack. The yellow arrows indicate the position of the transverse crack in each image.

2.4.2 Quantification of Matrix Cracking

Crack spacing is a quantity of interest in modeling because substantial matrix cracking is necessary for the material to have toughness and strain capability. For Specimen 1, the matrix crack spacing is approximately 700 μm between 70-75% of the specimen's failure stress and the matrix crack spacing decreased with stress down to a matrix spacing of 200 μm at 90% of the specimen's total failure stress. As discussed earlier, Specimen 2 was weaker than Specimen 1 and had fewer matrix cracks appear at similar stress increments. At lower % of failure stress, Specimen 2 had a smaller matrix crack spacing because there were more matrix cracks in the field of view. However, as load was applied, more matrix cracks occurred in Specimen 1, and from 80% of total failure stress all the way to fracture Specimen 1 had a smaller matrix crack spacing. Between 75% and 80% of both of the specimens' failure stress, the matrix crack spacing was 500 and 700 μm. For the matrix crack spacing values, only matrix cracks that propagated across the entire face and through thickness were evaluated. There were matrix cracks that did not traverse through the entire specimen and there were indications that the cracks could have continued forming but for the fiber-governed ultimate failure that terminated the test. If the 0° plies tested here had been incorporated into a cross-ply laminate as is usual in applications, tunnel cracks in the 90° plies would abet the formation of matrix cracks in 0°, which is a synergetic effect that increases toughness. Plies that result in the best cross-ply laminate toughness will be less tough (but of course stronger) when tested alone. A more in depth look into the mechanics behind the matrix crack spacing will be discussed in Chapter 3.

2.4.3 Fiber Break Opening Observations

Damage accumulation such as matrix cracking and fiber breaks can be seen using X-ray tomography techniques and the data acquired from the images can be quantified. For example, due to the contrast of the fiber breaks to the material's X-ray attenuation, fiber breaks can be easily identified throughout the volume of the specimen. These break locations relate to fiber pullout on the final fracture of the specimen. For each of the unidirectional specimens, both small and large fiber pullout can be observed along the fracture surface as seen in Figure 2.8 with arrows pointing to both fiber pullout and fiber breaks in the post fracture specimen. Pulled-out fibers as long as 0.3 mm were observed protruding from the fracture surfaces. Several breaks with smaller distances from the fracture plane (about 0.02 mm) can be seen near matrix cracks distant from the final failure plane. It was observed through the volume of the specimen that multiple fiber breaks may occur in the same fiber which is possibly due to fibers having a reduced ability to move relative to the matrix due to locally inadequate coating reducing debonding, such that one crack is not enough to unload the fiber along its entire length.

Fiber fragmentation opening measurements were obtained for each fiber break that was segmented through the volume of each specimen and it can be seen in Figure 2.8 that these openings increase with stress. The average fiber break opening for both specimens is shown in Figure 2.9 with the bars representing the range of breaks. It can be seen that although the average fragmentation opening post fracture was approximately 10 μm, the openings ranged from 2 μm all the way to 300 μm. At lower stresses, between 75% and 80% of each specimen's failure stress, the average fiber break opening was measured at approximately 3 μm which is nearing the resolution of the micro-CT images. Whereas the largest fiber break opening measured between 75-80% of failure stress was about 15 μm. Fiber breaks measured post-fracture had average opening values of 10-12 μm.

Figure 2.10a shows the fiber break opening distribution for each stress increment along with the 25th and 80th percentiles for each stress increment measured in Specimen 1. It can be seen that the 80th percentile increases from 2.5 μm at 445 MPa to 5 μm at an applied stress greater than 500 MPa. It can be seen that fiber break openings continue to increase as applied stress was increased. The increase in fiber break opening values is due to new fiber breaks at higher stresses having larger openings than those that occurred at lower stresses, and the fibers that were broken at lower stresses continue to open as stress is applied. However, it can be seen in Figure 2.10b that the fiber break openings in Specimen 2 didn't increase as much as Specimen 1. This could due to higher frictional sliding that may also contribute to the lower ultimate tensile strength of Specimen 2 compared to Specimen 1.

The matrix crack opening displacement as a function of stress is of interest in micromechanical modeling. The comparison of a typical fiber break opening and the opening of the matrix crack can be seen in Figure 2.18. The imaging method used here does not resolve the crack opening well until complete separation and it can be seen in Figure 2.18 that the fiber break opening is not necessarily comparable to the opening displacement of the matrix crack. The opening of the matrix crack was never discernable in the x-ray tomography images however the fiber breaks were easily visible and able to be quantified.

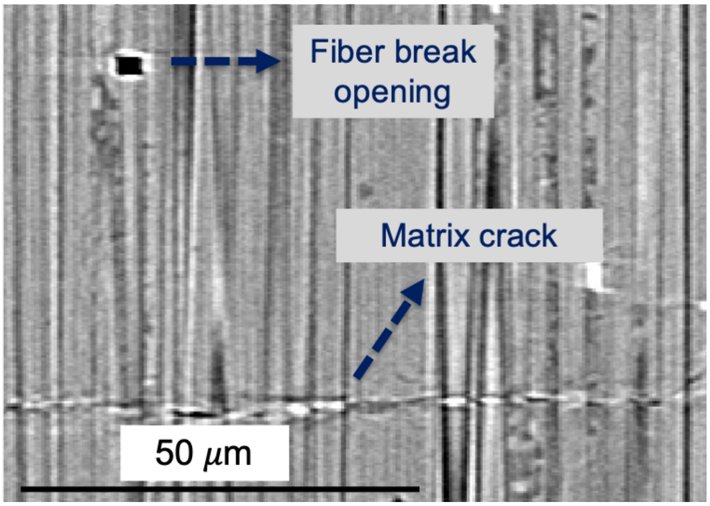

Figure 2.18 Comparison between the opening of a fiber fragmentation and the opening of the matrix crack in a tomography slice within the volume of Specimen 1

2.5 Summary

In summary, using a hard X-ray beam at the Advanced Light Source, Lawrence Berkeley National Laboratory, microscopic damage processes were observed in unidirectional SiC/SiC ceramic matrix composite laminates loaded monotonically in tension at room temperature in laboratory air. The unidirectional laminate was tested using a novel double-reduced dogbone to facilitate observations of damage evolution in a unidirectional architecture produced using realistic processing methods. Damage such as matrix cracks and fiber breaks were tracked as load was applied to the specimens.

Most models assume the matrix cracks to be planar through thickness cracks. But from observations in this study, matrix cracks appeared in both of the unidirectional specimens that did not transverse across the entire width of the specimens therefore disputing the idea that transverse matrix cracks propagate across the entire section in a brittle, near-instantaneous manner. It should also be noted that matrix crack bifurcations were also observed throughout the volume of both specimens. Creating a 3D plane of a particular matrix crack through the volume of the specimen allowed for the non-planar crack to be measured and it was determined that a matrix crack can vary as much as 150 μm in height from the matrix crack's average measured location. The stress state varies as distance from a matrix crack plane and if the matrix crack plane itself is varying, or contains bifurcation, it could affect the models and make them less realistic. The next chapter will provide a more in-depth comparison between quantitatively observed composite damage and mechanical model predictions. While tracking the matrix crack progression throughout the volume of both specimens, it was noticed that Specimen 1 had a uniform planar fracture due to one specific matrix crack while Specimen 2 displayed a sharp vertical turn in its final crack path that caused fracture. This sharp turn could not be associated with any microstructural features that could be seen within the scans obtained.

Using micro-CT techniques, damage such as matrix crack spacing and fiber break opening were quantified. Matrix crack spacing was determined for both specimens with the weaker specimen, Specimen 2, having more matrix cracks and a smaller matrix cracking spacing at lower stresses but ultimately failing with a larger matrix crack spacing. The openings of fiber breaks were quantified using segmentation techniques. For both specimens tested, the distribution of fiber break openings increased as a function of increasing stress. Both specimens had average opening values less than or equal to 5 μm until failure where the average opening value increased to approximately 10 μm. This is due both to original fiber break openings continuing to increase with applied load and because fiber breaks that occur at higher stresses often exhibit a larger initial break opening value. It is also worth noting that it was observed that a few fibers were broken in more than one place near a single matrix crack.

References

1. Marshall DB, Cox BN, Evans AG. The mechanics of matrix cracking in brittle-matrix fiber composites. Acta Metallurgica 1985;33(11):2013-2021.
2. Aveston J, Cooper A, Kelly A. Single and Multiple Fracture: The properties of fiber composites. IPC Science and Technology Press; 15-26:1971
3. Thouless MD, Evans AG. Effects of pull-out on the mecanical properties of ceramic-matrix composites. Acta Metallurgica 1988;36(3):517-522.
4. Budiansky B, Hutchinson JW, Evans AG. Matrix fracture in fiber-reinforced ceramics. J Mech Phys Solids 1986;34(2):167-189.
5. Curtin WA, Ahn BK, Takeda N. Modeling brittle and tough stress-strain behavior in unidirectional ceramic matrix composites. Acta Mater 1998;46(10):3409-3420.
6. Morscher GN, Gordon NA. Acoustic emission and electrical resistance in SiC-based laminate ceramic composites tested under tensile loading. J Eur Ceram Soc 2017;37(13):3861-3872.
7. Sevener KM, Tracy JM, Chen Z, Kiser JD, Daly S. Crack opening behavior in ceramic matrix compsoites. J Am Ceram Soc 2017;100(10):4734-4747.
8. Sørensen BF, Talreja R. Analysis of Damage in a Ceramic Matrix Composite. Int J Damage Mech 1993;2(3):246-271.
9. Zok F, Hom CL. Large scale bridging in brittle matrix composites. Acta Metallurgica Et Materialia 1990;38(10):1895-1904.
10. Chateau C, Gélébart L, Bornert M, Crépin J, Caldemaison D, Sauder C. Modeling of damage in unidirectional ceramic matrix composites and multi-scale experimental validation on third generation SiC/SiC minicomposites. J Mech Phys Solids 2014;63(1):298-31

11. Bale H, Blacklock M, Begley MR, Marshall DB, Cox BN, Ritchie RO. Characterizing three-dimensional textile ceramic composites using synchrotron X-ray micro-computed-tomography. J Am Ceram Soc 2012;95(1):392-402.
12. Bale HA, Haboub A, Macdowell AA, Nasiatka JR, Parkinson DY, Cox BN, et al. Real-time quantitative imaging of failure events in materials under load at temperatures above 1,600°C. Nat Mater 2013;12(1):40-46.
13. Larson NM, Zok FW. In-situ 3D visualization of composite microstructure during polymer-to-ceramic conversion. Acta Mater 2018;144:579-589.
14. Maillet E, Singhal A, Hilmas A, Gao Y, Zhou Y, Henson G, et al. Combining in-situ synchrotron X-ray microtomography and acoustic emission to characterize damage evolution in ceramic matrix composites. J Eur Ceram Soc. 2019; 39(13):3546-3556.
15. Curtin WA. Theory of Mechanical Properties of Ceramic-Matrix Composites. J Am Ceram Soc 1991;74(11):2837-284

[2]Chapter III. Measuring the Evolution of Damage Mechanisms within Unidirectional SiC/SiC CMCs

3.1 Introduction

Ceramic matrix composites are of importance within the aerospace industry because of their unique high temperature capability and improved toughness when compared to traditional ceramics. However, because of their complicated microstructure it is important to better understand how damage evolves in these materials under mechanical loading. The three main types of damage in these materials are matrix cracking, fiber fragmentations, and debonding along the fiber/matrix interface. There have models to describe the evolution and onset of matrix cracking and subsequent interfacial debonding.[1-7] Many studies have also been performed to better understand fiber fragmentation, pullout of broken fiber fragmentations and the fiber strength distributions.[8-12] Some assumptions are made for these models to be accurate: 1) fibers are assumed to be straight and uniformly distributed 2) the matrix is treated as a fully dense uniform phase, 3) the matrix and fibers are assumed to be mechanically coupled through frictionally-sliding interfaces, 4) most of the constituent properties such as the interfacial sliding resistance, fracture toughness, and elastic moduli are presumed to be deterministic and lastly 5) fiber strength

---

[2] Most of this chapter was published as a paper in the Journal of the American Ceramic Society on January 15, 2020 and has been reformatted for dissertation format with additional data incorporated

is considered to follow a Weibull distribution. Although theoretical mechanical models have predicted matrix cracking and fiber fragmentation, very few studies have been able to experimentally observe the evolution of this damage *in-situ* and correlate the relationship between matrix cracking fiber fragmentations. Using micro-CT image analysis for this work, detailed observations of fiber breaks at increasing stress increments were analyzed and compared to the location of the matrix cracks that were observed through the volume of each specimen.

3.2 Methods and Materials

The synchrotron and micro-CT tensile set up was previously described in Chapter 2. The unidirectional un-notched samples loaded in tension consisted of two 0° plies and were obtained by face-grinding of the original eight-ply unidirectional samples until only the two center longitudinal plies remained. This was done to promote failure in the scanned volume by reducing thickness in the center of the gauge section. For the reconstruction, the x-ray tomography images were reconstructed using TomoPy[13] in standard filtered back-projection mode. The reconstructed images were visualized in VG Studio MAX 2.2 (Volume Graphics, GmbH) and image segmentation was done using Avizo Fire 8.1.1 (FEI, Thermo Fisher Scientific). The present study focuses on two principal damage mechanisms: fiber breaks and matrix cracking.

3.2.1 Segmentation of Fiber Breaks

Fiber fragmentations were relatively easy to distinguish and segment in tomography images, due to the high contrast between a dark fiber break (air) and the light grayscale of the rest of the composite (SiC fibers in a SiC matrix). The BN fiber coatings have a low x-ray attenuation coefficient, which makes them appear very similar to fiber breaks in tomography images which can cause the fiber fragmentation segmentation process to include fiber coatings (especially thicker coatings) in addition to the segmented fiber breaks. For segmentation, the fiber fragmentations or breaks were manually selected with the aid of thresholding tools such as Magic Wand in Avizo and the centroid and volume of each fiber break were reported. The height of each detected fiber fragmentation was estimated using the volume obtained from segmentation, assuming a fiber radius of 15 μm .

3.2.2 Matrix Crack Measurements

Matrix crack lengths were measured manually using Avizo Fire 8.1.1. and ImageJ. Theoretically the matrix crack opening (crack opening displacement) would show up similarly to that of fiber fragmentations with the gap between matrix crack faces being air and therefore having a dark contrast in X-ray tomography images. The matrix crack opening of these unidirectional specimens was extremely small, in most cases the opening was below the resolution limit for the imaged datasets. Phase-contrast effect allowed for the matrix cracks to appear as faint white lines (i.e. the matrix cracks that appear in Figure 3.4). Matrix cracks locations were measured within the volume of these unidirectional specimens, by viewing tomography images of the samples thickness and taking five measurements at every 100-slice increment within the specimen (approximately 2600 slices total in the sagittal plane).

3.3 Results and Discussion

Two unidirectional (UD) specimens were imaged at increasing stress increments while under tensile load using synchrotron tomography. The stress increments at which the two specimens (arbitrarily labeled Specimen 1 and Specimen 2) were imaged, are listed in Table 3.1. below.

Table 3.1 Two unidirectional specimens were scanned and imaged at increasing stress increments listed below

Specimen 1	Specimen 2
305 MPa	335 MPa
400 MPa	350 MPa
445 MPa	375 MPa
475 MPa	410 MPa
490 MPa	430 MPa
510 MPa	480 MPa: Failed
550 MPa	
610 MPa: Failed	

The stress-displacement curves produced from each tested specimen were shown and discussed in Chapter 2 but it is important to note that the one specimen failed at a stress 100 MPa lower than the other one and the two specimens had very different fracture planes. The apparatus used for these experiments was displacement controlled and Figures 3.1a and 3.1b show the load and displacement vs. time for Specimen 1 and Specimen 2 respectively. On these displacement curves, the hold time required for x-ray imaging can be discerned from the areas where there was no change in the crosshead displacement which indicates that the imaging process could take between 10-20 minutes.

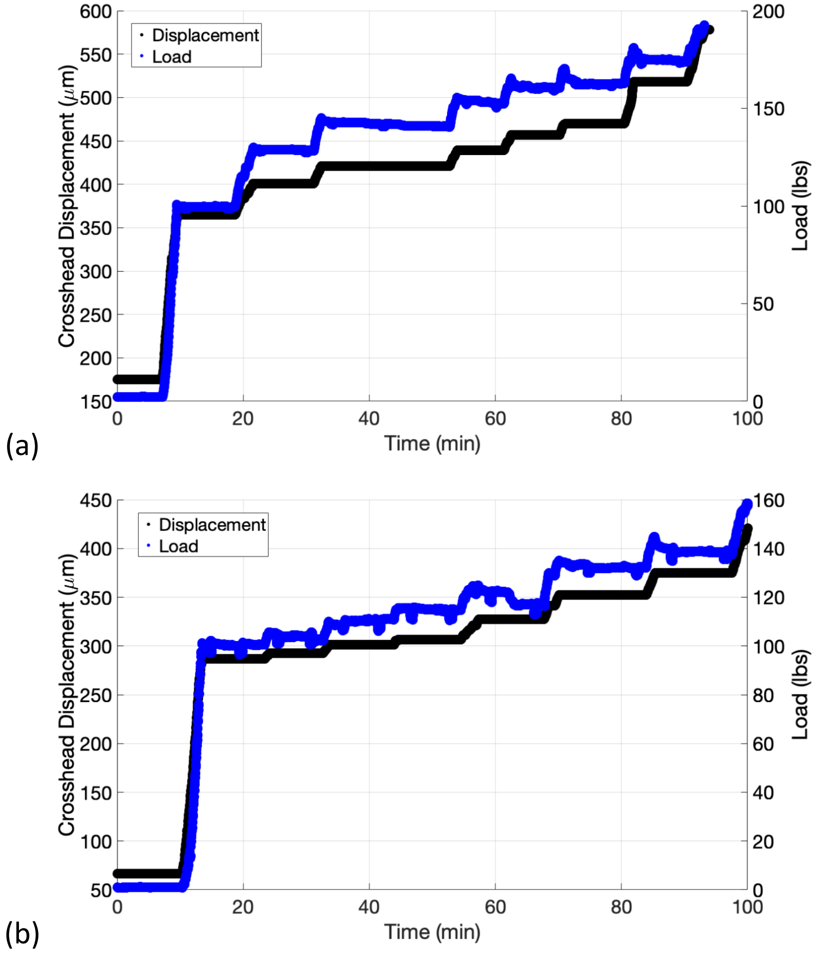

Figure 3.1 (a) Crosshead Displacement and Load vs. Time for Specimen 1 (b) Crosshead Displacement and Load vs. Time for Specimen 2

A 3-D image of the overall volume of the unidirectional specimen that was obtained using synchrotron imaging is depicted in Figure 3.2. In this 3D image, the fibers are running in a vertical direction to form the two 0° plies. Fibers that were damaged during polishing can also be seen extended near the edge of the volume of the specimen. In order to analyze damage within the specimen, single 2D images (slices) are viewed from within the entire volume of the 3D image stack.

Figure 3.2 3-D view of unidirectional Specimen 1

CMCs exhibit linear elastic behavior before any damage occurs, as was described in Chapter 1. Values for the modulus of SiC fibers and SiC matrices found in the literature are reported to be 380-420 GPa and ~340-380 GPa respectively.[15-17] Using an elastic modulus of 360 GPa and 400 GPa for the matrix (E_m) and fibers (E_f) respectively, results in a composite modulus (E_c) of 371 GPa by using rule of mixtures. At an applied stress (σ) of 200 MPa, before any damage occurs within the specimen, the sample can be assumed to have linear-elastic behavior and isostrain conditions where Equation (3.1) can be used to approximate the matrix stress (σ_m) as 194 MPa and the fiber stress (σ_f) as 216 MPa. The stress in both the fiber and the matrix, before matrix cracking occurs, is of similar value because both constituents (fiber and matrix) have comparable elastic moduli values since they are both made up of primarily SiC.

$$\frac{\sigma}{E_c} = \frac{\sigma_f}{E_f} = \frac{\sigma_m}{E_m} \tag{3.1}$$

3.3.1 Comparing Observed Matrix Crack Spacing to Mechanical Models

The matrix crack spacing measured at each stress increment for each specimen was previously shown in Chapter 2. However, many mechanical models are compared to observed matrix crack spacing and therefore the matrix crack spacings measured in these unidirectional specimens are emphasized again in Figure 3.3. In order to be able to directly compare the two specimens, since Specimen 2 was weaker than Specimen 1, the matrix crack spacing is shown as a function of the % of failure stress. As expected, the general trend for the matrix crack spacing is that the spacing decreases as a function of increasing stress due to new matrix cracks appearing in the composite.

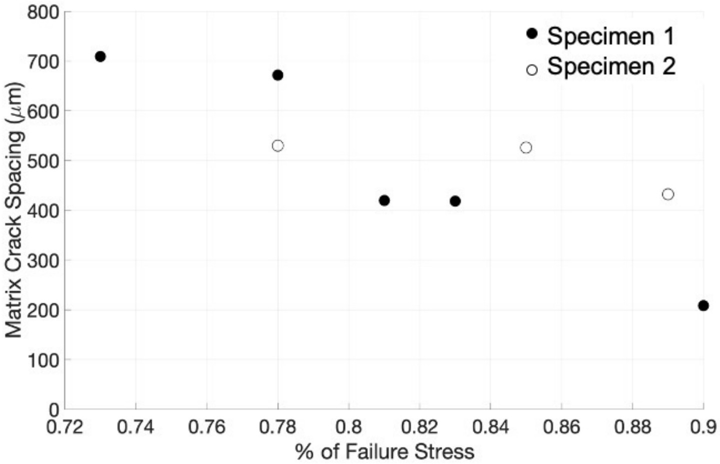

Figure 3.3 Matrix crack spacing for each specimen as a function of their respective % of failure stress

Although the matrix crack spacing decreased as a function of applied stress for both specimens, they each demonstrated different matrix cracking behaviors. For Specimen 1, the initial matrix crack spacing at 445 MPa, when there were only two cracks in the field of view, was approximately 700 μm. However, at 510 MPa (83% of failure stress) the matrix crack spacing was

420 µm and by 550 MPa the final matrix crack spacing, directly before failure was 208 µm. This observed matrix crack spacing corresponds well to published results by Chateau et al. who used micro-CT to study damage accumulation in SiC/SiC mini composites and reported a final matrix crack spacing values of 250 µm.[18] The matrix cracking behavior observed in Specimen 2 showed minimal change after the initial matrix cracking was imaged at 375 MPa. Initially one matrix crack was observed throughout the volume of Specimen 1. As applied stress increased, number of total matrix cracks within the field of view gradually increased with each stress increment (details presented in Chapter 2). In comparison, Specimen 2 initially had four matrix cracks identified within the field of view and directly before the specimen failed, its total number of matrix cracks only increased to five matrix cracks which resulted in only a minor change in the overall matrix crack spacing. The initial matrix crack spacing measured in Specimen 2 was approximately 550 µm and at its highest applied stress before failure the matrix crack spacing decreased by approximately 100 µm to result in an overall crack spacing of 430 µm.

Using the number of matrix cracks observed along the length (height) of the specimen in the field of view (2.8 mm), the matrix crack densities for both specimens were determined. The matrix crack density for Specimen 1 was initially 0.67 cracks/mm and increased to 3.0 cracks/mm at 400 MPa and 550 MPa respectively. Since Specimen 2 did not exhibit a large change in the matrix cracking behavior it only increased from 1.67 cracks/mm to 2 cracks/mm at the highest imaged applied stress. The matrix crack densities of each specimen are comparable to previously published results for SiC/SiC measured by using acoustic emissions during tensile testing.[19] For Specimen 2, the matrix crack spacing between each additional crack is more uniform than

Specimen 1, however there were fewer observed matrix cracks, and this is likely due to the specimen failing before matrix crack saturation had been attained.

Matrix cracking occurs with simultaneous debonding between the fiber and matrix interface and theories suggest that debond length depends on the interfacial shear stress τ_s, interface toughness (Γ_d), and the stress on the fiber.[1,5,8] However, since x-ray tomography is based on x-ray attenuation and the attenuation of the BN coating is so low that it appears black, there is no way to discern between the fiber coating and the debond spacing and therefore the fiber/matrix debonding is not detectible using these micro-CT techniques. Also, the debond gap is so small that it would be unlikely to be resolved.

Theoretical mechanical models have been developed to relate the spacing of matrix cracks to the debond length. The Budiansky, Evans and Hutchinson model is one of the first to consider debonding mechanism. It has been suggested that debond length could correlate to matrix crack spacing and therefor the Budianksy, Evans and Hutchinson model regarding shear-lag in unidirectional CMCs was used to determine the debond length, l_d, for each sample in this study and was compared to the measured matrix crack spacing for each specimen.[5,8] The debond length was calculated using Equation (3.2a) where v_m and v_f represent the volume fraction of the matrix and fiber respectively, E_m and E_c represent the elastic modulus of the matrix and the composite, σ is the applied stress, and τ_s is the interfacial sliding stress. The debonding stress, σ_d is determined from Equation (3.2b) where r is the fiber radius, E_f is the elastic modulus of the fibers, and Γ_d is the debonding toughness.

$$\frac{l_d}{r} = \left(\frac{v_m E_m}{v_f E_c}\right)\frac{\sigma - \sigma_d}{2\tau_s} \tag{3.2a}$$

$$\sigma_d = 2v_f\sqrt{\frac{E_f E_c \Gamma_d}{v_m E_m r}} \tag{3.2b}$$

The debond length was determined for Specimen 1 and Specimen 2 at applied stresses of 550 MPa and 430 MPa respectively which were the last imaged stress increments before failure for each specimen. For Specimen 1 the debond length l_d, was determined to be 213 μm while the debond length for Specimen 2 was calculated as 137 μm respectively using the values listed in Table 3.2. The observed matrix crack spacing for both samples at these same stresses (550 MPa and 430 MPa) were 208 μm and 432 μm for Specimen 1 and Specimen 2 respectively. There seems to be a good agreement between the calculated debond length and the observed matrix crack spacing for Specimen 1 at a composite stress of 550 MPa, directly before failure. However, Specimen 2, which was the weaker of the two specimens has a much larger matrix crack spacing when compared to the calculated debond length. The calculated debond length is lower than Specimen 1 because the applied stress at which matrix cracking was initially observed in Specimen 2 was lower when compared to Specimen 1. It is most likely that the specimen failed before matrix crack saturation was obtained which resulted in a fewer number of matrix cracks and therefore a direct comparison cannot be made.

Table 3.2 Values used for variables in debond length and shear lag distance predictions

Material Property Variables	Value
E_m	360 GPa
E_f	400 GPa
E_c	371 GPa
v_m	0.28
v_f	0.72
τ_s	15 MPa
r	7.5 μm
Γ_d[20]	1.8 J/m^2

Matrix crack spacing is also often compared to the shear lag distance. Shear lag is the distance from a matrix crack plane to the point at which the fiber stress is equivalent to the linear-elastic stress that is experienced in the undamaged region and can be calculated by re-arranging Equation (3.3) to solve for shear lag distance, z, assuming $\sigma_f(z)$ to be the stress in the fiber in the undamaged region. The stress in the undamaged region was determined based on the stress at which initial matrix cracking was observed. It is known that the first matrix crack occurred at or around 470 MPa for Specimen 1 and was imaged at 375 MPa for Specimen 2. Therefore, directly before matrix cracking, the average stress in the fibers, $\sigma_f(z)$, is approximately 500 MPa and 400 MPa for Specimen 1 and Specimen 2 respectively which can be assumed to be the stress in the fibers in the undamaged region of the specimen, determined from Equation (3.1). For Specimen 1, using a constant fiber stress of 500 MPa, the shear lag distance was predicted to be 366 μm which is approximately 150 μm larger than the last measured matrix crack spacing of 210 μm but correlates well the to the matrix crack spacing that occurred in Specimen 1 at both 490 and 510 MPa. For Specimen 2, using a constant matrix stress value of 350 MPa the shear lag distance was calculated to be 282 μm compared to a final matrix crack spacing measured to be

430 μm. The shear lag distance calculated for Specimen 2 is approximately 150 μm smaller than the final matrix crack spacing. Once again, it is most likely that Specimen 2 failed before matrix crack saturation was reached. Although the shear lag distance can be calculated and compared to the measured matrix crack spacing for each specimen, it is important to note that there will be a certain point where shear lag distances will overlap from neighboring cracks and the fiber/matrix will no longer return to the far-field strain state but instead the bulk strain of the composite will increase.

$$\sigma_f(z) = \frac{\sigma}{v_f} - \frac{2\tau_s z}{r} \tag{3.3}$$

The comparison between the final measured matrix crack spacing in both specimens and the predicted debond lengths and the predicted shear lag distances are shown in Table 3.3. The measured matrix crack spacing observed using micro-CT was 200 μm and 450 μm for Specimen 1 and Specimen 2. For Specimen 1 the measured matrix crack spacing corresponded extremely well to the debond length prediction of 200 μm. Specimen 2 didn't appear to correlate well to either prediction although it most closely corresponded to the shear lag distance predictions of 300 μm.

Table 3.3 The measured matrix crack spacing for each spacing compared to the predicted debond lengths and shear lag distances for each specimen based upon material properties.

	Specimen 1	**Specimen 2**
Measured: matrix crack spacing	200 μm	450 μm
Predicted: Debond Length	200 μm	200 μm
Predicted: Shear lag distance	400 μm	300 μm

3.3.2 The different cases for predicting the onset of matrix cracking and comparing the models to observed initial matrix cracking.

Detailed observations of the evolution of matrix cracking throughout the volume of the specimen was described in Chapter 2. However, there have been many models developed to predict the stress at which the composite will first experience nonlinearity due to the onset of matrix cracking. Aveston, Cooper, and Kelley[1] (ACK) predicted the matrix cracking stress based upon the concept of steady state crack growth and energy absorption that occurs during damage within the matrix. Their model for matrix cracking stress is described by Equation (3.4) where Γ_m is the matrix fracture toughness, σ_r is the residual stress in the composite, all other variables have been previously defined and the values used for each variable is listed in Table 3.4. Although ACK initially acknowledges that debonding occurs and that energy is absorbed by this process, they later go on to state that they cannot estimate the debonding energy and that they believe that in comparison to the energy it takes to form a matrix crack, debonding energy is negligible. As a result, they don't consider it in their final model but rather focus on the interfacial sliding stress (τ_s) that is experienced between the fiber and matrix due to fiber slipping.

$$\sigma_{mc,slip} = E_c \left[\frac{6 v_f^2 E_f \tau_s \Gamma_m}{v_m E_m^2 E_c r} \right]^{\frac{1}{3}} - \sigma_r \tag{3.4}$$

The matrix cracking stress determined from Equation (3.4) is 262 MPa which is approximately 100 MPa lower than the initial matrix cracking observed in both of the unidirectional specimens which were 362 MPa for Specimen 1 and 350 MPa for Specimen 2. The matrix cracking stress for fiber slipping is heavily dependent on the interfacial sliding stress which in turn corresponds to the fiber coating thickness which is known to be non-uniform when directly comparing fiber to fiber. The interfacial sliding stress (τ_s) for these materials has been previously determined by GE Research to be in the range of 5-50 MPa with an average stress of 15 MPa, the value used to determine the matrix cracking stress. Figure 3.4 depicts how the matrix cracking stress can vary based on the value of the interfacial sliding stress parameter used in Equation (3.4). When the interfacial sliding stress is extremely low, the onset matrix cracking stress could occur below 100 MPa for these materials, while a large sliding stress could result in an initial matrix cracking stress of 350 MPa which is closer to the experimentally observed values. In summary, with a range of 5-50 MPa for τ_s, the onset of matrix cracking could vary by 300 MPa. So, although an average interfacial shear stress of 15 MPa was used to predict a matrix cracking stress of 262 MPa, if the interfacial shear stress was actually much larger than 15 MPa, then the predicted matrix cracking stress ($\sigma_{mc,slip}$) could correlate much better to the initial matrix cracking observations obtained from the synchrotron.

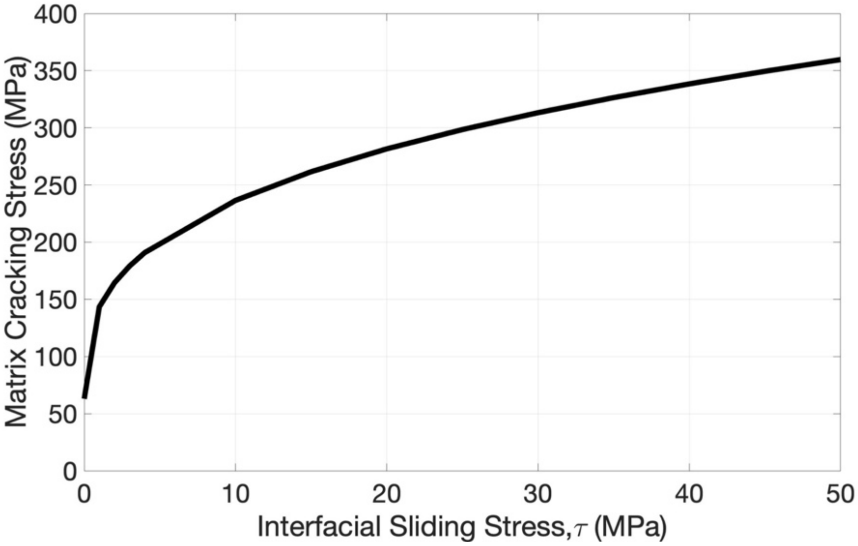

Figure 3.4 the stress at which the onset of matrix cracking occurs greatly depends on the interfacial sliding stress parameter.

Budiansky Hutchinson and Evans[2] (BHE) also developed mechanical models for the onset of matrix cracking for two separate cases (i) unbonded fibers held within the matrix by initial pressures due to thermal or other strain mismatches and are susceptible to frictional slip and (ii) fibers that were initially bonded to the matrix but debond due to the initiation of matrix cracking and results in no slipping. In the case of bonded fibers, the matrix cracking stress will depend on the debonding toughness of the composite. The no slip case is described by Equation (3.5a) and (3.5b) where υ is the Poisson's ratio.

$$\sigma_{mc,no\ slip} = BE_c \left[\frac{6v_f^2 E_f}{v_m^2 E_c(1+\upsilon)}\right]^{\frac{1}{4}} \left[\frac{\Gamma_m}{rE_m}\right]^{\frac{1}{2}} \tag{3.5a}$$

$$B = \left[\frac{2v_m^3}{-6\ln(v_f) - 3v_m(3-v_f)}\right]^{\frac{1}{4}} \tag{3.5b}$$

The matrix cracking stress determined from Equations (3.5a) and (3.5b) was calculated to be 659 MPa which is much larger than what was observed in these specimens by 297 MPa and 309 MPa for Specimen 1 and Specimen 2 respectively. In fact, the calculated stress for $\sigma_{mc,no\ slip}$ is higher than the stress at which both specimens experienced failure. Based on fiber pullout and fiber break opening that was observed in these specimens, it is known that fiber slipping does occur and therefore the onset of matrix cracking based on no fiber slipping does not relate to these materials.

The onset of matrix cracking for composites with initially bonded fibers that experience debonding in the matrix crack wake is described by Equation (3.6) where l_d is the debond length previously described in Equation (3.2a) and B is determined from Equation (3.5b).

$$\sigma_{mc,debond} = \sigma_{mc,no\ slip}\left[\frac{1+\frac{4v_f l_d \Gamma_d}{v_m r \Gamma_m}}{1+\frac{B^2}{v_m}\left[\frac{6E_c}{(1+v_m)E_f}\right]^{\frac{1}{2}}\left(\frac{l_d}{r}\right)}\right]^{\frac{1}{2}} - \sigma_r \tag{3.6}$$

Taking into consideration, fiber/matrix debonding mechanisms results in a matrix cracking stress of 286 MPa from Equation (3.6). This is slightly larger than the matrix cracking stress described by ACK. The initial matrix crack was detected in Specimen 1 at an applied stress of 362 MPa while the initial matrix crack in Specimen 2 was detected at 350. Both of the observed matrix cracking occurred at stresses between 65-75 MPa greater than what Equation (3.6) predicted. However, the matrix cracking stress case that considers debonding is within a reasonable range of comparison to the observed values from the micro-CT imaging. Table 3.5 lists all of the calculated values from Equations (3.4)-(3.6) and compares them to the stress at which matrix cracking was first detected in both of the specimens.

Table 3.4 Values used for variables in the onset of matrix cracking predictions

Material Property Variables	**Value**
E_m	360 GPa
E_f	400 GPa
E_c	371 GPa
v_m	0.28
v_f	0.72
τ_s	15 MPa
r	7.5 μm
Γ_d[20]	1.8 J/m^2
Γ_m	36 J/m^2
υ	0.14
σ_r	63 MPa

Table 3.5 The stress at which the onset of matrix cracking occurred spacing for each compared to the mechanical models developed for the onset of matrix cracking for various cases based on the microstructure and its results mechanical behavior.

Onset of Matrix Cracking	Value
Slip ($\sigma_{mc,slip}$)	262 MPa
No Slip ($\sigma_{mc,no\ slip}$)	659 MPa
Debonding ($\sigma_{mc,debond}$)	286 MPa
Initial matrix cracking observed in Specimen 1	362 MPa
Initial matrix cracking observed in Specimen 2	350 MPa

3.3.3 Fiber Fragmentations

After matrix cracking occurs, the matrix crack no longer has the ability to sustain applied stress at the location of the matrix crack resulting in the stress experienced by the fibers to be at a maximum at the matrix crack plane. The stress maintained by the fibers decreases linearly as a function of distance away from the matrix crack. Commercially available Hi-Nicalon Type S fibers have a fiber strength of 2.6-3 GPa and a fiber failure strain of ~0.7%.[15-17,40] Composite failure is completely dependent on fiber failure and ceramic fiber strengths are highly stochastic. There have been studies done on the testing of these fibers and resulting Weibull moduli of 2.5-4.5 have been reported.[34,41] The increase in stress on the fibers results in fibers breaking near a matrix crack. Conventional imaging of polished CMC sections often does not show in-situ fiber fractures and the fiber damage that it does capture could be due to polishing artifacts instead of the actual mechanics of the composite. Because of this, there is limited experimental information related to both the number and location of failed fibers within a melt infiltrated SiC/SiC composite. Figure 3.5, a single 2D slice within the volume of Specimen, readily demonstrates that micro-CT can be used to observe fiber breaks. It can be seen in Figure 3.5 that the gap, or fiber break height, can vary between each individual fiber and a single fiber can be broken in more than one location.

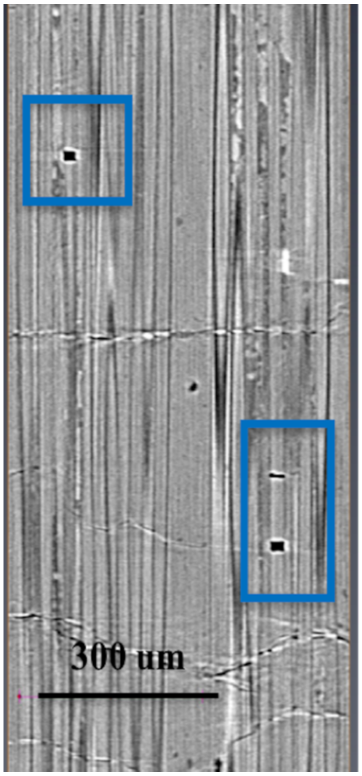

Figure 3.5 Fiber Breaks detected within the volume of Specimen 1 observed from sagittal view at 550 MPa (Slice 458 out of 2559). It can be seen that the height of each fiber break varies and that a single fiber can break twice.

Individual fiber breaks were observed within the volume of each specimen as a function of applied stress. Figure 3.6a represents the 3D location of approximately 300 fiber breaks measured within the volume of Specimen 1 at an applied stress of 445 MPa while Figure 3.6b represents that same 3D scanned field of view for Specimen 1 but at a stress of 550 MPa where there were approximately 2,300 fiber breaks measured. Figures 3.7a and 3.7b show the number of fiber breaks and their location in Specimen 2 at 375 MPa and 430 MPa respectively. At 375 MPa there were a little over 300 breaks detected within the volume of Specimen 2 while there were almost 1,600 breaks detected at 430 MPa which was the stress increment that was imaged directly before Specimen 2 failed.

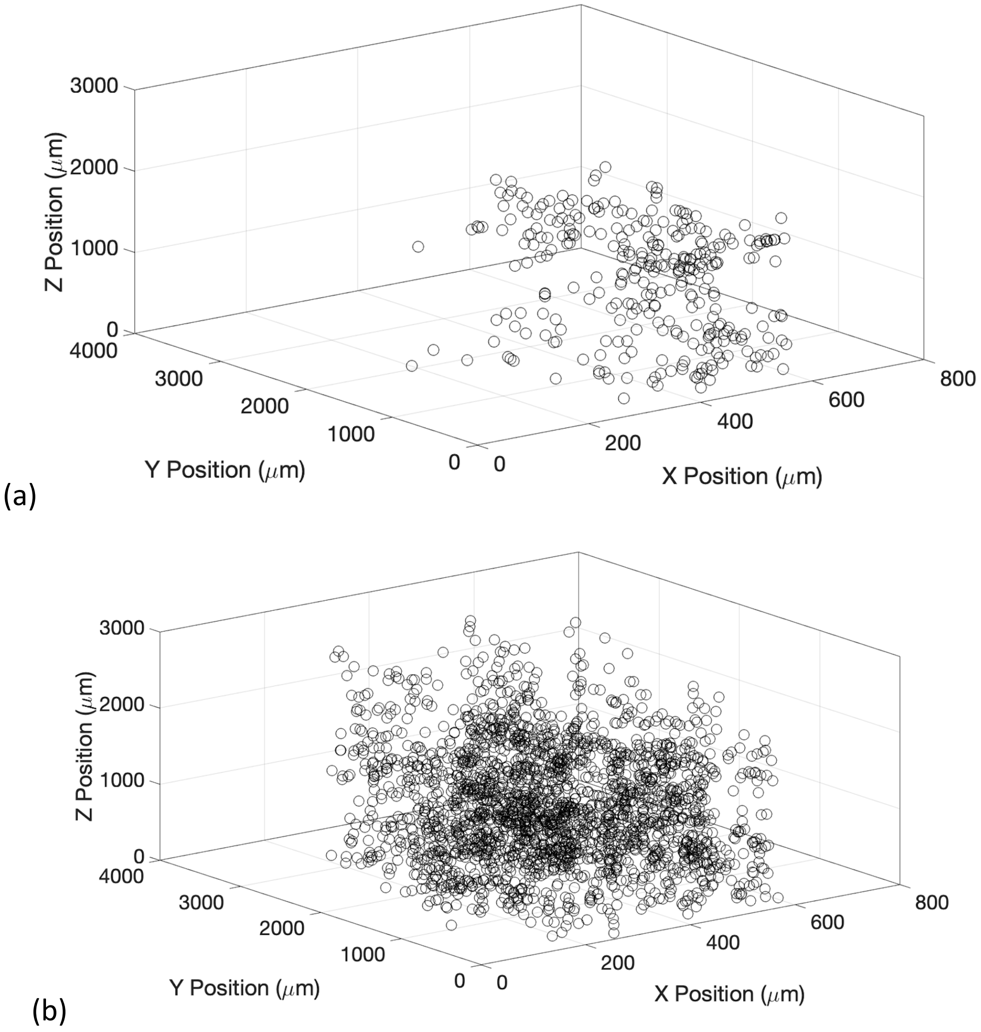

Figure 3.6 (a) the 3D location of approximately 300 breaks measured within the volume of Specimen 1 at 445 MPa (b) the 3D location of approximately 2300 breaks measured within the volume of Specimen 1 at 550 MPa

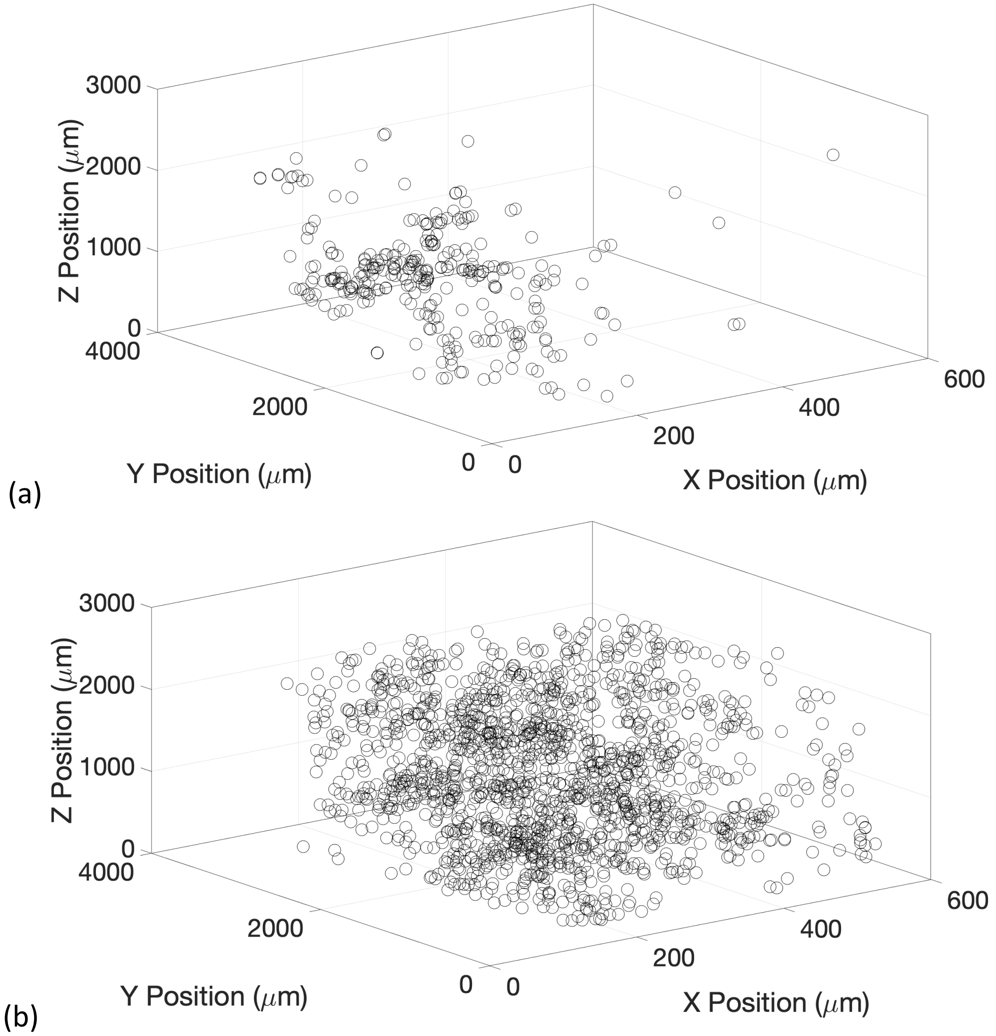

Figure 3.7 (a) the 3D location of approximately 300 breaks measured within the volume of Specimen 2 at 375 MPa (b) the 3D location of approximately 1600 breaks measured within the volume of Specimen 2 at 430 MPa

The total number of fiber fragmentations observed within the volume of each specimen is plotted in Figure 3.8 as a function of % of failure stress for each specimen. When comparing the number of fiber breaks in each specimen as a function of % of total failure stress, it can be seen that there is good agreement. Between 70-80% of both specimens failure stress, there were less than 500 detected fiber breaks. The number of fiber fragmentations increased drastically increased between 85% and 100% of both Specimen 1 and Specimen 2’s failure stress. There were approximately 3,000 fiber breaks measured post fracture in both specimens, at 100% of their failure stress. There appears to be a linear trend in the number of fiber breaks as the applied stress, or % of failure stress, increases.

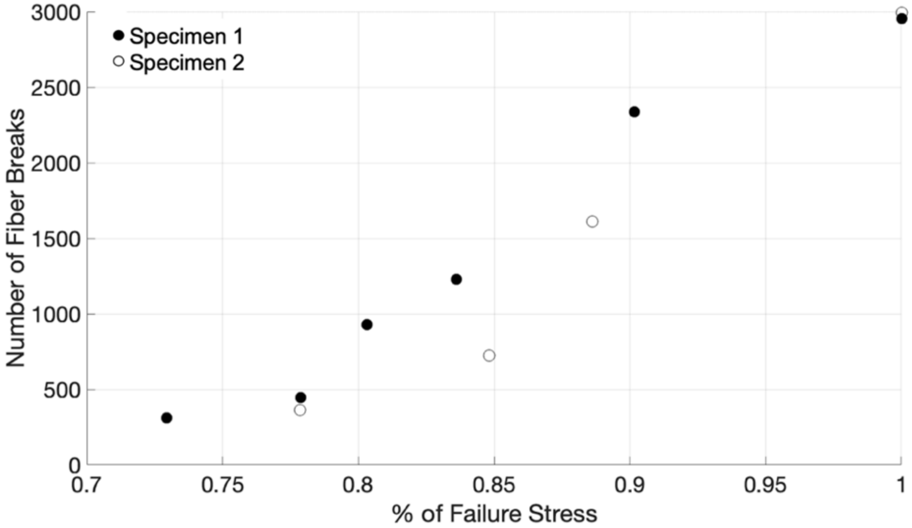

Figure 3.8 total number of fiber fragmentations measured at increasing scanned stress increments shown as the % of each specimen’s failure stress

Using the number of segmented fibers compared to the volume fraction of fibers in this sample, the approximate % of intact fibers can be projected as shown in Figure 3.9. However, the micro-Ct imaging only captured a portion of the gauge section so there are fibers that failed outside of the field of view that were not taken into account. At lower stresses of 445 and 475 MPa, ~70-80% of Specimen 1’s failure stress, over 80% of the fibers were still intact, assuming the number of fibers who had fragmentations in multiple locations was minimal. There were approximately 2300 fiber breaks at 90% of Specimen 1’s failure stress shown in Figure 3.8, so only 33% of the fibers were still intact. At fracture for both specimens, fiber fragmentations that were detected away from the fracture plane were measured and it was determined that there were approximately 3000 fiber breaks measured which would assume almost all of the fiber had broken and the ones that didn't were no longer able to carry load.

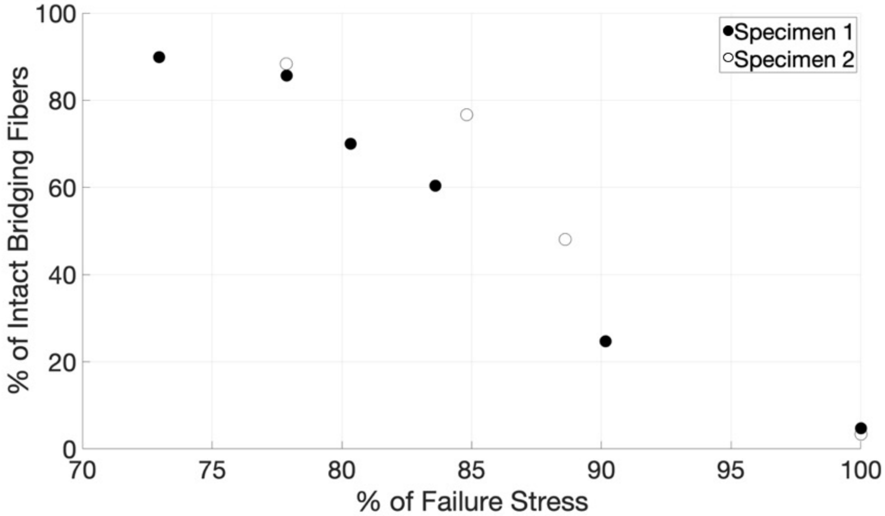

Figure 3.9 The percentage of fibers that are considered "intact" and bridging the plane of matrix crack assuming that a fiber only breaks once at each stress increment shown as the % of each specimen's failure stress.

3.3.4 Correlating Observed Matrix Cracks and Fiber Fragmentations

Previous work has been done on studying either matrix cracking or fiber fragmentation, but very little experimental work has been done to compare and correlate the two types of damage mechanisms. In Figure 3.10a and 3.10b, the 2-dimensional locations of all the fiber breaks and matrix cracks, relative to a common reference zero, measured in Specimen 1 at 445 and 550 MPa are shown in order to qualitatively compare the location of each type of damage. The black lines represent the average location of each measured matrix crack at the respective stress increment while the open black circles represent the 2-dimensional locations of fiber breaks in the coronal plane. Several fiber fragmentations were detected near the uppermost region of Specimen 1 in Figure 3.10b that don't appear to correspond to a nearby matrix crack. However, one must recall that the field of view for imaging is 2.8 mm x 3.3mm (height x width) while the actual gauge section of the specimen is 9.0 mm x 3.0 mm (height x width) and therefore fiber fragmentations that were identified near the upper portion of Figure 3.10b, correlate to matrix cracks that are not visible in the scanned field of view but rather to a matrix crack outside of the field of view confirmed by post-test micro-CT imaging.

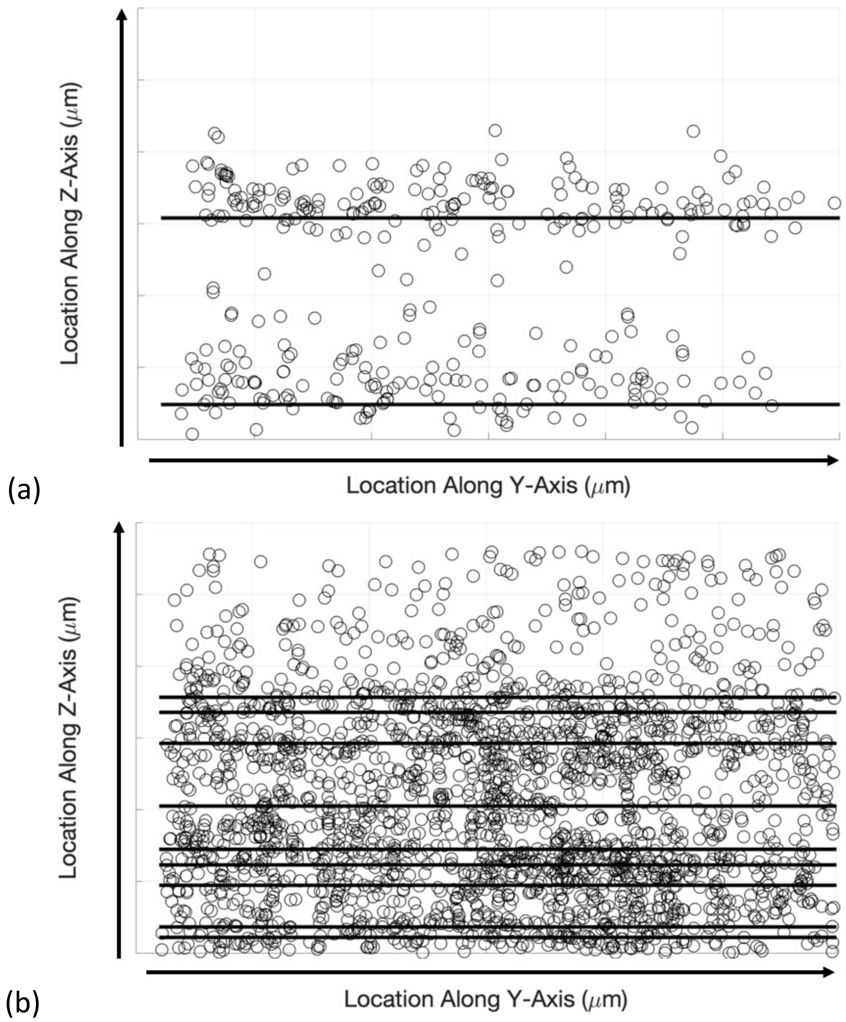

Figure 3.10 (a) the position of fiber breaks (open circles) and matrix cracks (black lines) within the field of view of Specimen 1 at 445 MPa (b) the position of fiber breaks (open circles) and matrix cracks (black lines) within the field of view of Specimen 1 at 550 MPa

The same qualitative analysis was done for Specimen 2 as shown in Figures 3.11a and 3.11b at applied stresses of 375 MPa and 430 MPa respectively. The fiber fragmentations that were initally imaged in Specimen 2 at 375 MPa were measured after five equally spaced matrix cracks were detected within the volume of the specimen. These equally spaced matrix cracks caused the fiber fragmentations to occur more uniformly throughout the imaged volume when compared to Figure 3.10a within Specimen 1 where the fiber fragmentations distinctly occurred in close proximity to each matrix crack.

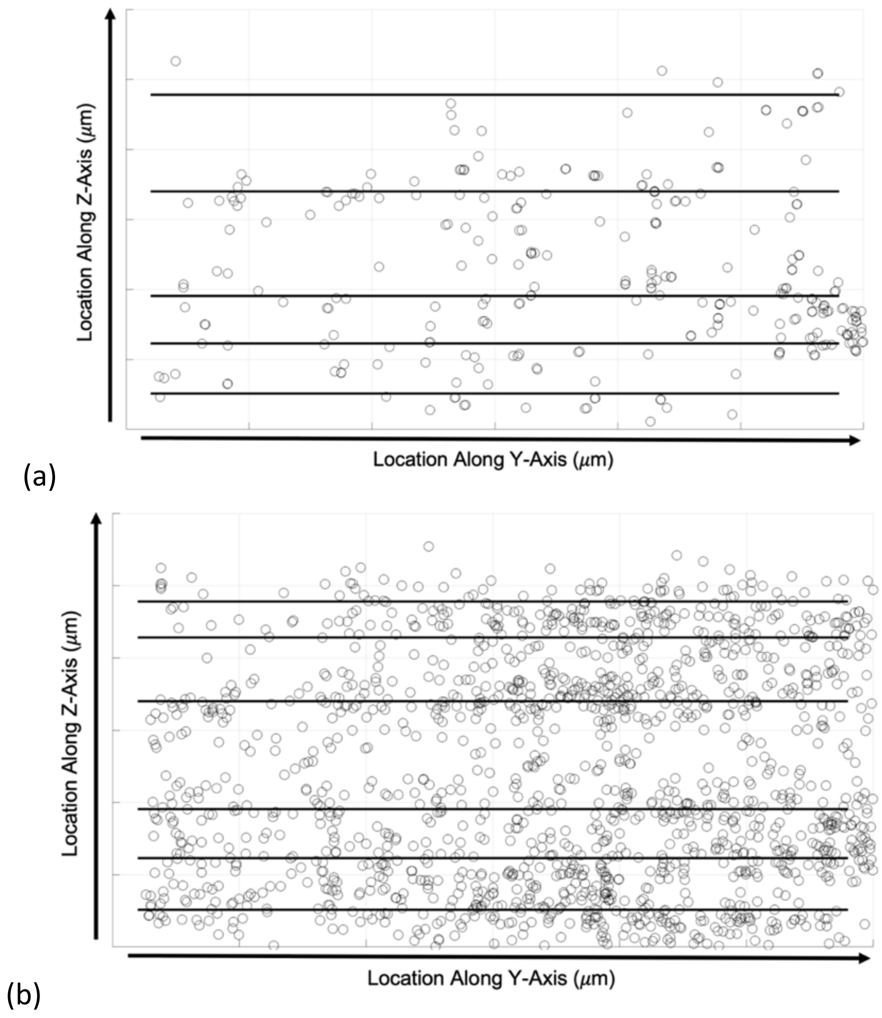

Figure 3.11 (a) the position of fiber breaks (open circles) and matrix cracks (black lines) within the field of view of Specimen 2 at 375 MPa (b) the position of fiber breaks (open circles) and matrix cracks (black lines) within the field of view of Specimen 2 at 430 MPa

Another way to look at the comparison between the location of fiber breaks and the location of matrix cracks is to quantify damage along the length (or z-axis) of the specimen as depicted in Figure 3.12a. The number of fiber fragmentations were quantified by counting the number of breaks detected within 100 μm increments along the length (height) of the specimen. The number fragmentations measured within each 100 μm region at each stress increment for Specimen 1 is shown in Figures 3.21b-f. The average location of each matrix crack (depicted by the dashed vertical lines) was also included in these figures in order to compare the fiber fragmentation trends to the location of each matrix crack. At 445 MPa, (Figure 3.12b) most of the fiber fragmentations were detected at 200 μm and 1500 μm along Specimen 1's length which matrix positions. There was a slight inrease in the number of fiber breaks observed at 475 MPa (Figure 3.12c) when compared to 445 MPa but no region exhibited a significant amount of increased damage. At 490 MPa (Figure 3.12d), there was a substantial increase in the number of fiber breaks at the locations where fiber fragmentations were first detected. For example, the number of fiber breaks increased from approximately 70 measured breaks at the 1500 μm location to 110 breaks. Also in that area two additional matrix cracks were observed along with an increase in the number of fiber breaks surrounding the area next to the matrix crack. The two areas along the specimen's length where large amounts of damage were detected were labelled "Damage Zone A" and "Damage Zone B" as shown in Figure 3.12d. By 510 MPa (Figure 3.12e) the damage observed within Damage Zone A and Damage Zone B continued to increase. A slight increase in the number of fiber fragmentations was mesaured near the 700 μm location along the length of the specimen, although the number of fiber breaks in this region was minimal compared to the two main damage zones. At the final imaged stress increment before failure at 550 MPa (Figure 3.12f), the number of fiber breaks measured at this stress increment is depicted by the red curve and the red vertical line represents the new matrix crack the caused failure. Four new matrix cracks, including the one that caused failure, were detected at the last imaged stress increment and all appeared in an initally “undamaged” zone between Damage Zones A and B. Also the number of fiber breaks drastically spiked in the area near the failure crack going from less than 30 detected fiber fragmentations at the previous stress increment to almost 160 fiber fragmentations at 550 MPa. The maximum number of fiber fragmentations measured directly before failure was within 200 μm of the crack that caused failure. It is possible that the load from the two inital “damage” zones were both being shed on to this undamaged zone until evenutally significant damage occurred to relieve the stress.

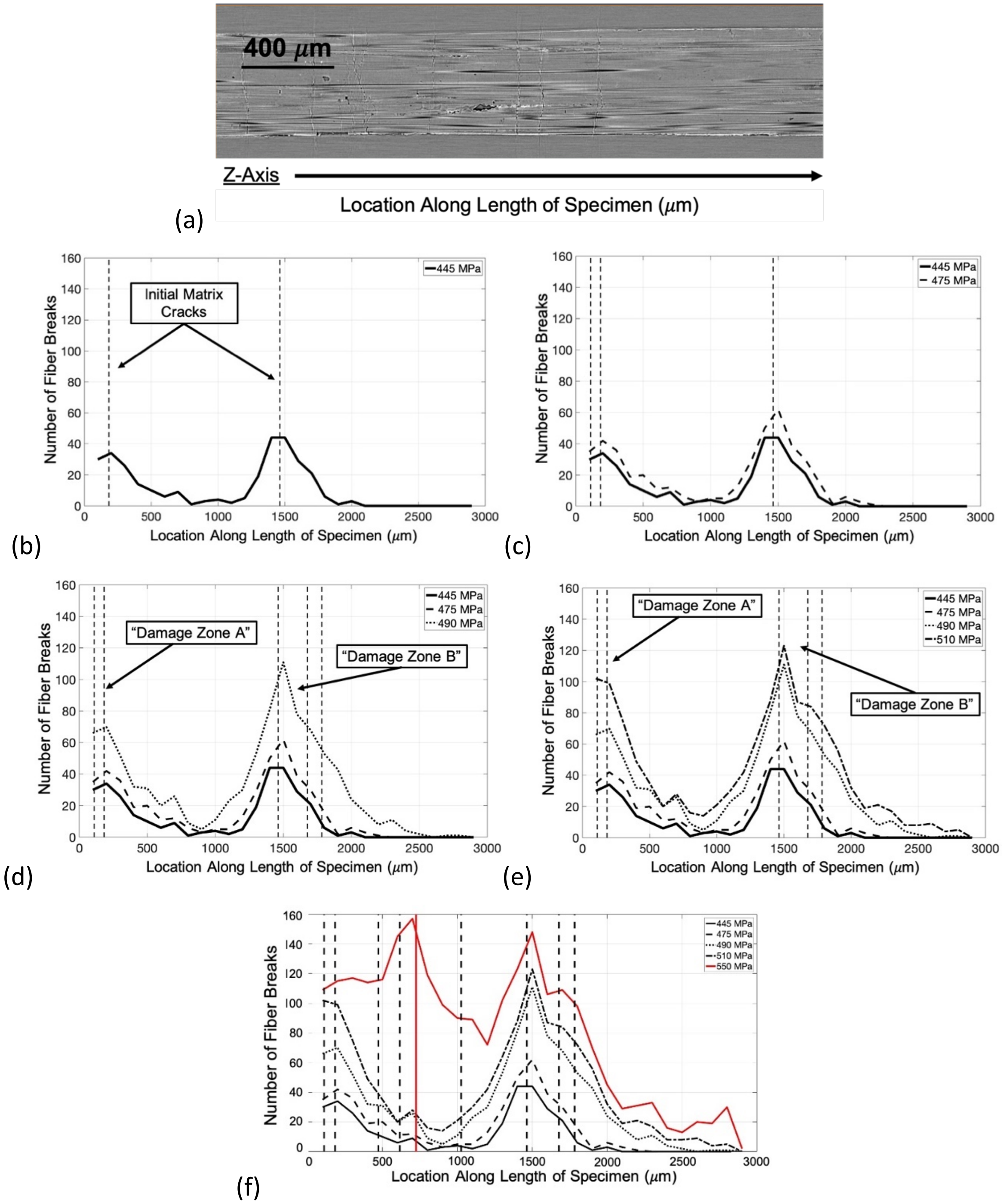

Figure 3.12 (a) depicts the length of the specimens in which the number of fiber breaks were measured. (b-f) the number of fiber breaks that occurred within 100 *μm* increments along the length of Specimen 1 for each increasing stress increment of (b) 445 MPa (c) 445 MPa and 475 MPa (d) 445 MPa, 475 MPa and 490 MPa (e) 445 MPa, 475 MPa, 490 MPa, and 510 MPa (f) 445 MPa, 475 MPa, 490 MPa, 510 MPa, and 550 MPa (directly before failure)

Specimen 2 failed in a much different way than Specimen 1 which was shown in Chapter 2 and can be seen when quantifying the damage as well. Specimen 2 did not have a clean fracture surface so in order to try to compare the damage between the two specimens, it was assumed that location of the failure crack in Specimen 2 was where the clean fracture began as depicted in Figure 3.13a. Unlike Specimen 1, the matrix crack that led to failure in Specimen 2 was first seen at an applied stress of 375 MPa which was the first stress increment at which fiber fragmentations were also observed. The matrix crack spacing in Specimen 2 is much more uniform at lower applied stresses than what was observed in Specimen 1 where the matrix cracks appeared to agglomerate near one another. In Figure 3.13b, there were four matrix cracks in the field of view and the locations where an incrase in the number of fiber fragmentations were measured all occur near observed matrix cracks. The matrix crack that eventually led to failure was detected at approximately 1000 μm along the speicmen's length and the number of fiber breaks near this crack did continue to grow although it didn't appear to have a distinctly different trend than the other nearby areas of damage. In Figure 3.13d the red curve depicts the number of fiber breaks observed directly before failure where it can be seen that the number of fiber breaks around each matrix crack is approximately the same with between 90 and 100 fiber breaks occuring near each matrix crack. The lower number of expected fiber fragmentations is also due to the non-planar fracture surface. It was assumed that one distinct matrix crack caused failure (as shown in Figure 3.13a) but it is known that this is not true and as a result there are fewer fragmentations and most of the fragmentations that were detected are in correlation to the section of the matrix crack that had a clean linear fracture surface.

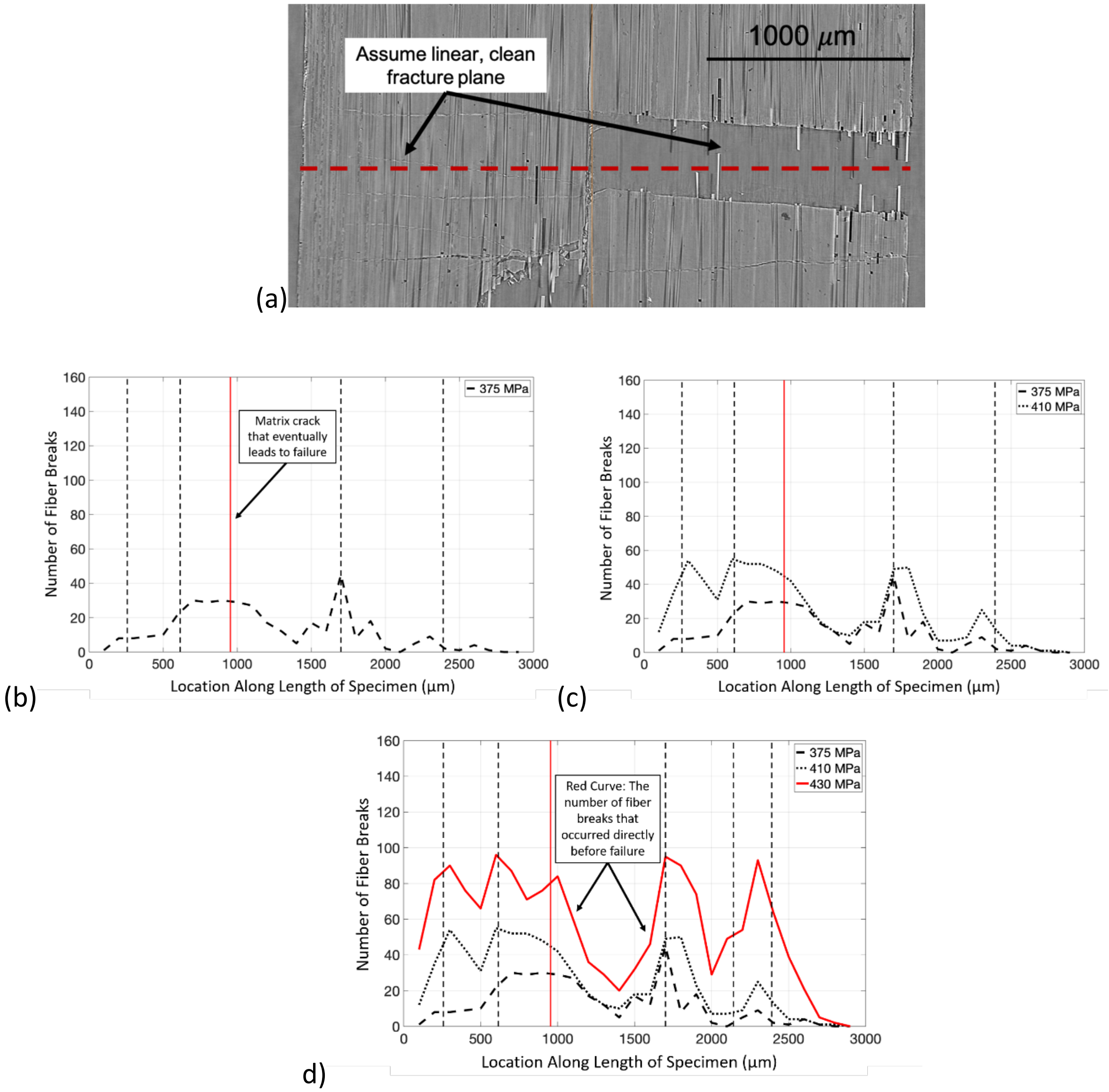

Figure 3.13 (a) Specimen 2 did not exhibit a typical fracture when it failed however in order to compare the number of fiber breaks near the location of the "failure crack", it was assumed that the initial clean, linear fracture plane extended across the entire width of the specimen even though it did not. (b-c) the number of fiber breaks that occurred within 100 μm increments along the length of Specimen for each increasing stress increment of (b) 375 MPa (c) 375 MPa and 410 MPa (d) 375 MPa, 410 MPa, and 430 MPa (directly before failure)

3.3.5 Comparing fiber fragmentation locations (distance away from a matrix crack) to mechanical predictions

It was qualitatively observed that fiber fragmentations often occur near matrix cracks as seen in Figures 3.10-3.13. The correlation between fiber fragmentations and matrix cracking was measured by binning fiber breaks to a specific matrix crack based on the fiber break's centroid. A schematic of this process is depicted in Figure 3.14 where there are three matrix cracks in the field of view portrayed by the three different colored dashed lines. Every fiber break that occurred between a certain matrix crack and the location half-way between another matrix crack was binned to first matrix crack. In Figure 3.14 the fiber breaks that occurred in box (1), the green box, were considered to correspond to the matrix crack in box (1) and the fiber breaks that occurred in box (2) were considered to correspond to the matrix crack in box (2), etc.

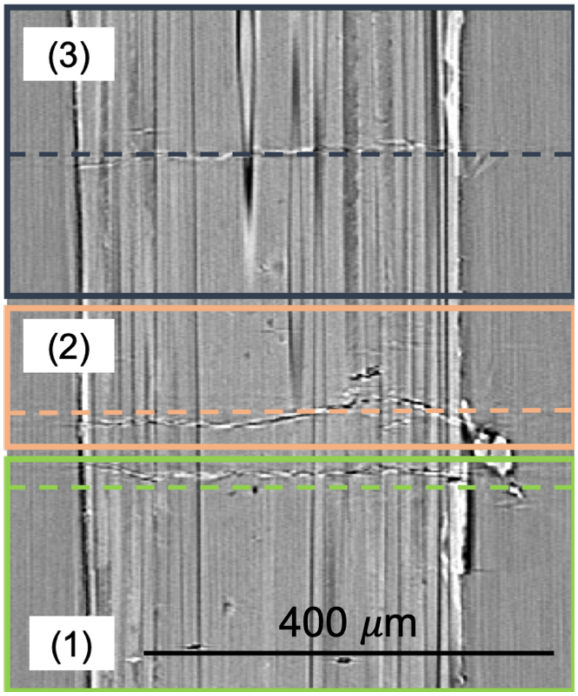

Figure 3.14 depicts how fiber fragmentations were binned for each specimen based on their location to correspond to a specific matrix crack.

The average distance at which fiber fragmentations were detected from a matrix crack is shown in Figure 3.15a and 3.15b with standard deviations. The different colors represent the different matrix cracks, arbitrarily labelled Crack A – I for Specimen 1 and Crack A – F for Specimen 2. It can be observed from Figure 3.15a that the average distance can vary depending on the crack with the average ranging from approximately 25 μm to 250 μm. The standard deviation is also quite large for the fiber fragmentations detected at lower stresses. By 550 MPa, the average fiber fragmentation distance from its respective matrix crack was within the range of 50-100 μm with the exception of the fragmentations correlated to matrix crack D. The average distance of fiber fragmentations in relation to Crack D was much larger (325 μm) in comparison to the distances of the other fiber fragmentations.

In comparison to the first specimen, Specimen 2 showed less of a distribution of fiber fragmentation distances which resulted in smaller deviations. There was also less of a range in relation to the average distance of fiber fragmentations related to each matrix crack. The average distance for detected fiber fragmentations in relation to their corresponding matrix crack ranged between 75 μm and 150 μm. The average distance of fiber fragmentations did decrease slightly at 550 MPa, directly before failure, which is expected due to the larger number of fiber breaks that occur closer to the matrix crack as damage accumulates.

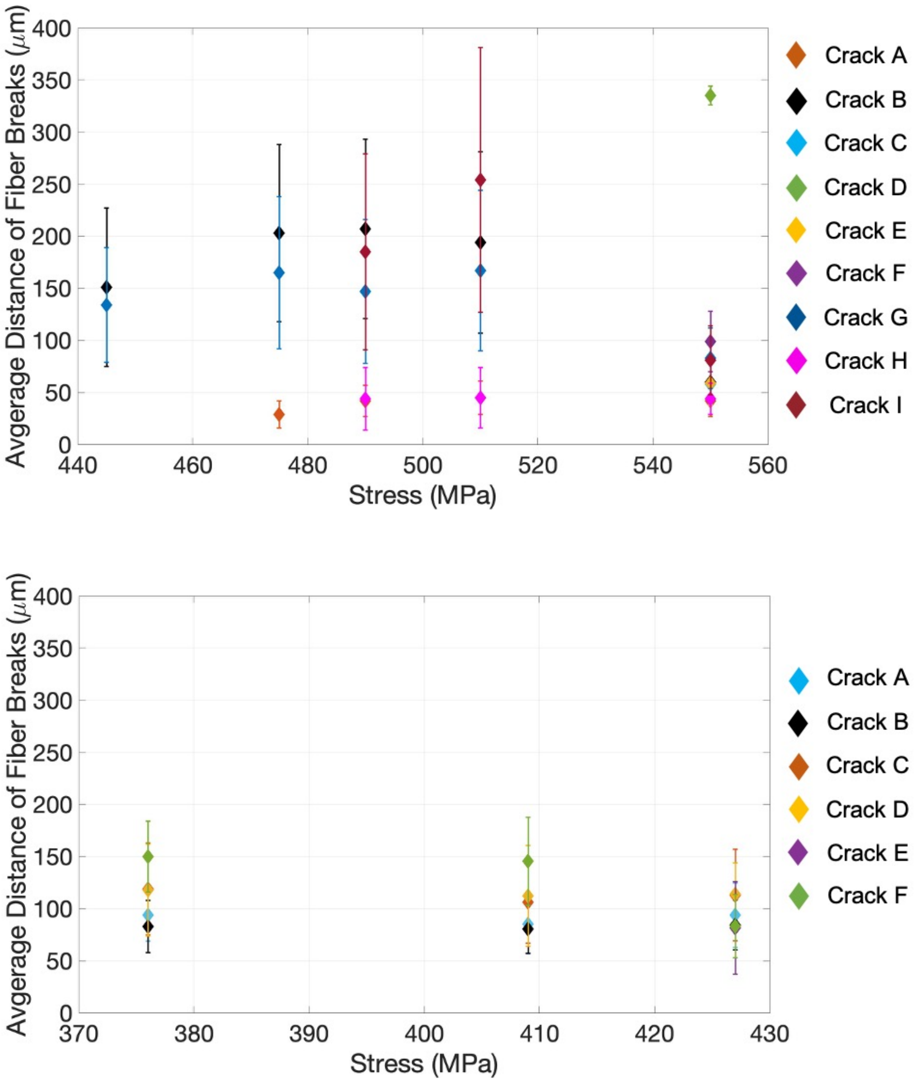

(a)

(b)

Figure 3.15 The average distance of fiber fragmentations from their corresponding matrix cracks in Specimen 1, Crack A through Crack I (b) the average distance of fiber fragmentations from their corresponding matrix cracks in Specimen 2, Crack A through Crack F

Fiber failure was studied by Thouless and Evans[11] where they studied the statistical considerations of fiber failure and incorporated fiber pull-out effects into the mechanics of these composites. In their work, the fibers were assumed to have low debond resistance so that fiber slipping would occur at a constant shear sliding resistance, τ_s. Using weakest-link statistics they were able to predict the average failure location of the fibers when all the fibers have failed (i.e.

pullout length) as shown in Equations (3.7a) and (3.7b). Since weakest link statistics were the basis of this equation S_o represents characteristic fiber strength, m represents the Weibull parameter, A is the surface area of fibers and Γ is the complete gamma function.

$$\bar{h} = \frac{A_o}{4\pi r}\left(\frac{S_o}{\Sigma}\right)^m \Gamma\left(\frac{m+2}{m+1}\right) \tag{3.7a}$$

$$\Sigma = \left[\frac{A_0 S_0^m \tau(m+1)}{2\pi r^2}\right]^{\frac{1}{(m+1)}} \tag{3.7b}$$

Using Equations (3.7a) and (3.7b) results in an average pullout length of 215 μm, at final fracture. When comparing this predicted distance to the average distances of fiber fragmentations to their relative matrix crack in Specimen 1 (Figure 3.15a) this correlates relatively well to the values at some of the lower stresses below 550 MPa. However, at the highest imaged stress directly before failure the average distance for most fiber fragmentations was less than 100 μm (with the exception of the breaks binned to Crack D). This is mainly dominated because of the matrix crack spacing which as discussed previously was 210 μm. If the distance from one matrix crack to another is approximately 200 μm then the maximum a distance a fiber break could occur away from its corresponding matrix crack plane is 200 μm. The distance of fiber fragmentations for Specimen 2 were all closer to the matrix crack than the calculated 215 μm, with the largest average distance being 150 μm.

As shown earlier, there were up to 3000 fiber breaks detected at failure for each specimen and as the standard deviations show in Figure 3.15a and 3.15b, the fiber fragmentations occurred at a range of distances from the matrix crack plane. Therefore it is more beneficial to look at the distribution of fiber break distances instead of just the averages when comparing them to the calculated average failure location from Equations (3.7a) and (3.7b)

Using the same binning method used to determine the average fiber fragmentation distance, Figures 3.16a-e show the distribution of fiber fragmentation distances from the location of their corresponding matrix crack plane at each stress increment. Figure 3.16a shows that at 445 MPa, 80% of the fiber fragmentations related to Crack B and Crack G (arbitrarily labelled) occurred within 200 μm of each crack; although fiber fragmentations were detected up to 700 μm away from the matrix crack. At 490 MPa (Figure 3.16c), all of the fiber breaks related to Crack A and Crack H occurred within 150 μm of the matrix crack while 80% of the fiber breaks related to Crack B were detected within 400 μm of the matrix crack, while approximately 80% of the fiber breaks related to Crack G and Crack I occurred within 300 μm of the fiber breaks. There were fiber breaks located at distances over 600 μm away from the matrix crack for matrix crack's B,G and I. The location of fiber breaks at 510 MPa (Figure 3.16d) is comparable to the locations at 490 MPa (Figure 3.15c) except the number of fiber breaks that were detected at distances far away from the matrix crack (+400 μm) increased. By 550 MPa (Figure 3.16e), all of the fiber breaks were located within 200 μm of their correlated matrix crack as shown in Figure 3.15e for Cracks A-I. The distance range correlates to Specimen 1's matrix crack spacing of 210 μm. Most models predict fiber fragmentations occur near a matrix crack as the stress experienced by the fibers at the matrix crack planes would be at a maximum. However, it can be seen from Figures 3.16a-e that fiber fragmentations were detected as far as 900 μm away from the closest matrix crack. These large distances may be due to the presence of matrix cracks smaller than the resolution limits or matrix cracks just beyond the field of view.

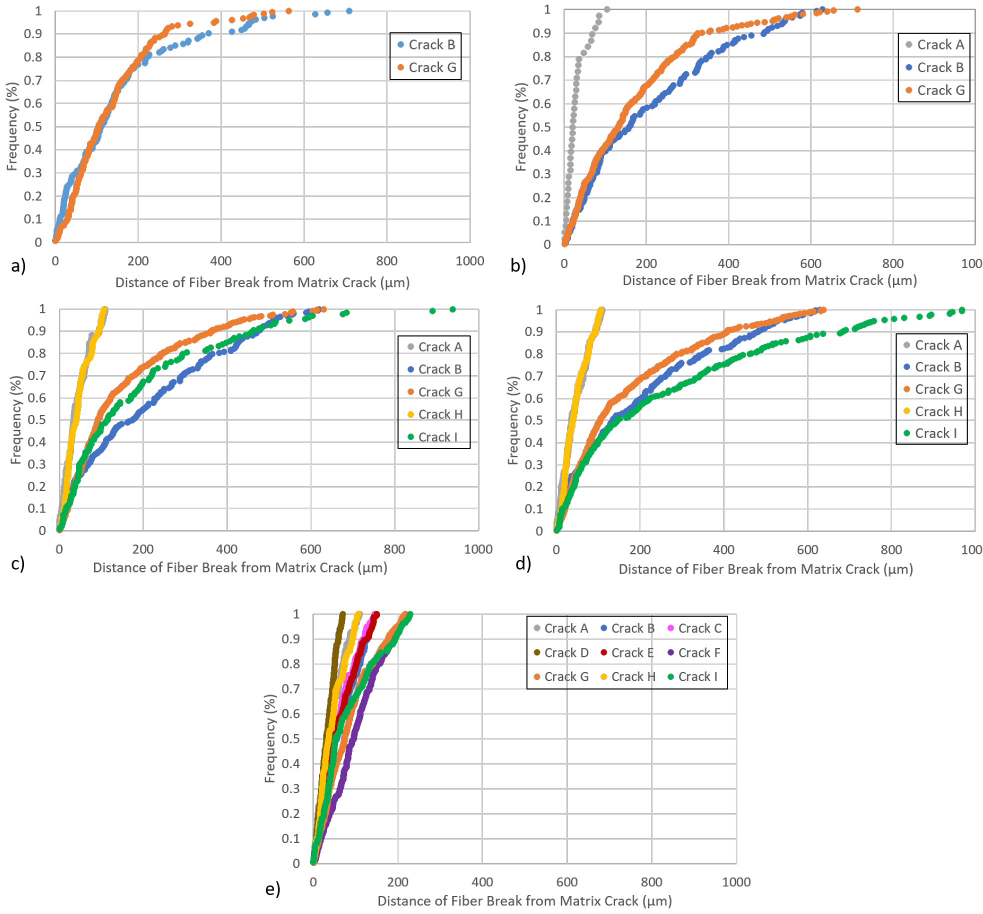

Figure 3.16 represents the percentage of fiber breaks that are located a certain distance from a specific matrix crack (cracks labelled A-I) for Specimen 1 at each stress increment of: (a) 445 MPa, (b) 475 MPa, (c) 490 MPa, (d) 510 MPa, (e) 550 MPa

For Specimen 2, the total number of fiber fragmentations detected at the specimen's lesser applied stresses was much lower than the total number of fiber fragmentations detected in Specimen 1. Also due to the uniform matrix cracking that was observed in Specimen 2, the location of measured fiber fragmentations in relation to observed matrix cracks didn't show a great deal of variation between the stress increment. In Figures 3.17a-c, all of the detected fiber fragmentation positions occurred within 400 μm of their corresponding matrix crack. By the highest imaged stress increment of 430 MPa (Figure 3.17c) 80% of the measured fiber fragmentations occurred within 200 μm of the matrix crack which is similar to what was seen in Specimen 1. The results of fiber fragmentation locations are similar to published fiber pullout studies which showed fiber pullout values between 100-250 μm.[22] The fiber fragmentation locations for Specimen 1 and Specimen 2 often fall in the range of the matrix crack spacing.

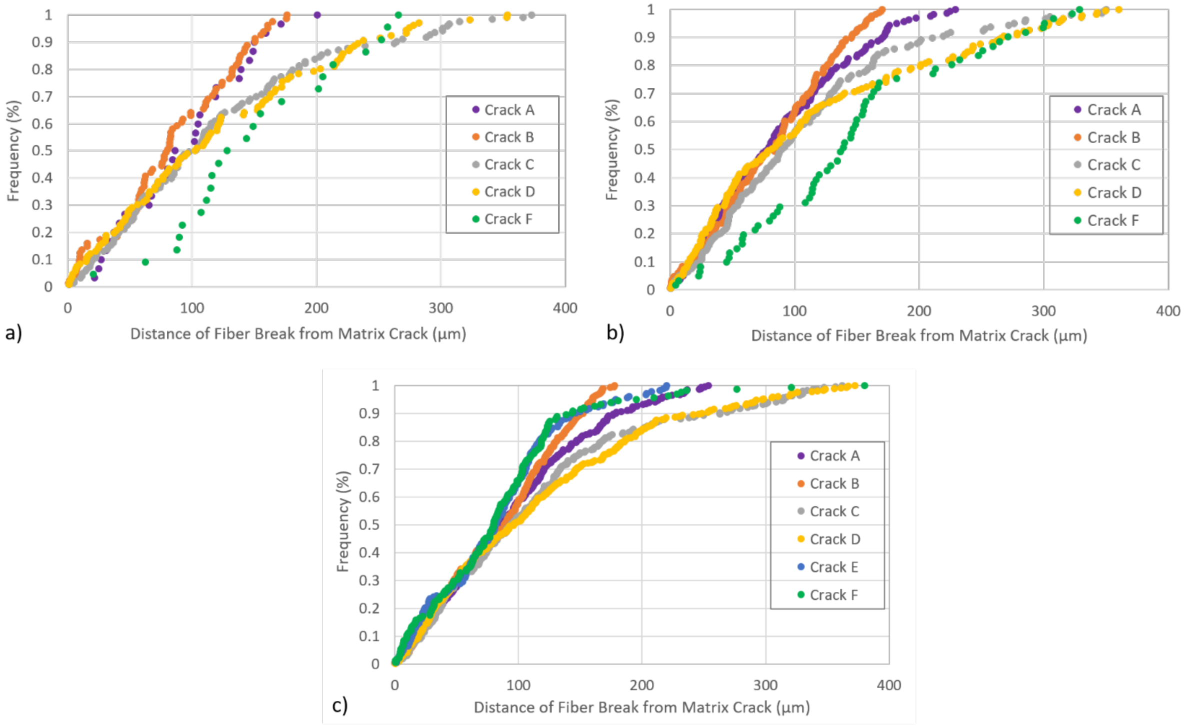

Figure 3.17 represents the percentage of fiber breaks that are located a certain distance from a specific matrix crack (cracks labelled A-F) for Specimen 2 at each stress increment of: (a) 375 MPa, (b) 410 MPa, (c) 430 MPa

3.4 Summary

Microstructural features such as matrix cracking and fiber breaks were observed using in-situ computed x-ray tomography techniques. The location of matrix cracks was measured through the volume of each specimen which allowed for determination of matrix crack spacing and matrix crack density. The observed crack spacing in each specimen was compared to the calculated values of debond length and shear lag distance determined from previous models and the predicted debond length corresponded well to the matrix crack spacing observed in Specimen 1. In-situ fiber breaks were observed and measured with the number of breaks increasing with applied stress showing nearly the same trend between both specimens. Knowing the total number of fiber breaks that occurred within the field of view allowed for an approximate measurement of the number of fibers that were still intact and bridging the matrix crack.

The number and location of fiber fragmentations were both qualitatively and quantitatively correlated to the location of the observed matrix cracks. Also, both of the specimens failed in the field of view and the matrix crack that caused failure was able to be identified. Looking at these correlations for both specimens showed that Specimen 1 and Specimen 2 had very different damage evolution modes. The damage that eventually caused Specimen 1 to fail occurred rapidly and in an area that showed no signs of previous damage until directly before failure. Specimen 2 was weaker than Specimen 1 and showed a more uniform damage evolution through the volume of the specimen. The location of fiber fragmentations in relation to their corresponding matrix crack for each specimen showed that the location of fiber fragmentation often correlates to the matrix crack spacing of the specimen. It has been predicted that fiber fragmentations should occur near an already evolved matrix crack, however fiber fragmentations up to 700 μm away from the nearest matrix crack were observed for these specimens. Using micro-CT to observe damage evolution in unidirectional SiC/SiC CMC specimens provided insight how on the two types of damage (matrix cracking and fiber fragmentations) interacted with one another.

References

1. Aveston J, Kelly A. Theory of multiple fracture of fibrous composites. J Mater Sci. 1973; 8:352-362.
2. Marshall DB, Cox BN, Evans AG. The mechanics of matrix cracking in brittle-matrix fiber composites. Acta Metall. 1985; 33(11):2013-2021.
3. Beyerle D, Spearing S, Zok F, Evans A, Damage and Failure in Unidirectional Ceramic-Matrix Composites. J Am Ceram Soc. 1992; 75(10):19-25.
4. Zok F, Spearing S. Matrix crack spacing in brittle matrix composites. Acta Metall Mater. 1992; 40:2033–2043.
5. Budiansky B, Hutchinson JW, Evans AG. Matrix fracture in fiber-reinforced ceramics. J Mech Phys Solids. 1986; 34(2):167-189.
6. Rajan VP, Zok FW. Matrix cracking of fiber-reinforced ceramic composites in shear. J Mech Phys Solids. 2014; 73:3-21.
7. W.A. Curtin, B.K. Ahn, N. Takeda, Modeling brittle and tough stress–strain behavior in unidirectional ceramic matrix composites, Acta Mater. 46 (10) (1998) 3409–3420
8. Budiansky B, Evans AG, Hutchinson JW. Fiber-matrix debonding effects on cracking in aligned fiber ceramic composites. Int J Solids Struct. 1995; 32(3-4):315-328

9. Domergue J-, Vagaggini E, Evans AG. Relationships between Hysteresis Measurements and the Constituent Properties of Ceramic Matrix Composites: II, Experimental Studies on Unidirectional Materials. J Am Ceram Soc 1995;78(10):2721-2731.

10. Curtin WA. Theory of Mechanical Properties of Ceramic-Matrix Composites. J Am Ceram Soc 1991;74(11):2837-2845.

11. Thouless MD, Evans AG. Effects of pull-out on the mecanical properties of ceramic-matrix composites. Acta Metall. 1988; 36(3):517-522.

12. Longbiao L. Modeling first matrix cracking stress of fiber-reinforced ceramic-matrix composites considering fiber fracture. Theor Appl Fract Mech. 2017; 92:24-32.

13. D. Gursoy, F. De Carlo, X. Xiao, C. Jacobsen, TomoPy: a framework for the analysis of synchrotron tomographic data, J. Synchrotron Radiat. 21 (5) (2014) 1188–1193.

14. P. Cloetens, M. Pateyron-Salomé, J.Y. Buffiere, G. Peix, J. Baruchel, F. Peyrin, M. Schlenker, Observation of microstructure and damage in materials by phase sensitive radiography and tomography, J. Appl. Phys. 81 (9) (1997) 5878–5886.

15. Bunsell AR, Piant A. A review of the development of three generations of small diameter silicon carbide fibres. J Mater Sci. 2006; 41(3):823-839.

16. Dunn D. The effect of fiber volume fraction in HiperComp^{TM} SiC-SiC Composites. Ph.D. Thesis, Alfred University. 2010.

17. Lamon J, Mazerat S, R'Mili M. Reinforcement of ceramic matrix composites: properties of SiC-based filaments and tows. In: Bansal NP, Lamon J. editors. Ceramic matrix composites: materials, modeling, and technology. Hoboken, NJ: John Wiley & Sons, Inc, 2014; p. 1-26.

18. Chateau C, Gélébart L, Bornert M, Crépin J, Caldemaison D, Sauder C. Modeling of damage in unidirectional ceramic matrix composites and multi-scale experimental validation on third generation SiC/SiC minicomposites. J Mech Phys Solids. 2014; 63(1):298-319.

19. Morscher GN, Gordon NA. Acoustic emission and electrical resistance in SiC-based laminate ceramic compsoites tested under tensile loading. J Eur Ceram Soc. 2017; 37(13):3861-3872.

20. J. Lamon, F. Rebillat, A.G. Evans, Microcomposite test procedure for evaluating the interface properties of ceramic matrix composites, J. Am. Ceram. Soc. 78 (2) (1995) 401–405.

21. Hay RS, Chater RJ. Oxidation kinetics strength of Hi-Nicalon^{TM}-S SiC fiber after oxidation in dry and wet air. J Am Ceram Soc. 2017; 100(9):4110-4130.

22. Meyer P. Experimental and numerical investigation of the damage response of ceramic matrix composites. Ph.D. Thesis, University of Michigan. 2015

Chapter IV. Matrix Crack Progression in Cross-ply SiC/SiC CMCs in Tension using Micro-CT Analysis

4.1 Introduction

The addition of high strength fibers to ceramics to form CMC allows for toughening and high tensile strains prior to failure. In unidirectional CMCs, fibers are aligned in one direction, usually parallel to the loading direction, as discussed in Chapter 2 and Chapter 3. Cross-ply composites consist of both longitudinal plies where fibers are aligned in the loading direction and transverse plies where fibers are aligned perpendicular to the loading direction. In this chapter, micro-CT observations of damage evolution are presented for cross-ply melt-infiltrated CMCs that consisted of a $[0°/90°]_s$ layup, symmetric around a SiC center matrix only region.

The ability to observe the progression and evolution of damage development that occurs while the composite specimen is under load is essential in order to model the damage behavior to provide input for lifetime assessment in service conditions. As discussed for the unidirectional specimens, in CMCs there are three main types of damage mechanisms: matrix cracking, fiber/matrix debonding, and fiber fragmentation.[4-8] For cross-ply composites under tensile load, damage first occurs as small matrix cracks, often referred to as “tunneling cracks”, that occur within the center matrix rich region and in the weaker transverse plies.[9-15] As applied stress continues to increase, the initial tunnel cracks will lengthen and propagate through the longitudinal plies and eventually create a through-thickness matrix crack that will extend through all eight plies of the composite. It is the onset of these matrix cracks that allows for non-linear stress-strain behavior of the overall composite which results in an increase in toughness when compared to monolithic ceramics. The matrix crack spacing or density of through-thickness matrix cracks is often described by shear-lag theory.[16-17] It has been shown that the SiC/SiC system specifically can have low crack densities and high interfacial shear stresses which can result in larger proportional limits and higher composite strengths.[11]

Ceramic matrix composites exhibit linear elastic behavior up until the onset of matrix cracking. This change in behavior from linear elastic behavior to non-linear behavior, is often referred to in the CMC literature as the proportional limit.[3] One of the main differences between cross-ply and unidirectional composites is the stress at which the onset of matrix cracking occurs. For cross-ply composites, matrix cracking initiates at much lower applied stresses, resulting in a lower proportional limit.[9] In cross-ply composites, the 0°, longitudinal plies, provide toughening where the weaker 90°, transverse plies do not. When matrix cracking occurs in a unidirectional specimen, the applied load at the matrix crack plane is distributed between all of the fibers. In comparison, when a matrix crack occurs in a cross-ply composite, the load is only distributed to the fibers in the loading direction within the longitudinal plies. Both unidirectional and cross-ply composites will exhibit fiber fragmentations at some stress after the proportional limit.

---

[3] This is not the same thing as the plastic proportional limit in ductile materials but is rather the point at which ceramic composites exhibit non-linear behavior.

Due to the variation in their microstructure, it is important to develop a detailed understanding of the relationship between the microstructure of ceramic matrix composite specimens and how damage evolves throughout the specimen on both a micro and macro scale. Micro-CT was used to observe the initiation and growth of damage in cross-ply CMC specimens as a function of applied stress. Micro-CT techniques, including both lab scale CT and synchrotron tomography, has been used to study damage evolution in SiC/SiC CMCs although most of these studies have been limited to unidirectional specimens or minicomposites.[18-23] Utilizing in situ tomography to image while the specimen is under tensile load allows for matrix cracks to be observed while still under tensile load avoiding the common issue that residual stress causes matrix cracks to close up after failure.[24]

The initial tunneling matrix crack in each specimen was detected and its evolution of the across each specimen was tracked as it extended through each of the eight plies of the composite while under increasing applied stress. Although damage mechanisms such as matrix cracking and fiber breaking was identified using micro-CT, debonding was not able to be observed using these tomography techniques due to contrast and resolution issues discussed in Chapter 3.

4.2 Methods and Materials

X-ray tomography was performed at the Advanced Light Source (ALS) synchrotron facility at Lawrence Berkeley National Lab. Two 8-ply $[90°/0°]_s$ cross-ply HiPerComp^{TM} composite specimens with 28 volume % SiC Nicalon Type S fibers were imaged using the full spectrum of the x-ray beam while under tensile load. The cross-ply HiPerComp^{TM} specimens were manufactured by GE Aviation using their melt-infiltration process described in Chapter 1. The 3D volume of one of these cross-ply specimens imaged while under tensile load using the ALS is depicted in Figure 4.1 where the transverse (90°) and longitudinal (0°) plies can easily be distinguished within the volume.

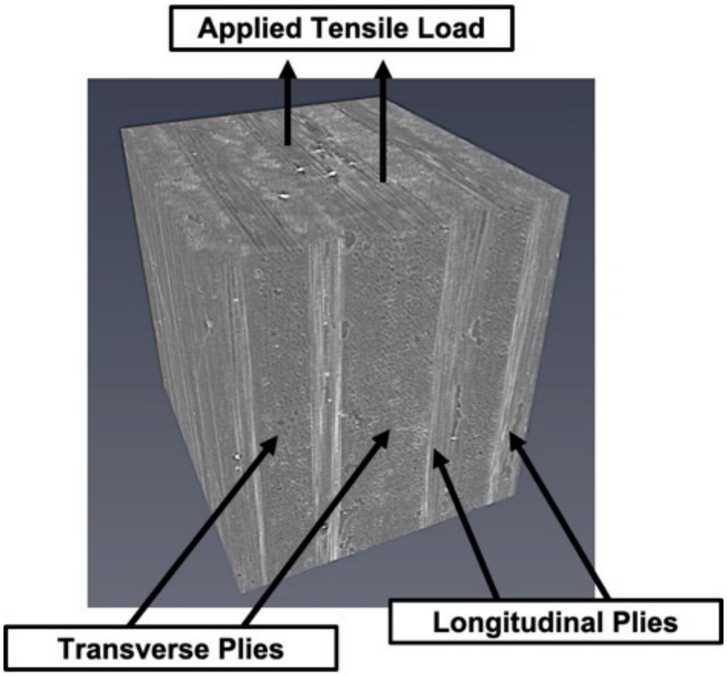

Figure 4.1 3D volume of the cross-ply specimen tested in tension and imaged using micro-CT techniques

The applied stress increments at which each specimen was imaged are listed in Table 4.1. Specimen 1 and Specimen 2 failed at an applied stress of 248 MPa and 254 MPa respectively and the stress vs. displacement plots for each specimen are shown in Figure 4.2

Table 4.1 The stress increments at which each specimen was imaged at while under load

Specimen 1	**Specimen 2**
9 MPa	110 MPa
187 MPa	150 MPa
195 MPa	177 MPa
204 MPa	194 MPa
212 MPa	210 MPa
221 MPa	217 MPa
229 MPa	226 MPa
238 MPa	238 MPa
246 MPa	246 MPa
Failed: 248 MPa (Not Imaged)	*Failed: 254 MPa (Not Imaged)*

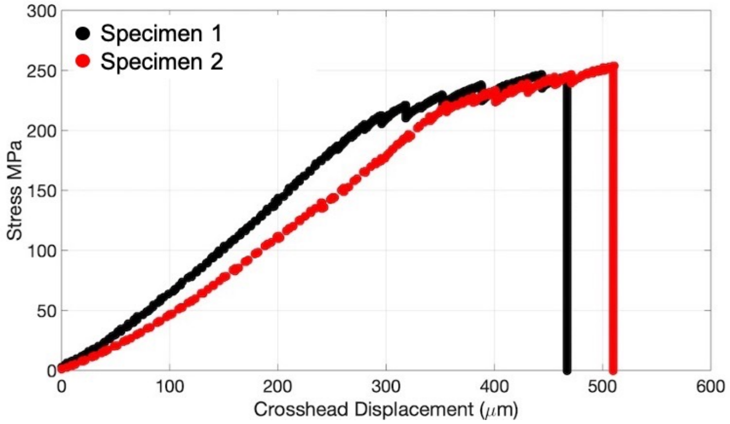

Figure 4.2 Stress vs. crosshead displacement for Specimen 1 (Black Curve) and Specimen 2 (Red Curve).

The loading stage, described in Chapter 2, was used in displacement control and Figures 4.3a and 4.3b correspond to the load and displacement as a function of time for Specimen 1 and Specimen 2 respectively. On these displacement curves, the hold time required for x-ray imaging can be discerned from the areas where there was no change in the crosshead displacement which indicates that the imaging process could take between five-ten minutes.

(a)

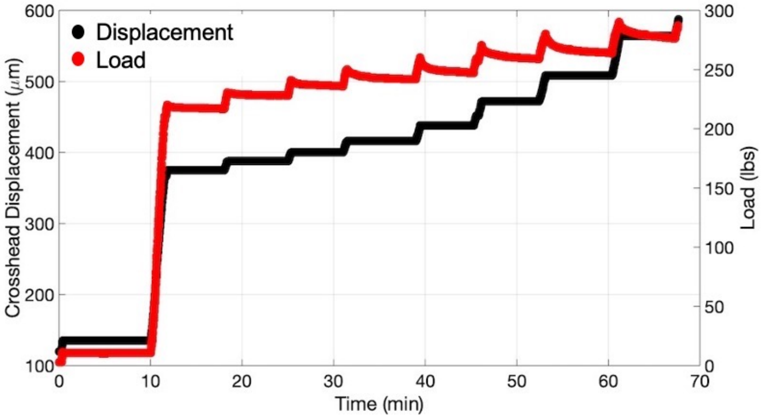

(b)

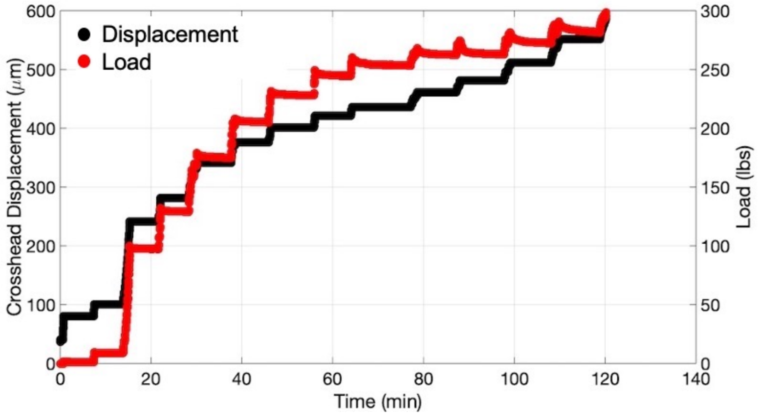

Figure 4.3 Crosshead Displacement and Load vs. Time for (a) Specimen 1 (b) Specimen 2

4.2.1 Matrix Crack Segmentation

Using synchrotron tomography allows for the rendering of 3D images which results in the ability to track and quantify different features and characteristics within the volume of a specimen. Certain features within a material volume can be distinguished and quantified through image segmentation. The process of image segmentation consists of grouping sets of pixels into different "objects" relating to one's data set. For example, some of the "objects" or groups that could be segmented in these CMC specimens include sorting pixels into groups that correlate to the matrix cracks, dense SiC matrix material, dense SiC fibers, or fiber fragmentations. For this work, segmentation of two matrix cracks in Specimen 1 was accomplished and the results and observations are described in Section 4.3.4. The matrix crack segmentation was performed manually by examining pixels (the resolution of the scan was 1.3 μm/pixel) and grouping the ones that were defined, by manual visual determination, as part of the matrix crack together into one group. The pixels that were deemed part of the matrix crack were chosen based on their black/grey scale. The matrix crack opening is only pixels in height and therefore an accurate measurement of the crack opening was not obtainable due to the limited resolution of the scan.

4.3 Detailed Micro-CT Observations

Matrix crack evolution was tracked throughout the volume of each specimen at incremental applied stresses above and below the proportional limit which allowed for the observation of the onset of the initial tunneling matrix crack in both cross-ply specimens. The progression of the initial matrix crack into subsequent nearby plies was detailed and Tables 4.2 and 4.3 list the stresses at which a matrix crack was first observed in each individual ply for Specimen 1 and Specimen 2 respectively. By the final imaged stress increment (246 MPa) there were two through-matrix cracks, i.e. the matrix crack eventually traversed through the entire width and thickness of the composite specimen, observed within the field of view for both specimens. The two matrix cracks in each specimen will be labeled Crack A and Crack B corresponding to the matrix crack that was observed first and second respectively within the volume of each specimen. A matrix crack spacing of 1100 μm and 1400 μm was calculated for Specimen 1 and Specimen 2 respectively with a corresponding matrix crack density of 0.71 cracks/mm for both specimens. It is difficult to compare matrix crack spacing and crack density of these specimens to other studies with certainty since there were only two matrix cracks within the field of view. However, there have been other experimental analyses that have reported matrix crack densities of 2.0 ± 1.1 cracks/mm measured in the longitudinal plies of SiC/SiC cross-ply laminate composites.[25] It is reasonable to have 0.71 cracks/mm in these materials however with only two matrix cracks in the field of view it is possible that this was not representative of the matrix crack density along the full length of the specimen.

4.3.1 Matrix Crack Evolution in Specimen 1

Crack A in Specimen 1 was initially observed at an applied stress of 195 MPa whereas Crack B wasn't observed until 212 MPa. The progression of Crack A in Specimen 1 over the range of 180 MPa – 221 MPa is shown in Figure 4.4. Crack A was first observable as a tunnel crack in the center matrix rich region at 195 MPa (Figure 4.4a), and by 204 MPa (Figure 4.4b) the matrix crack had traversed into the adjacent transverse ply and through the entire width of the right adjacent longitudinal ply as seen in Figure 4.4b. At an applied stress of 212 MPa (Figure 4.4c) Crack A was identified in six plies within the field of view, including both of the center longitudinal plies. An additional partial matrix crack that extends through the three rightmost plies, was detected at this stress approximately 200 μm above Crack A in the right longitudinal ply. Figure 4.4d depicts the evolution of Crack A into all eight plies and the additional partial matrix crack first observed in Figure 4.4c is still evident, but it hasn't extended through the center transverse plies and hasn't connected with Crack A. The 2D slices that are shown in Figures 4.4a-d are taken 700 μm from the front face of the specimen.

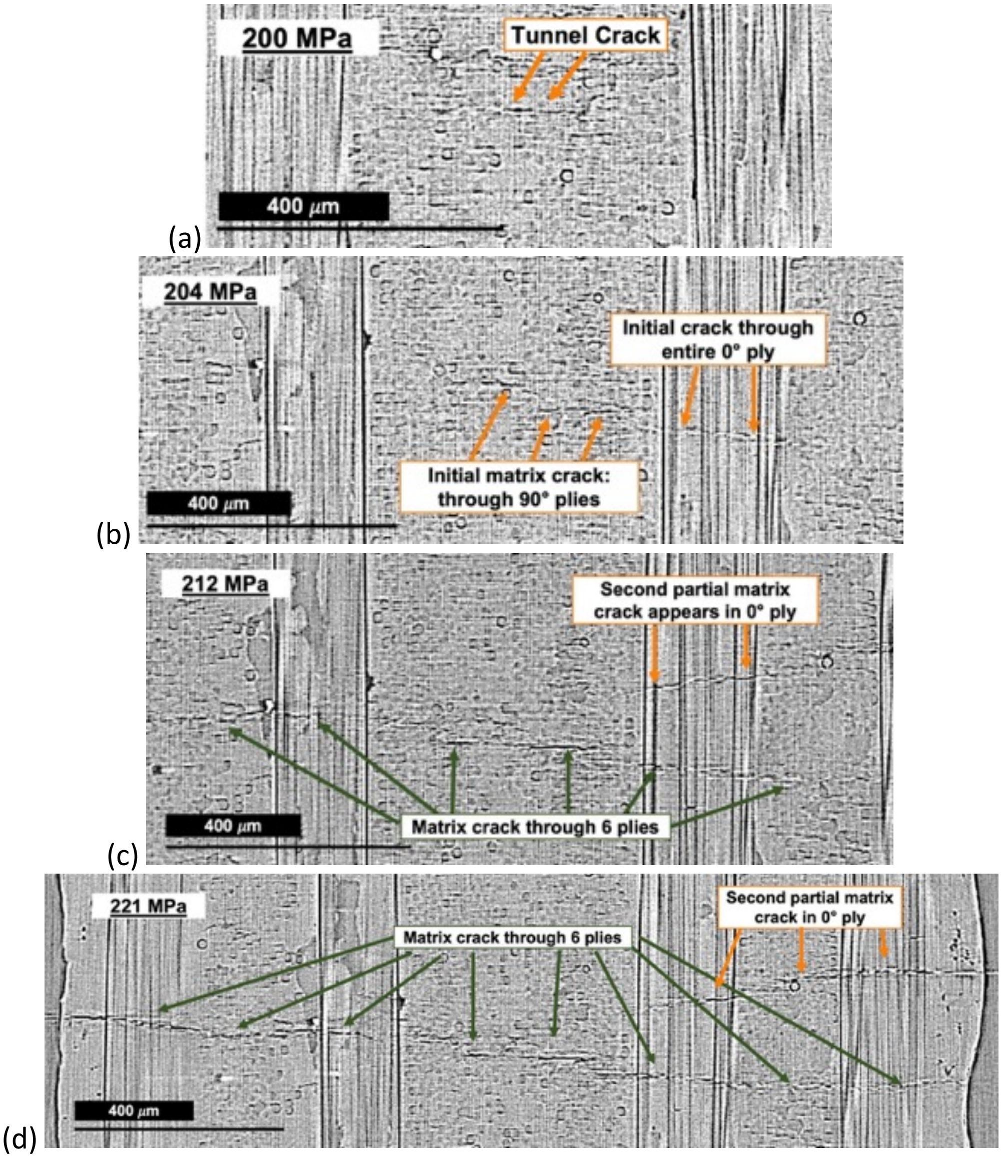

Figure 4.4 progression of Crack A in Specimen 1 in the sagittal plane approximately 700 μm from the front face of the specimen at increasing stress increments of: (a) 195 MPa, the initial tunnel crack in the matrix rich region was observed (b) 204 MPa, the initial crack in longitudinal ply is detected (c) 212 MPa, the crack continues to extend into outer transverse plies (d) 221 MPa, the crack is shown to have extended through all eight plies

The same matrix crack (Crack A) in Specimen 1 is depicted in Figures 4.5a-d but the 2D slices are taken from a different position within the volume of the specimen in order to emphasize how the matrix crack plane alters throughout the volume of the specimen. Also, Figures 4.5a-d represent the crack progression of Crack A at higher stress increments of 212 –

247 MPa. When comparing the cracking behavior of Crack A at an applied stress of 212 MPa but at two different locations within the volume (Figure 4.4c and Figure 4.5a), bifurcation was detected in the center left longitudinal ply in Figure 4.5a, whereas a uniform matrix crack was observed in Figure 4.4c. The bifurcation was measured and it occurred for a length of 750 μm through the thickness of the specimen. A partial matrix crack was also detected in the right longitudinal ply that is the same partial crack that was detected in Figure 4.4c and 4.4d. Between the stress increments of 212 and 221 MPa (Figure 4.5a and Figure 4.5b), there wasn't a significant change in the observed matrix crack behavior, although it appeared that there was a minor growth in the matrix opening. Recall that due to imaging resolution limitations, all crack opening observations are qualitative not quantitative. The matrix crack opening of Crack A appears to be marginally greater in the transverse plies than in the longitudinal plies at 221 MPa. By 238 MPa, shown in Figure 4.5c, Crack A had a distinct increase in matrix crack opening, in all of the plies, when compared to the crack opening examined at lower applied stresses. By 238 MPa (Figure 4.5c), the matrix crack that was initially labelled as a partial matrix crack progressed into the center transverse ply and appeared to partially connect with the original matrix crack and in the last imaged stress increment at 247 MPa (Figure 4.5d), fully connects with Crack A.

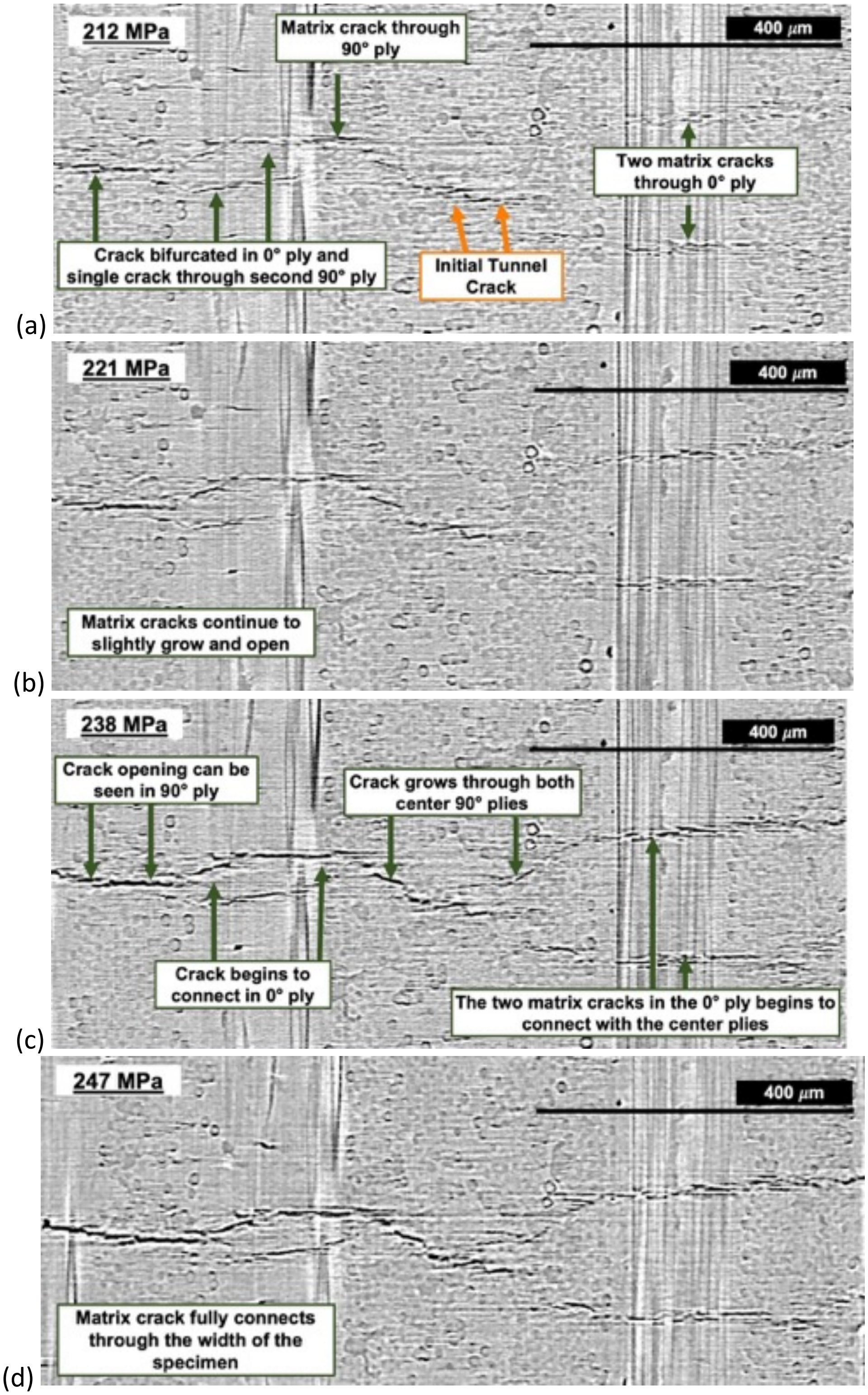

Figure 4.5 Continued progression of Crack A in Specimen 1 at a location within the volume ~1700 *μm* from the front face and at higher stress increments of: (a) 212 MPa, (b) 221 MPa, (c) 238 MPa, and (d) 247 MPa

Crack B was first detected in Specimen 1 at an applied stress 32 MPa greater than that of the initial matrix crack (Crack A). The progression of Crack B in Specimen 1 at the stress increments of 230, 238, and 247 MPa is shown in Figures 4.6a, 4.6b, and 4.6c respectively. At 230 MPa, the matrix crack can be observed in the six plies within the field of view, although the crack opening is relatively small. The crack opening of Crack B appears to increase when imaged at the stress increment of 238 MPa in Figure 4.6b and the crack opening appears to be greater in the transverse plies than the opening observed in the longitudinal plies comparable to the crack behavior observed for Crack A. Also similar to Crack A, Crack B appears to bifurcate into two cracks when it extends through the longitudinal plies. At 238 MPa, the left center longitudinal ply has two matrix cracks while the right longitudinal ply has up to four tiny (in relation to matrix crack opening) matrix cracks. In Figure 4.6c, at 247 MPa, the matrix crack bifurcations fully connect to form a linear matrix crack in the transverse plies and there was a greater overall distinction in the matrix crack opening.

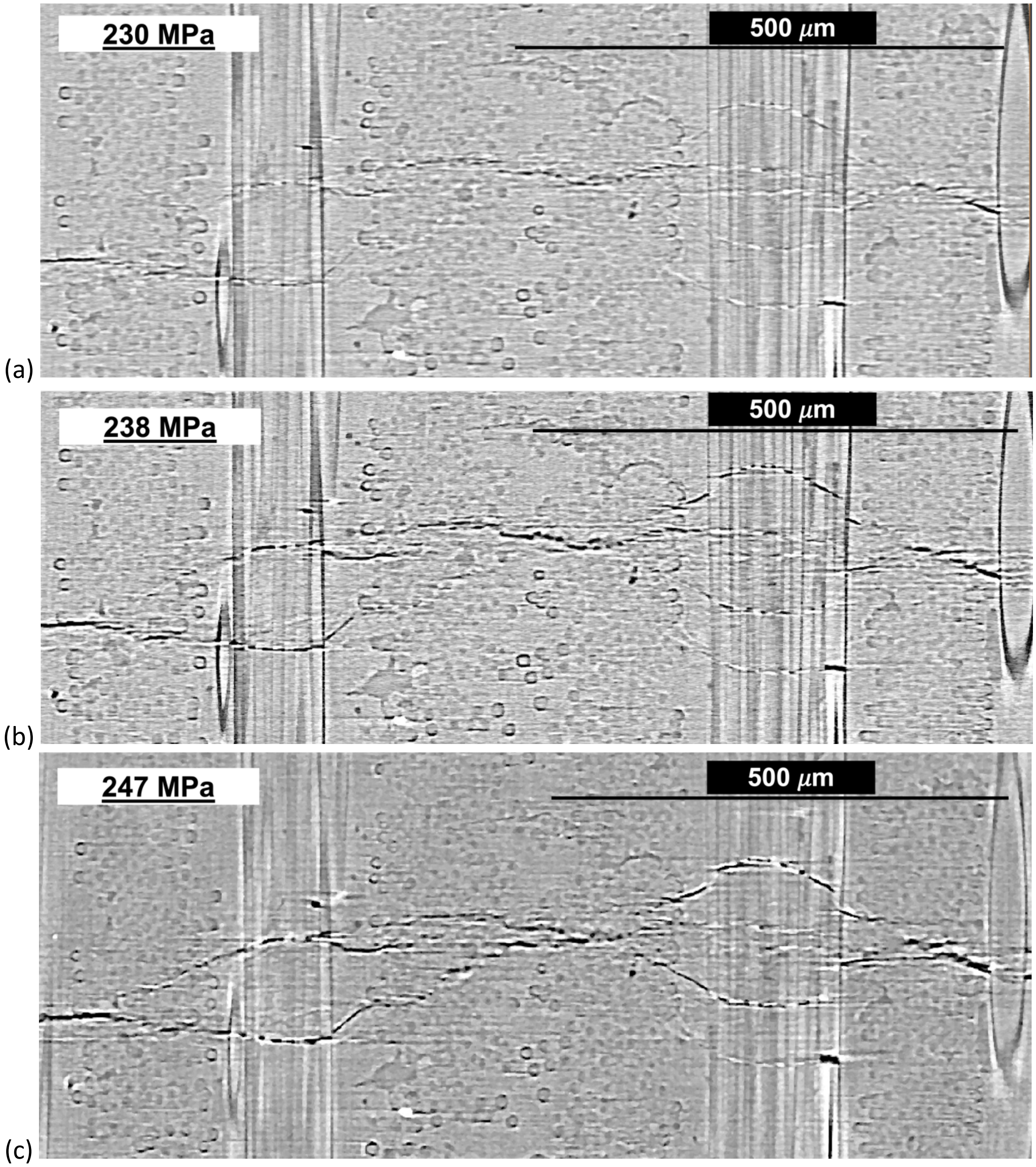

Figure 4.6 the progression of Crack B in Specimen 1 taken ~1000 μm from the front face (approximately near the middle of the volume of the specimen) at stress increments of: (a) 230 MPa, (b) 238 MPa, and (c) 247 MPa

Figure 4.7a-d examines the progression of multiple matrix cracks detected in the right center longitudinal ply. Figure 4.7a shows low resolution snapshots of the larger composite architecture to provide anchoring for the regions examined in higher resolution detail in Figure

4.7b-d. At 230 MPa, shown in Figure 4.7b, there are five matrix cracks that extended through the longitudinal ply and there doesn’t appear to be any significant distinction between the five cracks in terms of their length and opening except the bottommost crack has a small fiber break that occurred in the wake of the matrix crack. When comparing the behavior of these cracks at the next stress increment of 238 MPa, the uppermost crack “dominates”, meaning its crack opening is greater in comparison to the other cracks, while there doesn’t appear to be a considerable change in the behavior of the five other cracks. However, when stress increases from 238 MPa to 247 MPa in Figure 4.7c, two of the original four tiny matrix cracks appear to “dominate”, one of which is the top matrix crack which had a larger opening at 238 MPa. Meanwhile, the other matrix cracks that initially appeared in 230 and 238 MPa now appear to “close up” i.e. the matrix crack opening decreased for some matrix cracks while the opening of the dominant matrix cracks increased.

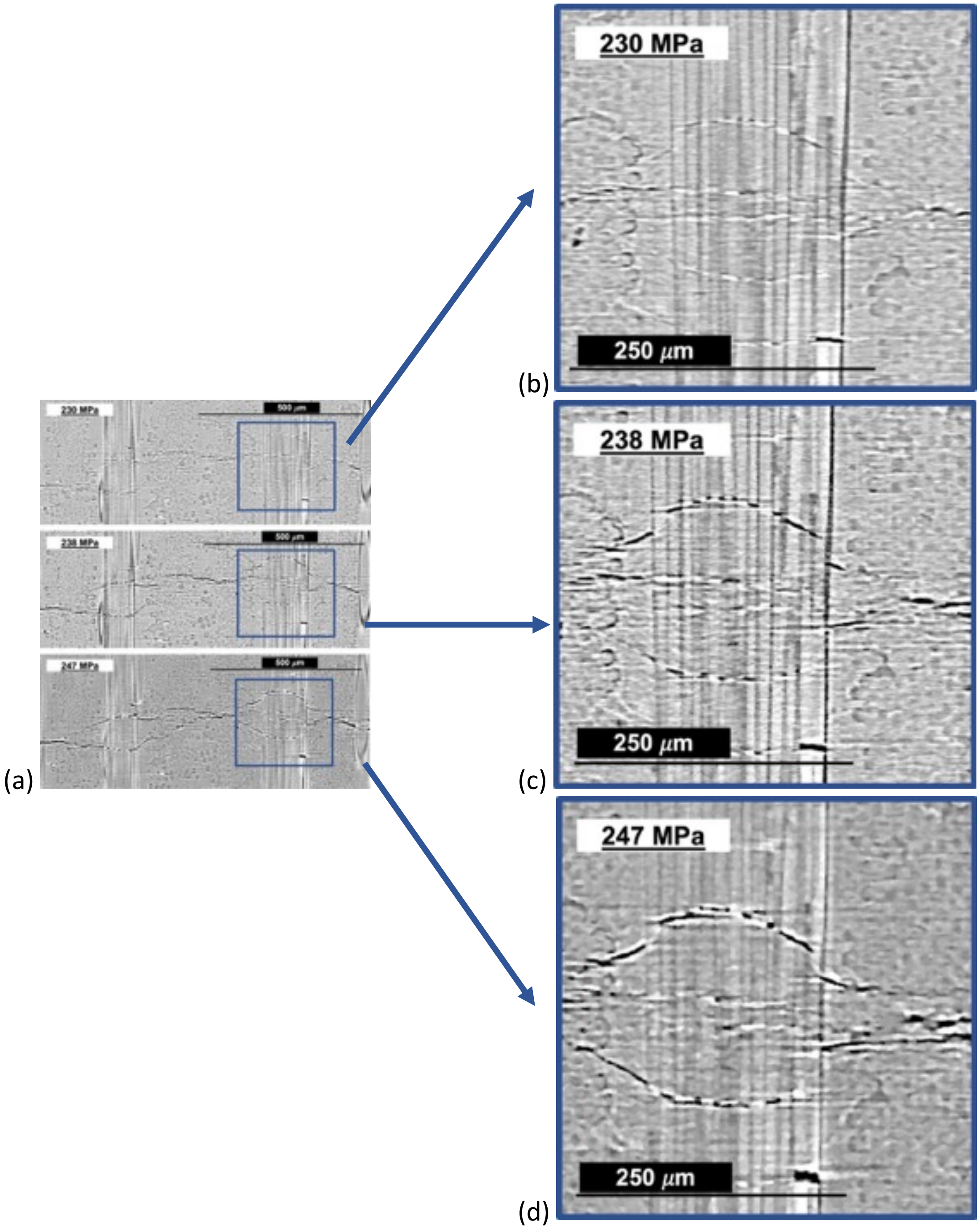

Figure 4.7 a closer look at how the matrix crack continues to grow and open within one of the longitudinal ply within Specimen 1 at stress increments of: (a) overall crack formation from Figure 4.6 (b) 230 MPa, five tiny initial matrix cracks (or bifurcations) can be seen (c) 238 MPa, some cracks appear to have a larger opening when compared to others (d) 247 MPa, two of the original five cracks have "dominated" and have larger openings

4.3.2 Matrix Crack Evolution in Specimen 2

For Specimen 2, Crack A was detected as a tunnel crack in the center matrix rich region at 210 MPa and was the top crack within the field of view, shown in Figure 4.8a. Along with the initial tunnel crack shown in Figure 4.8a, there was a small matrix crack observed in the right center longitudinal ply but the crack did not extend across the entire ply width. This behavior is unexpected considering the many studies and models that have been published and predict that cracking in the weaker transverse plies should occur prior to damage within the load bearing longitudinal plies. By 217 MPa, Crack A had extended through all eight plies of the composite as shown in Figure 4.8b. The matrix crack didn't appear to grow in length or in opening between the imaged applied stresses of 217 MPa and 226 MPa depicted in Figures 4.8b and 4.8c respectively. At 246 MPa, the matrix crack appeared to have an increased opening along the left side of the imaged section specimen when compared to the crack in the right three plies, shown in Figure 4.8d. This change in matrix crack opening is distinct and the matrix crack along the right three plies within the field of view seem to a more jagged plane and behavior to it when compared to the left side with the larger opening.

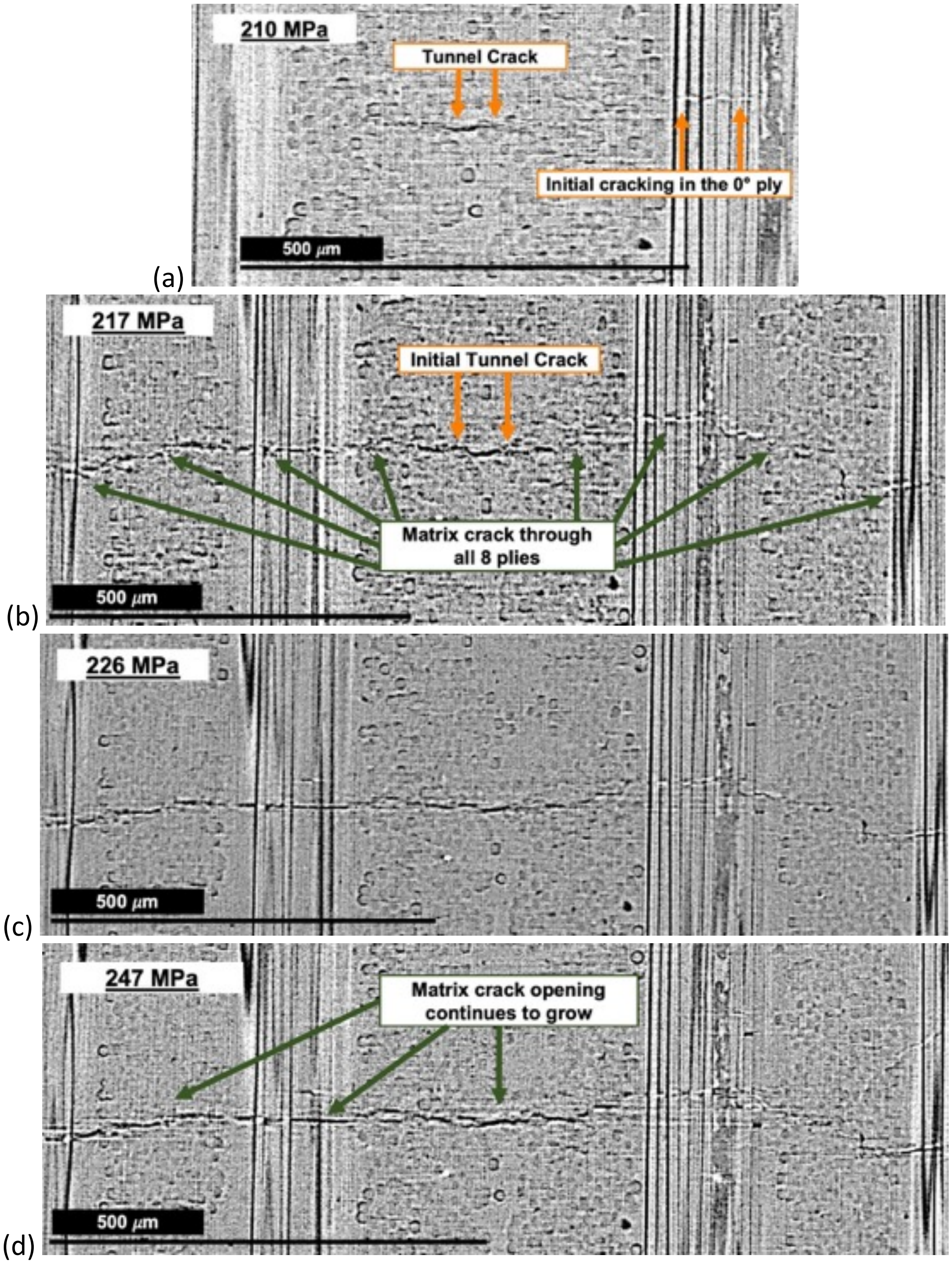

Figure 4.8 progression of Crack A in Specimen 2 in the XZ face approximately 200 *μm* from the front face of the specimen.at increasing stress increments of: (a)210 MPa, the initial tunnel crack in the matrix rich region was observed along with an initial crack in the right longitudinal ply (b) 217 MPa, Crack A had extended into all 8 plies (c) 226 MPa, there is no distinct change in the matrix crack behavior (d) 247 MPa, the matrix crack opening increased within the left four plies

The initiation of Crack B in Specimen 2 was not imaged; Crack B was not visible at 217 MPa, and when imaged at 226 MPa was already extended across size of the eight plies. The progression of Crack B in Specimen 2 is depicted in Figures 4.9a-c. There was also a silicon vein visible in Figure 4.9a which looks similar to a matrix crack. The silicon vein is a result of the residual silicon left in the matrix due to the melt infiltration process and often resembles a matrix crack because the silicon filled in shrinkage cracks from an earlier step during manufacturing. Its x-ray density is lower than that of the SiC but not as low as a matrix crack (air) and therefor can be distinguished between the two. The matrix crack appears to bifurcate in the right longitudinal ply similar to the matrix cracking behavior observed in Specimen 1. Within the left longitudinal ply there are two separate matrix cracks detected in the image, the top partial crack in Figure 4.9b originated in the longitudinal ply and extended into the transverse ply. At 238 MPa, the matrix crack opening is slightly larger when compared to the matrix crack opening observed at 226 MPa and the left center longitudinal ply still appears to have two matrix cracks, (1) the extension of Crack B and (2) the partial matrix crack that is not connected to Crack B at any point throughout the volume of the specimen. There was an additional partial matrix crack detected in the right three plies (longitudinal/ transverse/ longitudinal) approximately 350 μm directly above Crack B. At 247 MPa, the final imaged stress increment depicted by Figure 4.9c, the crack opening of Crack B appears slightly larger no changes to crack length or morphology are evident. At 247 MPa, the top matrix crack that originated in the left center longitudinal ply merged with Crack B to form a through thickness matrix crack. The partial matrix crack initially observed in Figure 4.9b has extended marginally in length into the center right transverse ply but did not expand across the width of the specimen.

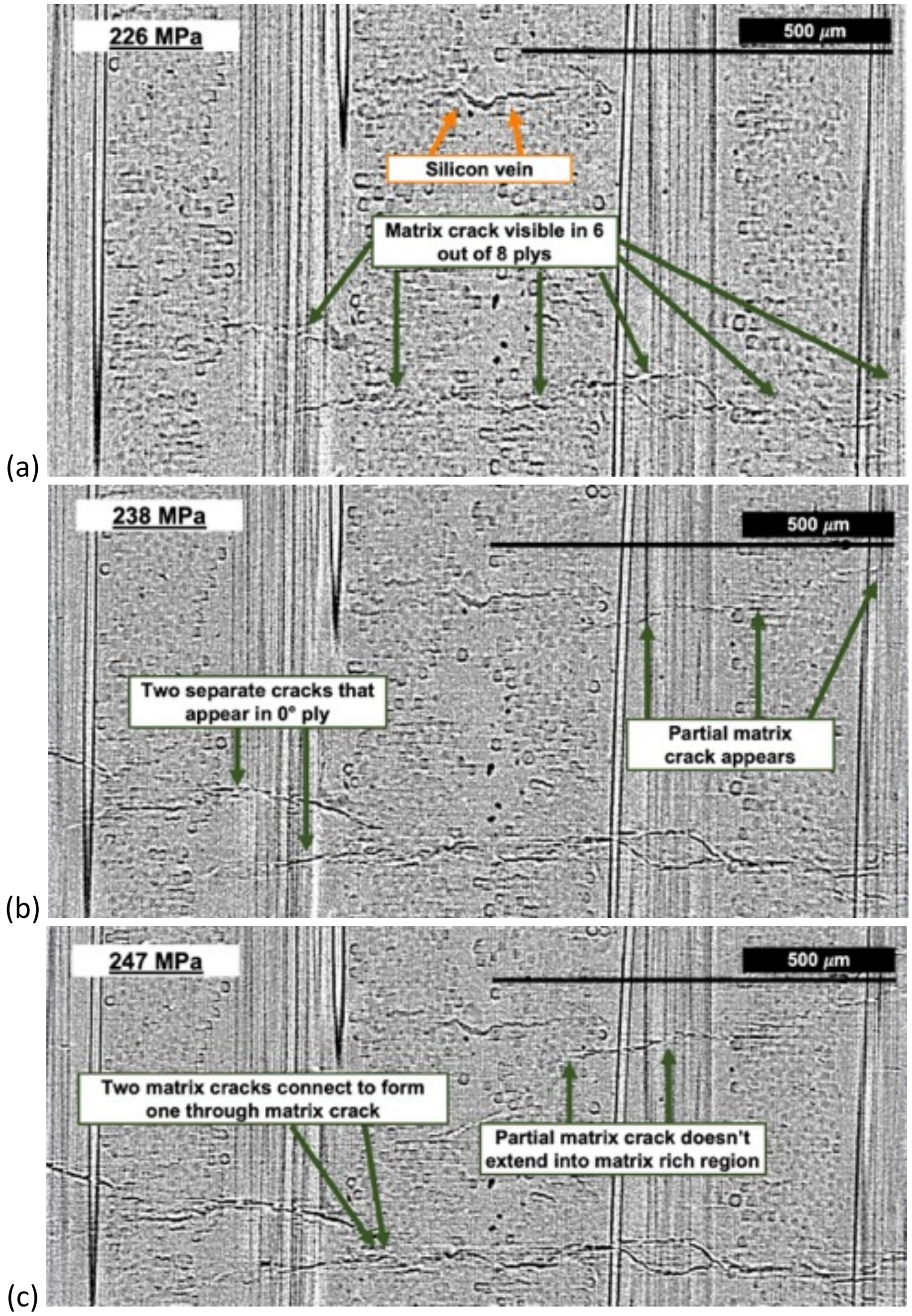

Figure 4.9 the progression of Crack B in Specimen 2 taken ~1200 *μm* from the front face at stress increments of (a) 226 MPa, a silicon vein can be detected and Crack B is in observed in six plies (b) 238 MPa, two partial matrix cracks appear within in the field of view (c) 247 MPa, one of the partial cracks connects with Crack B while the second partial crack extends slightly into the center transverse ply but does not create a through-thickness crack

4.3.3 The Comparison of Matrix Cracking Behavior

The overall matrix cracking behavior between these two specimens was similar with some slight differences. The most frequent matrix cracking behavior that was detected in both specimens was the bifurcation of the matrix crack in longitudinal plies. It is known that the fiber coating applied to the outside of tows is often thicker than the fiber coating applied to the center fibers within the tow. It is possible that once a matrix crack extends from the matrix rich region and transverse plies into the longitudinal plies where there is a thicker coating near the edge of the plies, that debonding occurs above and below the matrix crack plane and the matrix crack then bifurcates due to the subsequent debonding. Another matrix cracking behavior that was observed in both specimens was that the matrix crack opening was often greater in the transverse plies than the longitudinal plies. This is most likely due to the bridging fibers that are carrying load and causing closing traction on the crack in the longitudinal plies whereas the fibers in the transverse plies are not in the loading direction and cannot effectively bridge cracks. However, as stress is increased and fibers begin to break and no longer carry load, the difference in matrix crack opening between the transverse and longitudinal plies becomes minimal. The last similar observation between both specimens was that the second matrix crack (Crack B) that was detected in each specimen was no initially observed as a tunnel crack, but rather seemed to progress rapidly and first appear extended into multiple plies including longitudinal plies.

The biggest difference in matrix crack progression between the two specimens was how rapidly the matrix cracks evolved. In Specimen 1, Crack A was first detected as a tunnel crack, then extended slowly across multiple stress increments into nearby plies individually. Whereas in comparison, Crack A in Specimen 2 was detected as a tunnel crack and then by the next stress increment the crack had extended into all eight plies. Tables 4.2 and 4.3 describe whether the crack had extended into an individual ply at an individual stress increment. The plies were labelled Ply 1- Ply 8 going left to right in the images shown.

Table 4.2 the stress increment at which matrix cracking was detected within each ply of Specimen 1 (with X depicting an observed matrix crack within that respective ply)

Specimen 1, Crack A: Matrix Crack Observations in Individual Plies									
Stress Increment	Ply 1 (0°)	Ply 2 (90°)	Ply 3 (0°)	Ply 4 (90°)	Matrix Region	Ply 5 (90°)	Ply 6 (0°)	Ply 7 (90°)	Ply 8 (0°)
195 MPa					X				
204 MPa					X	X			
212 MPa		X	X	X	X	X	X	X	
221 MPa	X	X	X	X	X	X	X	X	X
229 MPa	X	X	X	X	X	X	X	X	X
238 MPa	X	X	X	X	X	X	X	X	X
246 MPa	X	X	X	X	X	X	X	X	X

Table 4.3 the stress increment at which matrix cracking was detected within each ply of Specimen 2 (with X depicting an observed matrix crack within that respective ply)

Specimen 2, Crack A: Matrix Crack Observations in Individual Plies									
Stress Increment	Ply 1 (0°)	Ply 2 (90°)	Ply 3 (0°)	Ply 4 (90°)	Matrix Region	Ply 5 (90°)	Ply 6 (0°)	Ply 7 (90°)	Ply 8 (0°)
210 MPa					X		X		
217 MPa	X	X	X	X	X	X	X	X	X
226 MPa	X	X	X	X	X	X	X	X	X
238 MPa	X	X	X	X	X	X	X	X	X
246 MPa	X	X	X	X	X	X	X	X	X

4.3.4 Observations from Segmentation of Matrix Crack

The matrix crack opening was large enough at the highest imaged applied stress increment of 247 MPa that the segmentation of two through thickness matrix cracks was accomplished in Specimen 1. Figure 4.10a displays the segmentation of the two matrix cracks in

Specimen 1 at 247 MPa with the gold representing the pixels that were grouped into the matrix crack plane. The bottom crack in Figure 4.10a is Crack A the top crack is considered Crack B and these cracks are displayed in 3D with the segmented matrix crack coming out of the plane and the X and Z directions representing the thickness and height of the specimen respectively. The denser gold regions are locations where the matrix crack was more distinct, i.e. locations with larger amounts of pixels considered to be part of the matrix crack. Areas where the crack appears to be missing or where there is unoccupied space is due to the lack of pixels considered to be part of the matrix crack which could be due to the matrix crack not existing at that location yet or the opening of the crack wasn’t large enough to be segmented. Figure 4.10b is a 2D image of the top down view of Crack B where the white represents the segmented crack. In this image the crack is presented in terms of its width and thickness, and the z direction is the height of the imaged field of view which is coming out of the plane of view. In Figure 4.10b the black circles, dots, and other black areas are locations where the pixels were not segmented or grouped as part of the matrix crack segmentation. In the longitudinal plies where there are large amounts of black dots, represents locations where there are no matrix crack pixels due to the fact that there are bridging fibers the matrix crack did not penetrate through; in this view the bridging fibers would be coming out of the plane. The segmentation of the matrix crack allows the viewer to see that certain areas of the crack have more pixels than others, which relates to a larger crack opening. In the matrix crack segmentation shown in Figures 4.10a and 4.10b, some general observations were that there are more pixels segmented as part of the matrix crack in the transverse plies than in the longitudinal plies which is due to the longitudinal plies have bridging fibers in the loading direction which does allow the matrix crack to have as large of an opening as was discussed in the previous section.

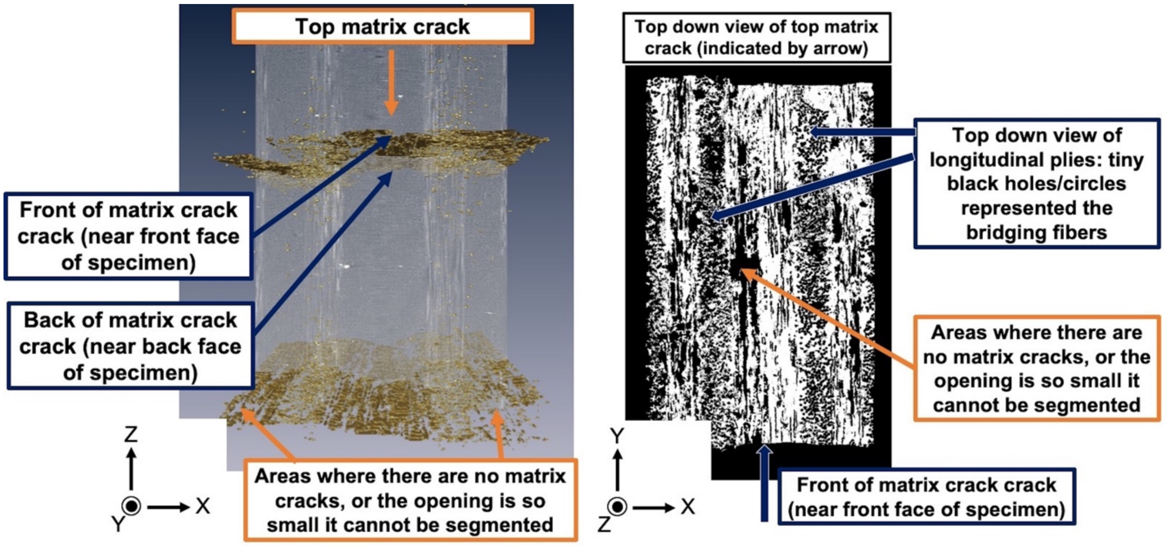

Figure 4.10 segmentation of Crack A and Crack B where (a) depicts the two matrix cracks in the field of view segmented out and (b) is the view of looking top down on the segmented matrix crack. Can see where the crack went through the matrix right region, black section represents bridging fibers or uncracked region of specimen

4.4 Comparing Observed Matrix Cracking Behavior to Mechanical Models

The ability to predict damage mechanisms, such as matrix cracking, that occurs within SiC/SiC CMCs under load is crucial for improving life prediction capabilities. The matrix cracking observations that were obtained using micro-CT were compared to theoretical mechanical models and the following sections will compare experimental observations to various mechanical model predictions of a) the onset of matrix crack, b) the extension of matrix cracking into the longitudinal plies and c) the ultimate failure strength, UTS, of these specimens. Table 4.4 lists the values for the observed matrix crack behavior, the predicted behavior, and the comparison of observations to other reported experimental studies.

4.4.1 Onset of Matrix Cracking, "Tunnel Cracks"

As stated previously, it has been predicted that matrix cracks first occur in the form of tunnel cracks.[9] The stress at which the onset of these tunnel cracks was observed was compared to the predicted onset of matrix cracking stress using well-known mechanical models from the literature. It has also been observed that additional cracking in the adjacent transverse plies occurs before there is any cracking observed in the longitudinal plies. For cross-ply composites, material properties are determined by the ply properties and up until the proportional limit, or the onset of matrix cracking, the composite is expected to behave linear elastically. The linear elastic properties in the plies that make up the composite (i.e. the transverse and longitudinal plies) are different. The material properties of the SiC matrix and SiC fibers were used to determine the expected ply behavior and are shown in Table II. The elastic moduli of the longitudinal (E_L) and transverse plies (E_T) were calculated using Equations (4.1) and (4.2) which are the rule of mixtures and Halpin Tsai equations respectively. These equations are based on the elastic moduli of the fiber and matrix and the fiber volume fraction of the composite.

$$E_L = v_f E_f + v_m E_m \tag{4.1}$$

$$E_T = \frac{1 + 2\eta v_f}{1 - \eta v_f} E_m \tag{4.2a}$$

$$\eta = \frac{\frac{E_f}{E_m} - 1}{\frac{E_f}{E_m} + 2} \tag{4.2b}$$

The stress required for the onset of tunneling matrix cracks has been previously derived from the steady-state energy release rate and is shown below in Equations (4.3a) and (4.3b).[9,13,14] These equations are dependent on $\overline{E}_0$: the plane strain Young's modulus, υ_L: the Poisson's ratio of the longitudinal ply, t: the thickness of a single ply and , $g\left(f, \frac{E_f}{E_m}\right)$: the elastic mismatch parameter which depends strongly on whether debonding between the fiber/matrix interface occurs and on the fiber volume fraction of the composite. If a crack is propagating entirely in the matrix then Γ is equivalent to Γ_m but if the tunnel crack is considered to be interacting with fiber interfaces, then Γ would be some fraction of Γ_m.[13] For the simplicity of this work it is going to be assumed that the tunnel crack is only interfering with the matrix and therefore Γ equals Γ_m. The residual stress in these HiPerComp^{TM} composites has been studied extensively and a value of 63 MPa will be used.[24,26,27] The values used for each material property to be able to calculate the onset of matrix cracking listed in Table 4.4

$$\sigma_{onset} = \sqrt{\frac{\Gamma \overline{E}_0}{t g\left(f, \frac{E_f}{E_m}\right)}} - \sigma_r \frac{(E_L + E_T)}{2E_T} \tag{4.3a}$$

$$\overline{E}_0 = \frac{E_L\left(1 + \frac{E_L}{E_T}\right)}{2\left(\frac{E_L}{E_T} - \upsilon_L^2\right)} \tag{4.3b}$$

Equation (4.3a) predicted a minimum stress of 205 MPa for the onset of matrix cracking, in the form of tunnel cracks, within the matrix rich region. Crack A in Specimen 1 initiated in the matrix only center region at 195 MPa whereas Crack A in Specimen 2 was first detected at 210

MPa. The variation for the onset of matrix cracking between the two cross-ply specimens was approximately 15 MPa and the onset of matrix cracking for both specimens was comparable to the predicted value. The onset of matrix cracking observed in Specimen 2 occurred only 5 MPa above the predicted value of 210 MPa while the initial matrix cracking in Specimen 1 was initially imaged 10 MPa below the predicted value. Morscher and Gordon have recently performed an AE study on GE's HiPerComp^{TM} CMC material behavior response under tensile load and reported both the first detected AE event and the first detected "loud" AE event in relation to matrix cracking. A "loud" AE event is characterized by the energy of the acoustic waveform and has been shown to correspond to transverse matrix cracking in SiC/SiC CMC materials. In Morscher and Gordon's study of multiple cross-ply composite specimens they reported the average first AE event occurred at 202 ± 13 MPa. It is likely that the first AE event they observed was due to the onset of matrix cracking within the matrix rich/double transverse layers within the center of the composite as it compares well to the observations of tunnel cracking at 195 MPa and 210 MPa for Specimen 1 and Specimen 2 respectively in this study.

4.4.2 Extension of Matrix Crack into Subsequent Plies

The extension of the initial primary tunnel crack into the load bearing longitudinal plies results in behaviors similar to that studied in unidirectional composite materials. However, the predicted stress at which matrix cracking should occur in the longitudinal plies is in relation to the stress that is acting on the longitudinal plies not the applied stress. The stress experienced by the longitudinal plies in relationship to the applied stress is not directly known and for a typical 0°/90° system, the stress acting on the longitudinal plies can be between the applied stress, σ, and up to double the applied stress, 2σ.[9] For the work presented in this section, the onset of matrix cracking for a unidirectional specimen is going to be compared to: (i) the applied stress (σ) at which matrix cracking was first observed in the longitudinal plies and (ii) two times the applied stress (2σ) at which matrix cracking was first observed in the longitudinal plies. The onset of matrix cracking for a unidirectional composite composed of fibers running parallel to the loading direction is defined by Equation (4.4) and was described in detail in Chapter 3.

$$\sigma_{mc}^{uni} = E_L \left[\frac{6\tau_s \Gamma_m v_f^2 E_f}{v_m E_m^2 r E_L} \right]^{\frac{1}{3}} - \sigma_r \tag{4.4}$$

The predicted stress at which the onset of matrix cracking in the longitudinal plies will occur using Equation (4.4), is 260 MPa. Matrix cracking was first observed in a longitudinal ply at an applied stress of 204 and 210 MPa for Specimen 1 and Specimen 2 respectively which is much lower (55-60 MPa lower) than the predicted onset of matrix cracking. However, the stress experienced by the longitudinal plies when matrix cracking was first observed could have been as large as 408 MPa and 420 MPa (2σ) for Specimen 1 and Specimen 2 respectively. Since the exact stress acting on the longitudinal plies isn't known it is difficult to directly compare the predicted matrix cracking stress in the longitudinal plies to the observations. The prediction of 262 MPa falls within the range of applied stress (204 MPa – 420 MPa) that could possibly be acting on the longitudinal plies. Also, 204 MPa and 210 MPa were the stresses at which the initial tunnel crack extended into at least one individual longitudinal ply. The initial "tunnel" matrix crack had extended into all longitudinal plies (resulting in a through thickness crack) at 217 MPa and 221 MPa for Specimen 1 and Specimen 2 respectively.

The AE study performed by Morscher and Gordon reported average AE parameters of 1st and 5th loud AE events which have been known to correspond to transverse cracking in CMC materials. They reported average values of 210 ± 19 MPa and 222 ± 13 MPa for the 1st and 5th loud AE events respectively. These values compare well to the stresses at which initial cracking in the longitudinal plies was observed along with the stresses at which the initial crack extended through all eight plies of the composite.

Table 4.4: Values use for variable to compare the onset of matrix cracking in cross-ply specimens to model predictions

Material Property Variables	**Value**
E_m	360 GPa
E_f	400 GPa
E_c	371 GPa
v_m	0.72
v_f	0.28
τ_s	15 MPa
r	7.5 μm
Γ_m	36 J/m^2
υ	0.14
σ_r	63 MPa
$g\left(f, \frac{E_f}{E_m}\right)$:	1.2
t	0.22 mm

4.5 Comparison of Matrix Cracking Behavior Between Unidirectional and Cross-ply Composite Specimens

Figure 4.11 depicts a 2D slice from Specimen 1 of each type (unidirectional and cross-ply) of architecture at the applied stresses where the most damage was observed in each respective specimen. There were two distinct differences between the observations of both specimens. First, it can be seen in Figure 4.11 that the unidirectional specimen had more matrix cracks (a total of eight in this slice) within the imaged field of view compared to only two in both of the cross-ply specimens. Second, it can also be observed that the matrix crack opening is larger for the cross-ply specimens than for the unidirectional specimens. There are mechanical models that predict the relationship between the mechanical behavior of the unidirectional and cross-ply composites. This section will compare the matrix cracking behavior of the cross-ply composite to (i) predicted behavior using material properties of the composite material (ii) the behavior of the cross-ply composite in relation to the previously tested unidirectional specimens. Imaging both unidirectional and cross-ply SiC/SiC CMCs provides the opportunity to compare the damage progression between the two types of samples.

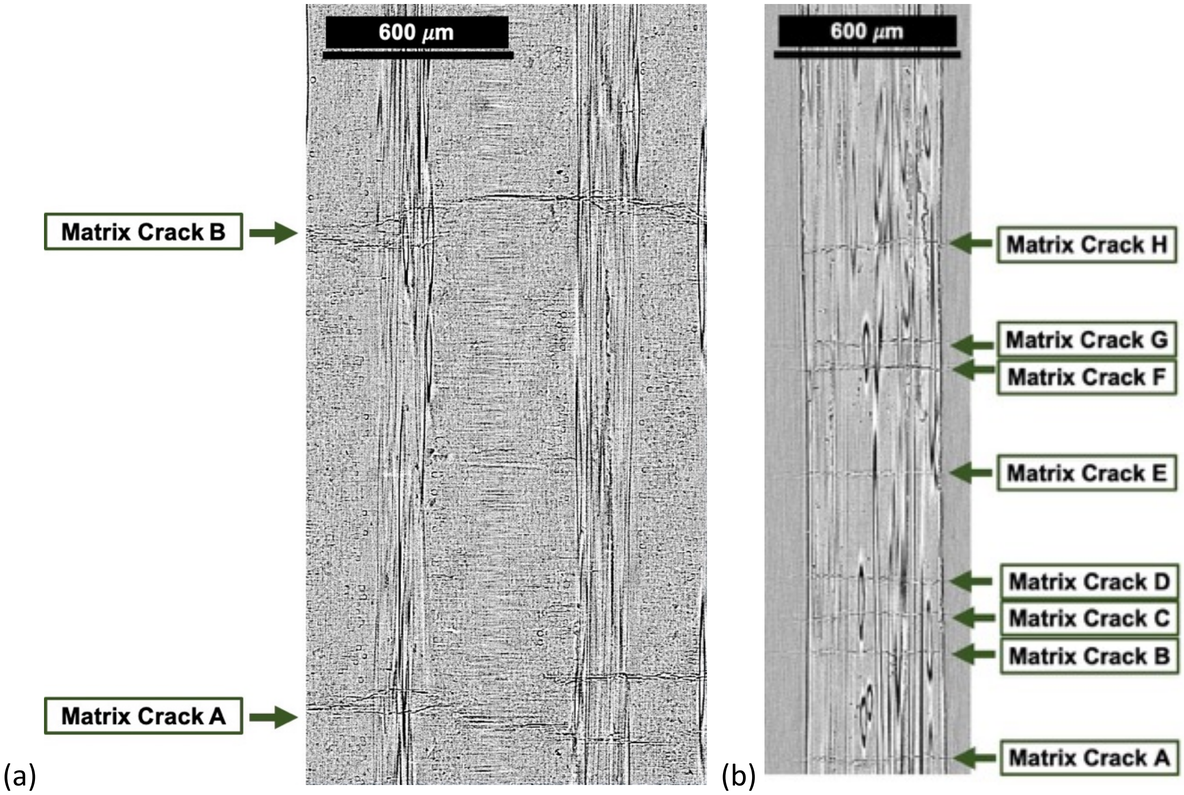

Figure 4.11 matrix cracking within (a) the cross-ply Specimen 1 at 247 MPa where there was a total of two through thickness matrix cracks observed directly before failure. The openings of the matrix crack were distinguishable looking at individual 2D slices (b) the unidirectional Specimen 1 at 550 MPa where there was a total of eight through thickness matrix cracks observed directly before failure and the openings of the matrix crack were not discernable.

The comparison between the two types of specimens results in the ultimate tensile strength, UTS, of cross-ply composites being scaled down by ½ when compared to the UTS of the unidirectional if the 0° and 90° ply widths are approximately the same width and because the 90° plies are assumed to not contribute to load bearing. The UTS of the cross-ply composite in relation to the UTS of the unidirectional composite can be estimated using Equation (4.5a) below where σ_{UTS}^{uni} is the ultimate tensile strength of the unidirectional composite, l_0 and l_{90} are the width of the 0° ply and 90° ply respectively.[11] The value for σ_{UTS}^{uni} in Equation (4.5a) can be determined through (i) material properties using Equation (4.5b), where m is the Weibull parameter (reported values of 2.5-4.5, although a Weibull modulus of 4 is used here), and S_c (3 GPa) is the fiber strength parameter, or (ii) from experimental testing of unidirectional specimens made using the same materials and process.

$$\sigma_{UTS}^{cp} = \sigma_{UTS}^{uni}\left(\frac{l_0}{l_0 + l_{90}}\right) \tag{4.5a}$$

$$\sigma_{UTS}^{uni} = fS_c\left[\frac{2}{(m+2)}\right]^{\frac{1}{(m+1)}}\left[\frac{m+1}{m+2}\right] \tag{4.5b}$$

The UTS of the cross-ply composite was first calculated using material properties and Equation (4.5b) which predicted the ultimate tensile strength of a unidirectional specimen to be 562 MPa, which then results in the UTS of the cross-ply (σ_{UTS}^{cp}) to be 281 MPa per Equation (4.5a). Since the widths of the 0° and 90° plies within the cross-ply are approximately equivalent, the predicted UTS for the cross-ply specimen is ½ of the predicted UTS for the unidirectional specimen. This scaling effect is due to the fact that the fibers in the loading direction dominate failure behavior and only 50% of the total fiber volume fraction of the cross-ply composite occur in the loading direction. The observed values of 248 MPa and 254 MPa for Specimen 1 and Specimen 2 respectively are 30-40 MPa less than the predicted value which could be due to the variation observed in the CMC microstructure

The UTS of the cross-ply composites was also compared to the experimentally observed UTS of previously tested unidirectional specimens made of the same material using Equation (4.5a) where the failure stress of the unidirectional specimens (Specimen 1 and Specimen 2) was used for (σ_{UTS}^{uni}). In situ tomography on two unidirectional composites of the same material, detailed in Chapters 2 and 3, had reported failure strengths of 480 and 610 MPa.[22] Using these observed values for unidirectional specimens results in a predicted UTS for the cross-ply specimens of between 240 MPa and 305 MPa. The ultimate tensile strengths of both cross-ply specimens fall in this range.

Table 4.5 Experimentally observed matrix cracking behavior and predicted behavior.

	Onset of matrix cracking	Extension of matrix cracking into longitudinal plies	Failure Stress (UTS)
Specimen 1	195 MPa	204-408	248 MPa
Specimen 2	210 MPa	210-420 MPa	254 MPa
Predicted	205 MPa	262 MPa	240, 305 MPa
Morscher/Gordon study	202 ± 13 MPa	Applied Stress of 210 ± 19 MPa	238 ± 15 MPa

Table 4.6 Variables used and their corresponding values.

Material Property Variables	**Values**
l_0	0.22 mm
l_{90}	0.22 mm
S_c	3 GPa
m	4

4.6 Summary/Conclusion

Micro-CT imaging of HiPerComp^{TM} SiC/SiC cross-ply CMCs under tensile load was performed and the evolution of matrix cracking was described. Most initial matrix cracks started as tunnel cracks in the 90° plies and became through cracks that spanned the entire thickness and width of the specimen although there was a partial matrix crack that was observed. The matrix crack opening couldn’t be directly measured due to limited resolution however, it was observed that the opening of the matrix crack was often slightly larger in the transverse plies when compared to the longitudinal plies which is to be expected.

The matrix cracking behavior obtained from these micro-CT experimental results were compared to well-known published mechanical models. The onset of matrix cracking in the form of tunnel cracks was detected and correlated well to predictions based on the mechanics of the composites. The process of the extension of the initial tunnel crack into the longitudinal plies was shown in detail and the relationship between the applied stress at which initial matrix cracking in the longitudinal plies occurred and the onset of matrix cracking in unidirectional specimens was examined. It is concluded that the observations are within general reasonable expectations from previously produced mechanical models[4-7]. However, due to the variability in the microstructure (i.e. variability in fiber diameter, fiber coating thickness, and non-linearity in matrix crack plane) the experimental results will vary from predictions.

The general behavior of matrix cracking in cross-ply composites is often compared to the cracking behavior seen in unidirectional composites. It was observed that the ultimate tensile strengths of the cross-ply specimens were similar to the predicated values for UTS and were also approximately 50% lower than that seen in the unidirectional composite. It was also observed that the unidirectional specimens had more matrix cracks in the field of view while under tensile load than the cross-ply composites but with much smaller crack opening consistent with models and other experimental observations. It was also noticed that in general the cross-ply composite specimen had more linear matrix cracks except in the longitudinal plies where bifurcation was often observed.

References

1. Steibel J. Ceramic matrix composites taking flight at GE Aviation. Am Ceram Soc Bull 2019;98(3):30-33.
2. Corman GS, Dean AJ, Brabetz S, Brun MK, Luthra KL, Tognarelli L, et al. Rig and engine testing of melt infiltrated ceramic composites for combustor and shroud applications. J Eng Gas Turbines Power 2002;124(3):459-464.
3. Halbig, M. C., Jaskowiak, M. H., Kiser, J. D., & Zhu, DEvaluation of ceramic matrix composite technology for aircraft turbine engine applications. 51st AIAA Aerospace Sciences Meeting including the New Horizons Forum and Aerospace Exposition 2013; 2013.
4. Marshall DB, Cox BN, Evans AG. The mechanics of matrix cracking in brittle-matrix fiber composites. Acta Metallurgica. 1985; 33(11): 2013-2021.
5. Rajan VP, Zok FW. Matrix cracking of fiber-reinforced ceramic composites in shear. J Mech Phys Solids. 2014;73:3-21.
6. Aveston J., Kelly A., J., Theory of Multiple Fracture of Fibrous Composites. J. Mater. Sci. 1973; 8: 352-362
7. Beyerle D., Spearing S., Zok F., Evans A., Damage and Failure in Unidirectional Ceramic-Matrix Composites. J. Am. Ceram. Soc. 1992; 75(10): 19-25

8. Solti JP, Mall S, Robertson DD. Modeling of fatigue in cross-ply ceramic matrix composites. J Compos Mater 1997;31(19):1921-1943
9. Evans A., Zok F., The physics and mechanics of fiber-reinforced brittle-matrix composites. J. Mater. Sci. 1994; 29: 3857–3896.
10. Sorenson B., Evans R., Analysis of Damage in a Ceramic Matrix Composite. Int. Journ. Dam. Mech. 1992; 2: 246-271
11. O'Day MP, Curtin WA, Marshall DB. Failure of crossply ceramic-matrix composites. J Am Ceram Soc 2002;85(6):1553-1560.
12. Xia ZC, Hutchinson JW, Evans AG, Budiansky B. On large scale sliding in fiber-reinforced composites. J Mech Phys Solids 1994;42(7):1139-1158.
13. Beyerle DS, Spearing SM, Evans AG. Damage Mechanisms and the Mechanical Properties of a Laminated 0/90 Ceramic/Matrix Composite. J Am Ceram Soc 1992;75(12):3321-3330.
14. Xia ZC, Carr RR, Hutchinson JW. Transverse cracking in fiber-reinforced brittle matrix, cross-ply laminates. Acta metllaurgica Et Materialia 1993;41(8):2365-2376.
15. Evans AG, Domergue J-, Vagaggini E. Methodology for Relating the Tensile Constitutive Behavior of Ceramic-Matrix Composites to Constituent Properties. J Am Ceram Soc 1994;77(6):1425-1435.
16. Budiansky B, Hutchinson J.W, Evans A.G. Matrix fracture in fiber-reinforced ceramics. Journal of the Mechanics and Physics of Solids 1986; 34(2): 167-189.
17. Budiansky B, Evans AG, Hutchinson JW. Fiber-matrix debonding effects on cracking in aligned fiber ceramic composites. Int J Solids Struct 1995; 32 (3-4): 315-328.

18. Bale HA, Haboub A, Macdowell AA, Nasiatka JR, Parkinson DY, Cox BN, et al. Real-time quantitative imaging of failure events in materials under load at temperatures above 1,600°C. Nat Mater. 2013; 12(1): 40-46.
19. Saucedo-Mora L, Lowe T, Zhao S, Lee PD, Mummery PM, Marrow TJ. In situ observation of mechanical damage within a SiC-SiC ceramic matrix composite. J Nucl Mater 2016;481:13-23.
20. Thornton J, Arhatari BD, Sesso M, Wood C, Zonneveldt M, Kim SY, et al. Failure Evaluation of a SiC/SiC Ceramic Matrix Composite during In-Situ Loading Using Micro X-ray Computed Tomography. Microsc Microanal 2019.
21. Maillet E, Singhal A, Hilmas A, Gao Y, Zhou Y, Henson G, et al. Combining in-situ synchrotron X-ray microtomography and acoustic emission to characterize damage evolution in ceramic matrix composites. J Eur Ceram Soc. 2019; 39(13):3546-3556.
22. Hilmas AM, Sevener KM, Halloran JW. Damage evolution in SiC/SiC unidirectional composites by X-ray tomography. J Am Ceram Soc. 2020; 103(5): 3436-3447
23. Hilmas A, Henson G, Singhal A, Gao Y, Schuster M. In-situ observation of damage in unidirectional CMC laminates under tension. Ceram Int. 2020; 46(9): 13502-13510
24. Wing BL, Esmonde-White F, Halloran JW. Microstress in reaction-bonded SiC from crystallization expansion of silicon. J Am Ceram Soc 2016;99(11):3705-3711.Bale AIP
25. Morscher GN, Gordon NA. Acoustic emission and electrical resistance in SiC-based laminate ceramic composites tested under tensile loading. J Eur Ceram Soc 2017; 37(13): 3861-3872.

26. Wing BL, Halloran JW. Relaxation of residual microstress in reaction bonded silicon carbide. Ceram Int 2018;44(10):11745-11750.
27. Wing BL, Halloran JW. Microstress in the matrix of a melt-infiltrated SiC/SiC ceramic matrix composite. J Am Ceram Soc 2017;100(11):5286-5294

Chapter V. Fiber Fragmentations Within Cross-ply SiC/SiC CMCs using Micro-CT Imaging and the Comparison of Damage Evolution Between Unidirectional and Cross-ply Specimens

5.1 Introduction

This chapter will continue to focus on the damage evolution in cross-ply ceramic matrix composites with a $[0°/90°]_s$ layup, symmetric around a center SiC matrix only region. Fiber fragmentations were studied and correlated to matrix cracking damage. The fiber fragmentation opening values will also be discussed. Although SiC/SiC ceramic matrix composites have been studied for decades there are very few published experimental results on the fiber fragmentation damage mechanism within CMCs. Damage observations are often made by surface microscopy techniques after polishing a specific face of the specimen and therefore it can be difficult to capture the fiber fragmentations. For this work the terms fiber fragmentation and fiber breaks can be used interchangeably. Utilizing Acoustic Emission (AE) has also provided experimental information about fiber fragmentations because the sound created by the breaking of fibers show up as high frequency, low energy AE events. Using micro-CT allows for the observation of fiber fragmentations within the volume of each specimen at increasing stress increments.

As stated previously, the specimens tested were $[0°/90°]_s$ composites and fiber fragmentations do not occur within the transverse plies because the fibers are running perpendicular to the loading direction. The fibers in the longitudinal direction respond to the applied load in a similar fashion to what was observed within the unidirectional specimen. The width of the cross-ply specimen was approximately the same size as the field of view and as a result at some of the applied stress increments, the imaging dataset was truncated and the outside two longitudinal plies were not fully captured within the field of view. Therefore, in order to keep consistency in the analysis across all data sets, only the fiber breaks within the two center-most longitudinal plies were segmented. This also allowed for comparison to the unidirectional specimens which consisted of two longitudinal plies.

An example of multiple fiber fragmentations and their segmentation can be seen in Figure 5.1. Every fiber break was segmented using black/grey scale and was then viewed manually to ensure that only fiber breaks were segmented. Due to the BN fiber coating have a low x-ray attenuation, it also showed up dark and therefor would occasionally be segmented along with the fiber breaks. However due to the low x-ray density of the BN coating on the fibers, the pixels in the data set that were part of the coating were often segmented as fiber breaks.

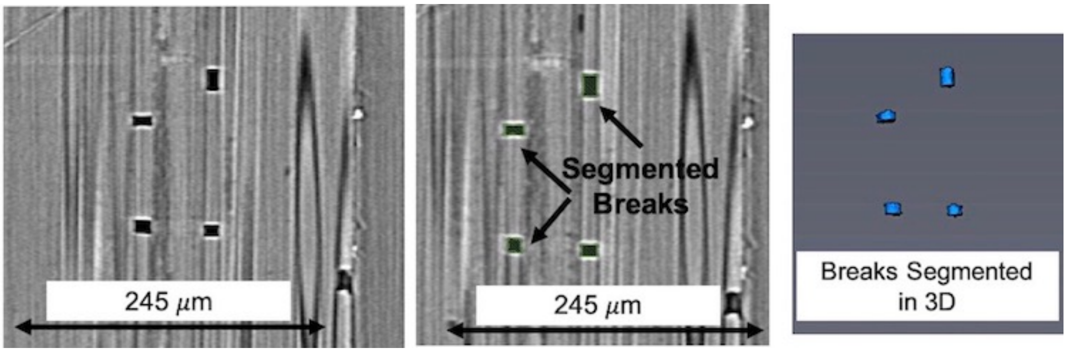

Figure 5.1 The image on the left is a slice within the volume of Specimen 1 where four fiber breaks can be seen. In the middle image the fiber breaks are selected (represented by the green highlight) and the last image on the right shows the segmentation of the breaks where the x,y,z centroid of the breaks was determined.

5.2 Fiber Fragmentation Observations

Segmenting the fiber fragmentations allowed for the centroid of each fragmentation to be identified. giving an X,Y,Z location for each individual fiber fragmentation. Figures 5.2a and 5.2b depict the location of each fiber break within each of the two center plies in the volume of Specimen 1 at 212 MPa and 246 MPa. For perspective, the width of each ply was approximately 200 μm. At 212 MPa there were fewer fiber fragmentations detected with only 260 fiber fragmentations observed within the entire volume of the specimen. It can also be seen in Figure 5.2a that initially there were slightly more fiber fragmentations within Ply 1 than Ply 2 (the plies are depicted by labels within Figure 5.2) . The fiber fragmentations appear to be evenly distributed in Ply 1 meanwhile there is a region near the front center portion of Ply 2 where no fiber fragmentations were detected in Ply 2 at 212 MPa. By 246 MPa, shown in Figure 5.2b, the measured fiber fragmentations filled almost the entire height and thickness of the imaged ply volumes. It did appear that certain regions within each ply had more fiber breaks than others due to the correlation of fiber fragmentations to matrix crack positions.

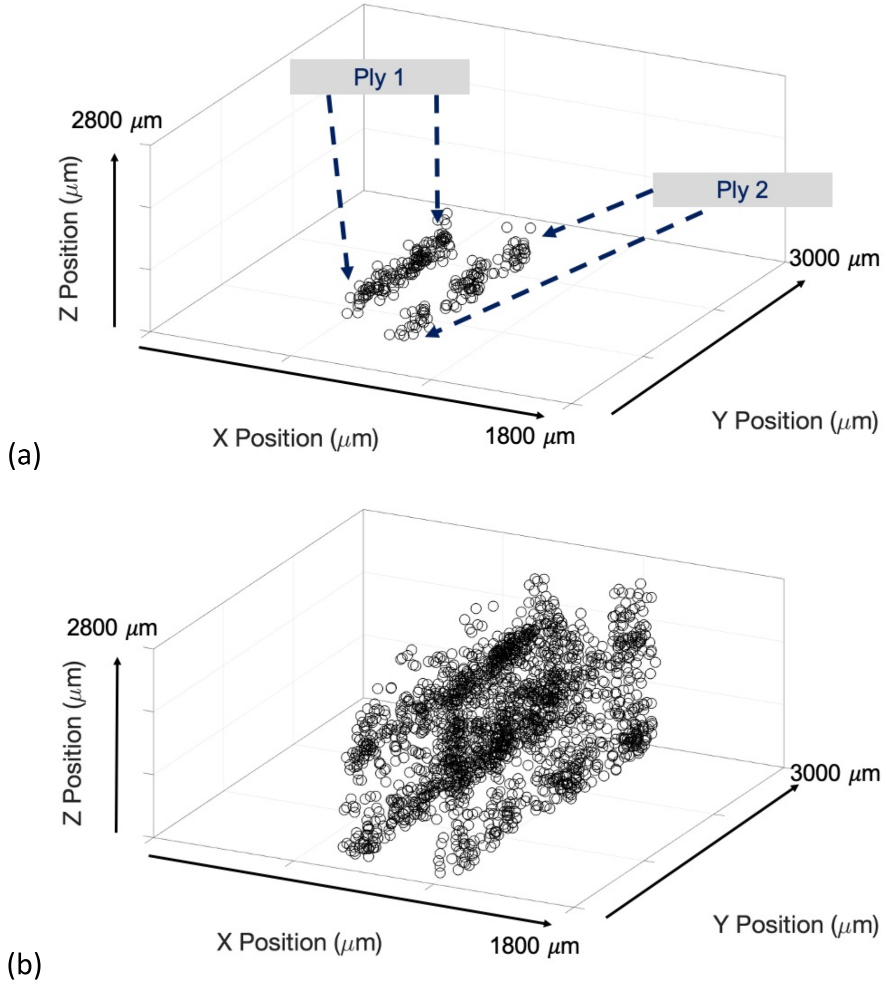

Figure 5.2 (a) the 3D location of approximately 260 breaks measured within the volume of Specimen 1 at 212 MPa (b) the 3D location of approximately 2075 breaks measured within the volume of Specimen 1 at 246 MPa

The location of fiber fragmentations within the volume of Specimen 2 at applied stresses of 217 MPa and 246 MPa are shown in Figures 5.3a and 5.3b respectively. At 217 MPa, there are 125 detected fiber fragmentations observed within the volume and it appears that more fiber breaks occurred near the front and back ends (Y Position direction) of the specimen compared to the regions within the center of the volume similar to Ply 2 in Figure 5.2a. In Figure 5.3b it can be observed that there are regions along the z-direction where there are larger number of fiber fragmentations. These correlate to the locations of the observed matrix cracks in Specimen 2. When comparing the fiber fragmentation locations within each Specimen, one noticeable difference between the two was the distribution of fiber fragmentations in the Z-direction. For Specimen 1, by 246 MPa, fiber fragmentations were detected along the entire Z-axis (height) of the specimen, 2.8 mm. However, in Specimen 2, the distribution of fiber breaks doesn't quite fill the height of the field of view (2800 μm) but rather the location of the highest detected fiber fragmentation was at 2100 μm along the length of Specimen 2.

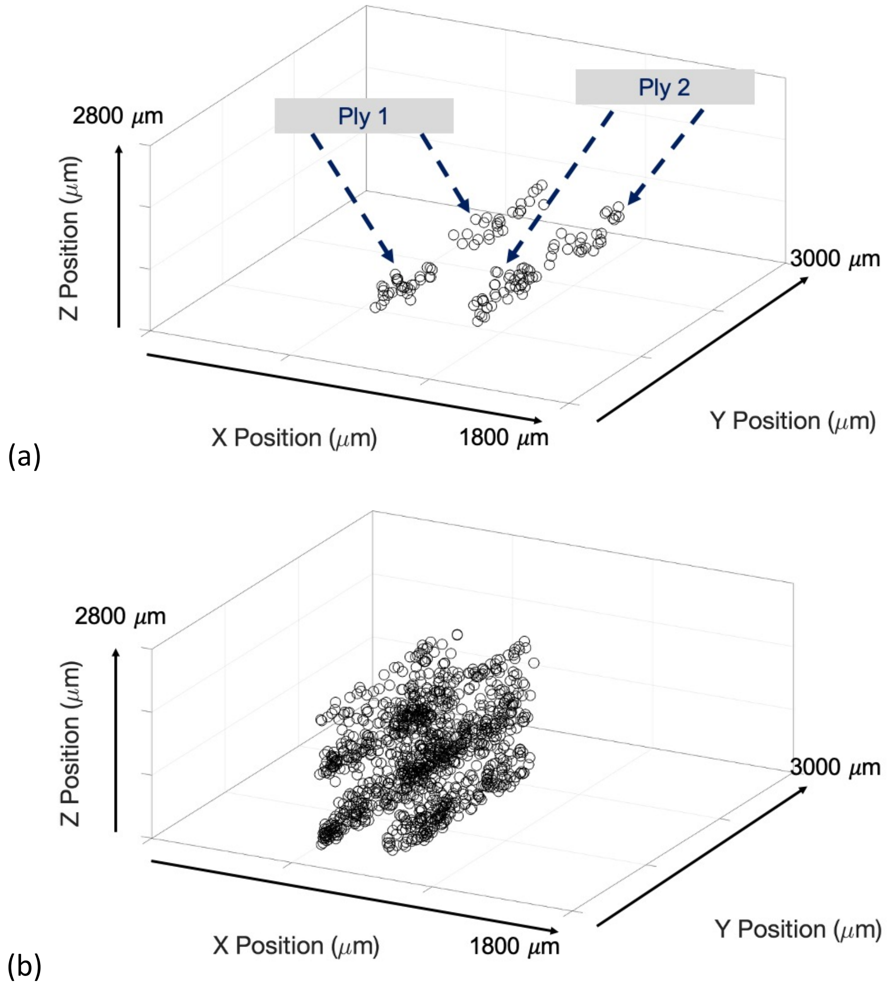

Figure 5.3 (a) the 3D location of approximately 125 breaks measured within the volume of Specimen 2 at 217 MPa (b) the 3D location of approximately 1140 breaks measured within the volume of Specimen 2 at 246 MPa

The total number of fiber fragmentations segmented at each increasing stress increment for each specimen is plotted in Figure 5.4a. Both specimens experienced an increase in the total number of fiber fragmentations detected at each increasing applied stress increment. When looking at the observed increase in fiber fragmentations between 212 MPa and 246 MPa in Specimen 1, the number of fiber fragmentations increased by a little over eight times the original number of initially segmented fiber breaks. The number of fiber fragmentations detected in Specimen 2 had an increase of approximately nine times when comparing the number of fiber fragmentations detected initially 216 MPa to the number of fragmentations at 246 MPa in Specimen 2. The increase in fiber fragmentations observed for both specimens results in similar trends for each specimen shown in Figure 5.4a. However, when directly comparing Specimen 1 and Specimen 2, Specimen 2 contained only half the total number of fiber fragmentations that were detected in Specimen 1 at comparable applied stresses. Although Specimen 2 experienced less damage (observed within the field of view) than Specimen 1, the two specimens failed at stresses of 248 MPa and 254 MPa for Specimen 1 and Specimen 2 respectively. Given the uncertainty in stress values it is assumed that the two tested specimens failed at approximately the same stress. However, each imaged stress increment is identified by their calculated stress increment so they will be continued to be labelled by 248 and 254 MPa respectively. The failure crack and in turn the fracture surface itself, was not imaged but rather the final failure occurred approximately 5 mm below the bottom of the scanned volume for Specimen 1 and even further away from the imaged field of view for Specimen 2.

In order to better understand the uniformity of damage evolution, the number of fiber fragmentations detected in each individual ply for each stress increment for Specimen 1 and

Specimen 2 is shown in Figure 5.4b. The number of fiber fragmentations within each ply are relatively similar for both specimens although it was observed in Specimen 1 that Ply 1 consistently had a slightly larger number of fiber fragmentations when compared to Ply 2. The difference however is within the range of 100 fiber fragmentations and compared to the 1600 fibers that make up an individual ply, the difference in the detected fiber fragmentations is minimal (6% of total fibers within an individual ply). The fiber fragmentations detected in Specimen 2 appeared to be relatively uniform between the two plies. The segmentation of fiber of individual fiber breaks was performed manually using grey scale and as a result, the number of fiber breaks have very little uncertainty while the fiber fragmentation opening does involve uncertainty due to the variation in the grey scale used for each individual fiber fragmentation.

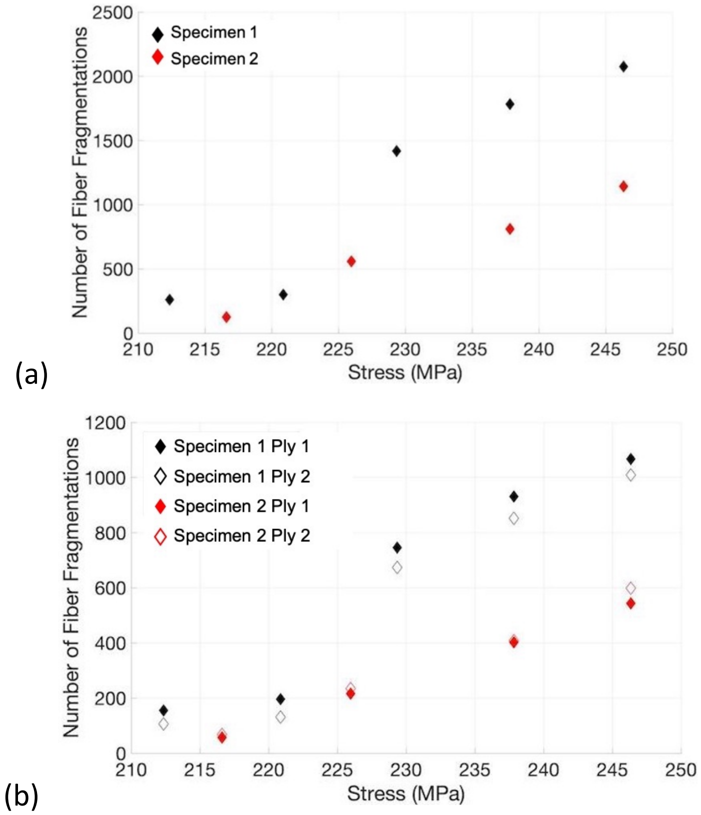

Figure 5.4 (a) the number of fiber fragmentations detected at each stress increment for each specimen (b) the number of fiber fragmentations detected within each ply (labelled as Ply 1 and Ply 2) at each stress increment of each specimen

5.3 Correlating Observed Matrix Cracks and Fiber Fragmentations

As with the unidirectional specimens, the two main types of damage that occur within cross-ply composites are matrix cracking and fiber fragmentation. The matrix cracking observations were discussed in detail in Chapter 4. In this section, fiber fragmentation location and evolution are correlated to the matrix crack observations.

In order to visually correlate the location of the detected fiber fragmentations to the location of each matrix crack, the location of both types of damage were plotted onto a 2D-plane (XZ Plane) as shown for Specimen 1 in Figures 5.5a and 5.5b at 212 MPa and 246 MPa respectively. Fiber fragmentations only occur in longitudinal plies and to be consistent between every specimen, only the fiber fragmentations within the center two longitudinal plies were segmented as depicted in Figure 5.5a and 5.5b. At 212 MPa, the fiber fragmentations detected within the X-Z plane of Specimen 1, are predominantly located near Crack A; although there were fiber fragmentations detected up to 650 µm away from the measured average location for Crack A. By 246 MPa there were fiber fragmentations measured along the entire length (Z-axis) of the field of view of Specimen 1 and it is apparent from Figure 5.5b that the fiber fragmentations were not uniformly distributed along the length of the specimen but rather were more dense near each matrix crack, with fewer fiber fragmentations detected in the center of the specimen between Crack A and Crack B. This behavior is comparable to that of the unidirectional Specimen 1.

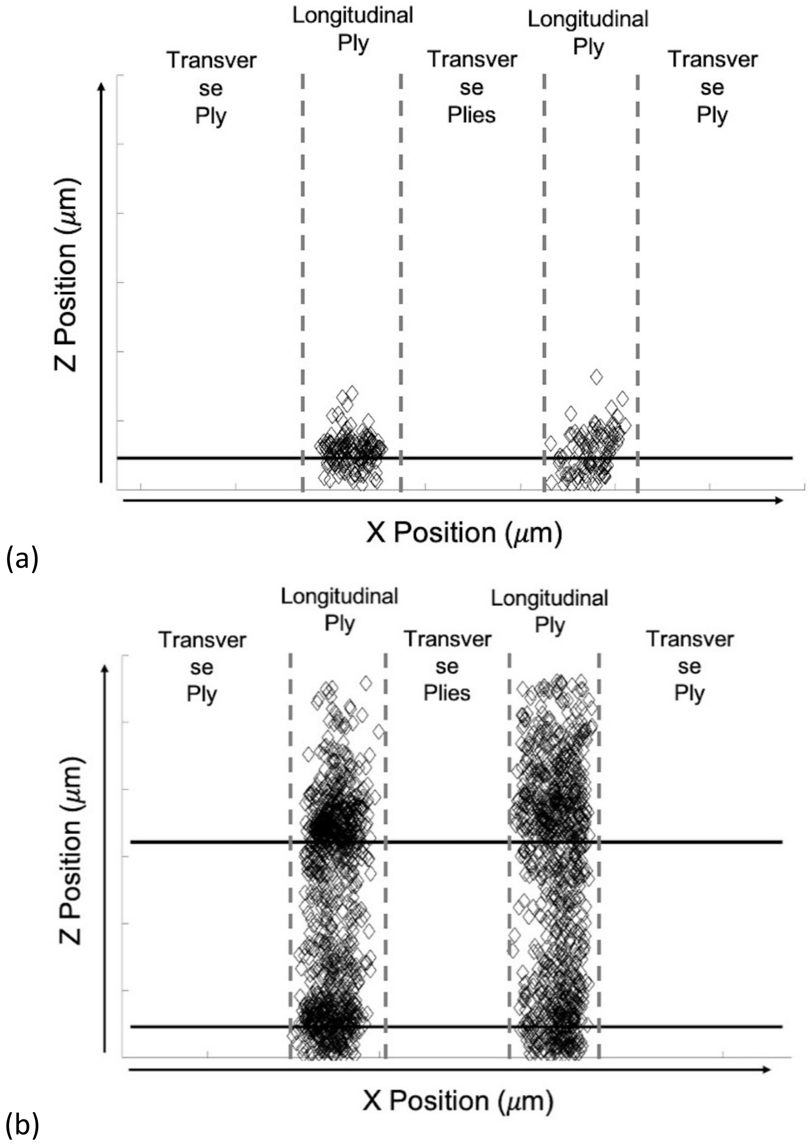

Figure 5.5 (a) the position of fiber breaks (open diamonds) and matrix cracks (black lines) within the field of view of Specimen 1 at 212 MPa (b) the position of fiber breaks (open diamonds) and matrix cracks (black lines) within the field of view of Specimen 1 at 246 MPa

The relationship between the location of fiber fragmentations and the location of each matrix crack in Specimen 2 is depicted Figures 5.6a and 5.6b at 217 MPa and 246 MPa respectively. When comparing the damage detected in Specimen 1 and Specimen 2 at 246 MPa (Figures 5.5b and 5.6b) it is readily observed that Specimen 1 higher amounts of fiber fragmentations, while both specimens exhibit higher fiber fragmentation density in the vicinity of matrix cracks.

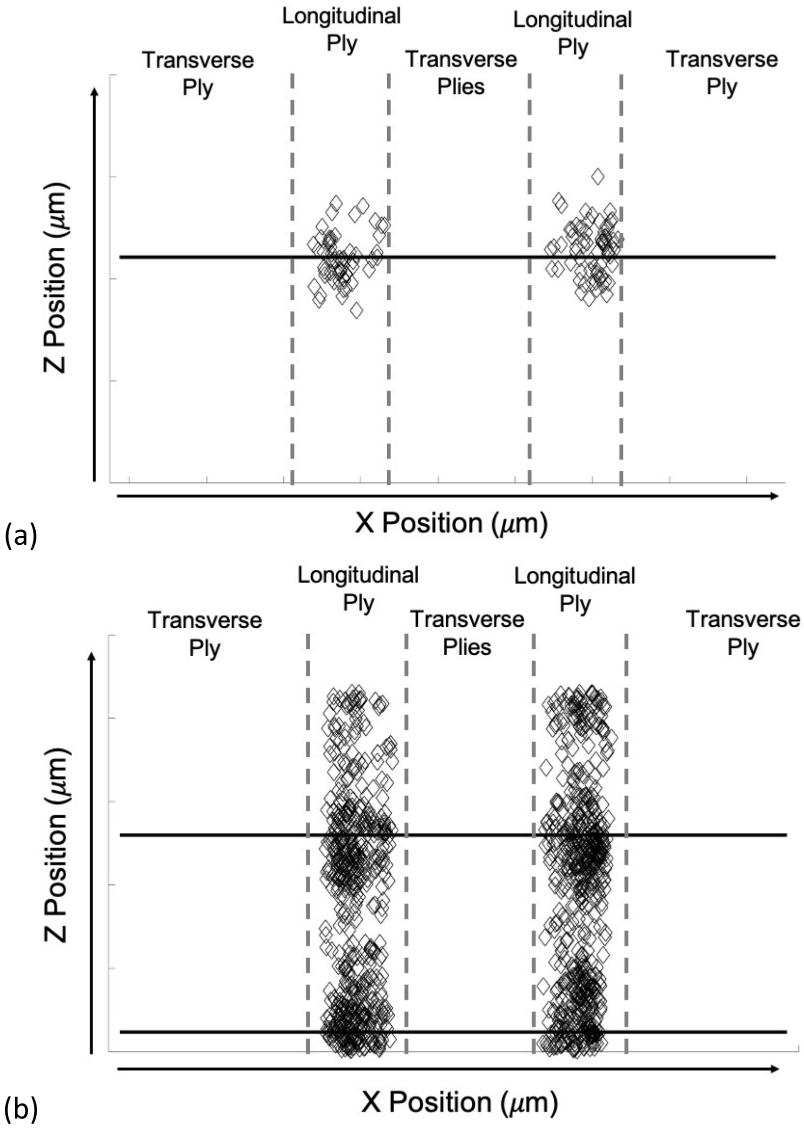

Figure 5.6 (a) the position of fiber breaks (open diamonds) and matrix cracks (black lines) within the field of view of Specimen 2 at 217 MPa (b) the position of fiber breaks (open diamonds) and matrix cracks (black lines) within the field of view of Specimen 2 at 246 MPa

Another way to look at the comparison between the location of fiber breaks and the location of matrix cracks is to quantify damage along the length (or z-axis) of the specimen at each stress increment similarly to what was done with the undirectional specimens is depicted in Figure 5.7a-e. The number of fiber fragmentations detected within 100 μm increments along the length of each specimen (within both center plies) were determined and plotted for Specimen 1 and Specimen 2 in Figures 5.7a-e and 5.8a-d respectively. The black vertical lines represent the location of each matrix crack along the length of the specimen. In Figures 5.7a and 5.7b, the number of fiber breaks were measured along the length (z-axis) of the specimen (i.e. the number of breaks that occurred between 0-100 µm, 100-200 µm, etc. along the length of the specimen). For Specimen 1, fiber breaks were first visually detected at 212 MPa after Crack A had initiated (but had not yet traversed through all eight plies) and before Crack B was detected (Figure 5.7a). By 229 MPa shown in Figure 5.7c, the second matrix crack, Crack B, had occurred within the field of view and there was a large increase in the number of fiber breaks that occurred around this Crack B; so much so that there was a larger number of fiber fragmentations associated with Crack B at 229 MPa than there were associated with Crack A. As stress was increased from 229 MPa to 238 MPa, the trend and number of fiber breaks at each length increment only increased slightly as shown in Figure 5.7d. At the highest imaged stress increment before failure of 246 MPa (Figure 5.7e) there still wasn’t a significant change in the number of fiber fragmentations detected. The crack that caused failure occurred outside the field of view and therefor was not imaged, so a large increase in fiber fragmentation number may not be expected with the field of view.

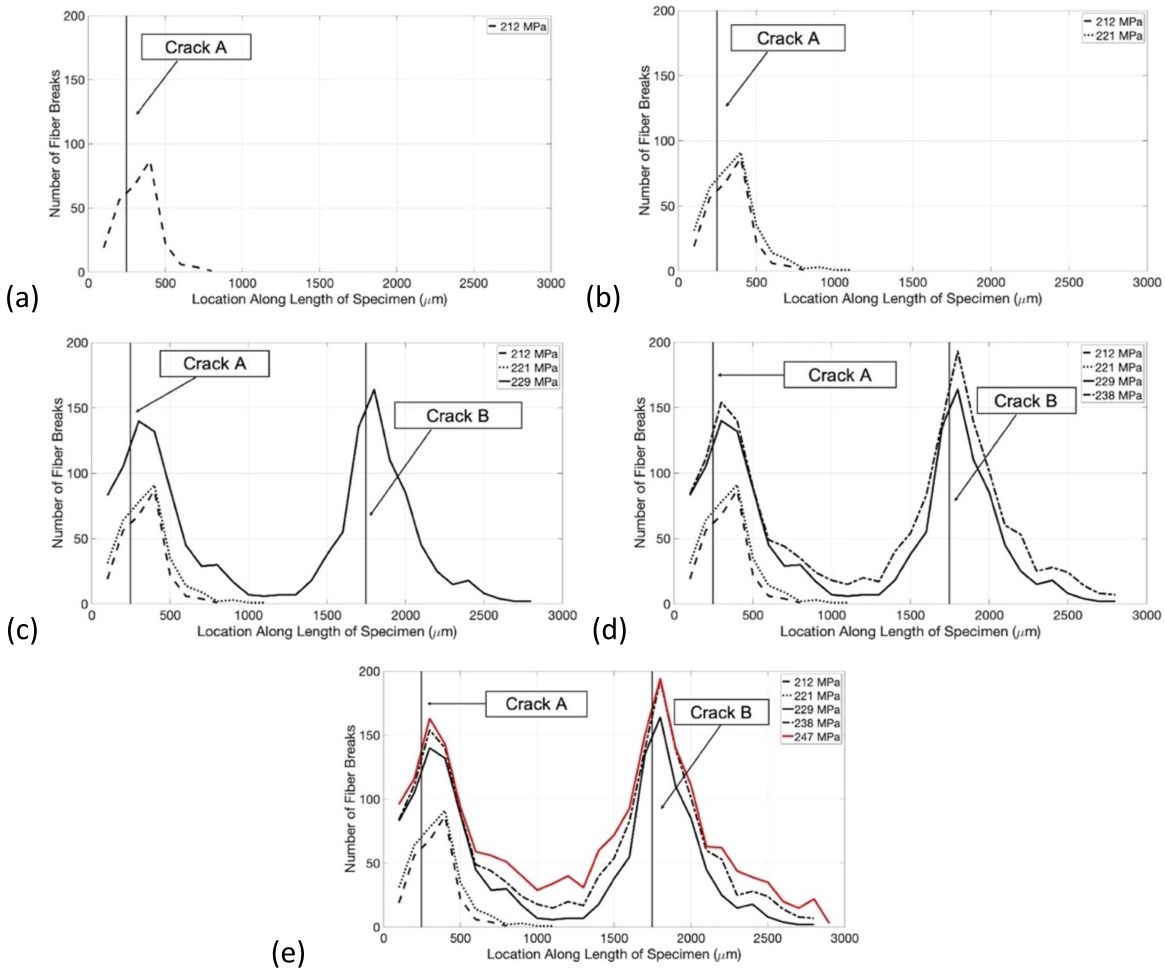

(a) (b) (c) (d) (e)

Figure 5.7 the number of fiber fragmentations that occurred within 100 *μm* increments along the length of Specimen 1 for each increasing stress increment of (a) 212 MPa (b) 212 MPa and 221 MPa (c) 212 MPa, 221 MPa and 229 MPa (d) 212 MPa, 221 MPa, 229 MPa, and 238 MPa (e) 212 MPa, 221 MPa, 229 MPa, 238 MPa, and 246 MPa (directly before failure)

The number of fiber fragmentations detected along the Z-axis of Specimen 2 at increasing stress increments is shown in Figure 5.8a-d. Fiber fragmentations were first detected at the applied stress increment of 217 MPa where less than 100 fiber fragmentations were detected all within 100 μm of Crack A shown in Figure 5.8a. By the next stress increment of 226 MPa, shown in Figure 5.8b, the number of fiber fragmentations that were located near matrix crack A approximately doubled. Also by 226 MPa, the second matrix crack, Crack B, was detected along with corresponding fiber fragmentations adjacent to that matrix crack. In Figure 5.8c, at 238 MPa, the number of fiber fragmentations that were detected near Crack B increased to a value similar to the number of fragmentations detected near matrix crack A. As with Specimen 1, this specimen also failed outside of the imaged field of view and therefore the failure crack wasn't detected. From what was imaged within the field of view it was observed form Figure 5.8d that the number of fiber fragmentations increased at the highest applied stress of 245 MPa, directly before failure, and that at a location slightly above 2000 µm, there was a slight increase in the number of fiber fragmentations in that region indicating that another damage region occurred.

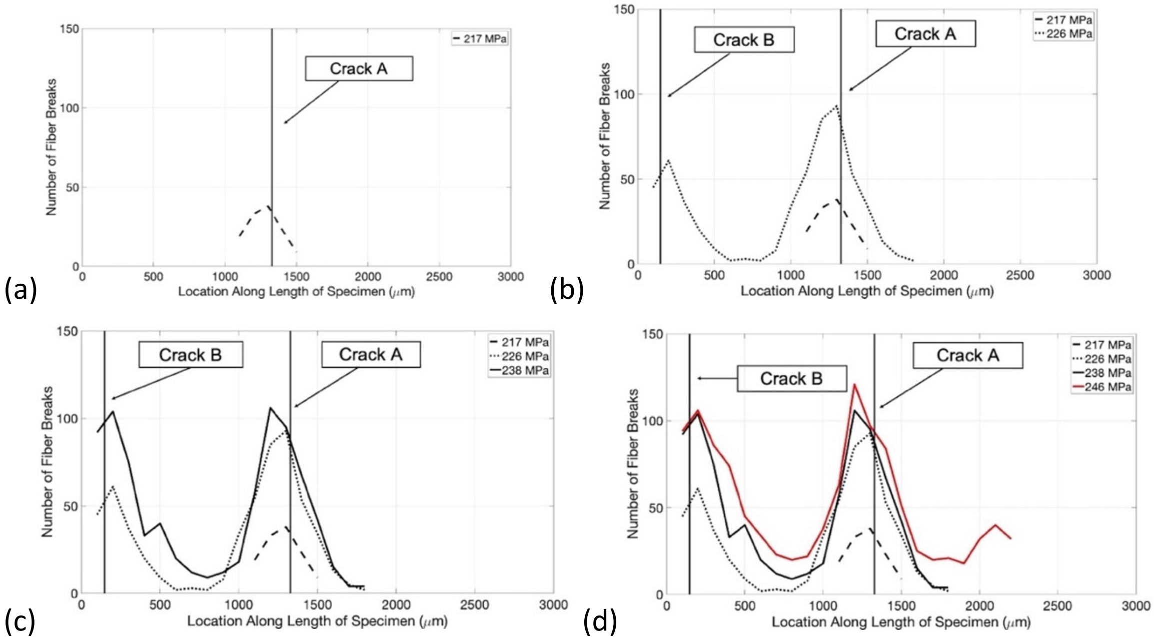

Figure 5.8 the number of fiber fragmentations that occurred within 100 μm increments along the length of Specimen 2 for each increasing stress increment of (a) 217 MPa (b) 217 MPa and 226 MPa (c) 217 MPa, 226 MPa and 238 MPa (d) 217 MPa, 226 MPa, 238 MPa, and 246 MPa

Knowing where fiber fragmentations occur relative to a matrix crack can be used to better understand the stress state of the composite once damage occurs. In order to try to obtain more quantified data about the fiber fragmentations, each measured fiber fragmentation was "binned" or designated to a specific matrix crack, in this case it was either sorted as part of Crack A or Crack B. For instance, the distance between the two matrix cracks in Specimen 1 was ~ 1200 µm. Fiber fragmentations were binned to the closest crack, i.e. the crack (A or B) less than half the crack separation distance (~ 600 µm) away This is the same process that was used for "binning" fiber fragmentations detected in the unidirectional specimens in Chapter 3.

Figures 5.9a and Figure 5.9b show the cumulative percent of fiber breaks that occur at increasing distances away from Crack A and Crack B within Specimen 1 respectively. For the fragmentations corresponding to Crack A, Figure 5.9a shows that at lower stresses of 212 and 221 MPa, 80% of the measured fiber fragmentations were located at a distance less than or equal to 200 µm. As the applied stress continued to increase, the number of fiber fragmentations increased, and the location of these fragmentations often occurred at larger distances away from the crack plane. By the highest stress increment of 246 MPa, a large number of new fiber fragmentations occurred near Crack A which resulted in 80% of the total number of fiber fragmentations detected at 246 MPa, occurring at a distance less than or equal to approximately 200 µm away from Crack A. This behavior is similar to what was observed in the unidirectional specimen although the distance of fiber fragmentations in the unidirectional specimen was dominated by the matrix crack spacing (which was slightly less than 200 µm)

The fiber fragmentation behavior for the breaks observed in relation to Crack B is unique compared to the behavior observed in Crack A and in relation to both of the observed matrix cracks detected in Specimen 2. There was only a slight change in the fiber fragmentation distance with an increase in stresses and it can be seen in figure 5.9b that 80% of the fiber fragmentations occurred at a distance less than or equal to approximately 500 µm which is approximately 300 μm greater than what was observed for the fiber fragmentations related to Crack A. It is likely that the fiber fragmentations near the top of the field of view that were binned and correlated to Crack B were actually corresponding to a matrix crack outside the field of view. If this is true this means many of the large number fiber fragmentations that occurred at 400-600 μm away from the matrix crack plane of Crack B could actually correspond to a different matrix crack. As a result, the distribution of fiber fragmentations corresponding to Crack B would completely change and the distances of the fiber fractures would occur closer to the matrix crack plane. Post-fracture analysis, beyond the field of view of the present study, would be needed to determine if this is true.

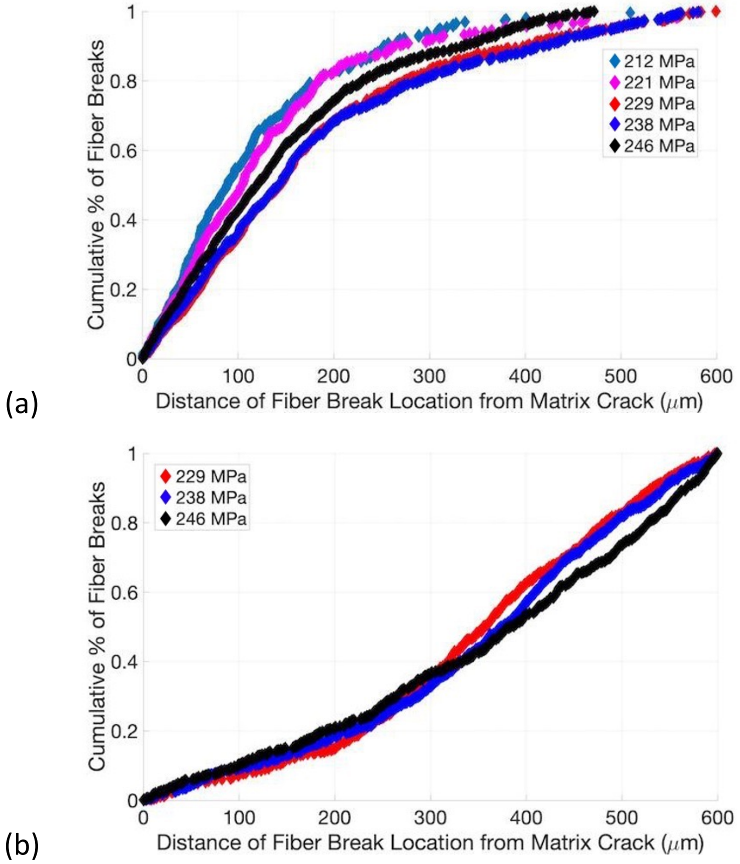

Figure 5.9 (a) Cumulative fraction of fiber breaks as a function of their distance away from Crack A in Specimen 1 (b) Cumulative fraction of fiber breaks as a function of their distance away from Crack B in Specimen 1

The cumulative fraction of fiber fragmentations in relation to their distance from the first and second matrix cracks (Crack A and Crack B) in Specimen 2 is represented by Figure 5.10a and Figure 5.10b respectively. When comparing the behavior observed in Specimen 2 to that observed in Specimen 1, the distance of fiber break location distinctly increased with increasing composite stress compared to Specimen 1 where there was only a slight difference in distance. For the fiber fragmentations detected in Specimen 2 in relation to Crack A, at 217 MPa, 80% of the fragmentations were detected at distance less than or equal to 150 µm. However, as stress was increased this distance continued to increase and by 246 MPa, 80% of the fiber fragmentations occurred at a distance of 300 µm. The behavior observed for the fragmentations observed in relation to Crack B in Specimen 2 is similar to that observed for Crack A as shown in Figure 5.10b. Another thing to note is that there were fewer fiber fragmentations detected in Specimen 2 compared to Specimen 1 as previously discussed. The statistical variation in distance between fiber fragmentations and the matrix crack plane is due to the large number of fiber fragmentations. If the fibers only break within the debond length, then a distribution of break-crack distances should reflect the statistics in the spatial distribution of strength-limiting flaws within the fibers at that stress. It is possible that these fiber breaks distance distributions could be a statistical distribution for the debond length along different fibers. The variability in debond lengths could be attributed to variability in fiber diameters and fiber coating thickness which would affect the debond lengths.

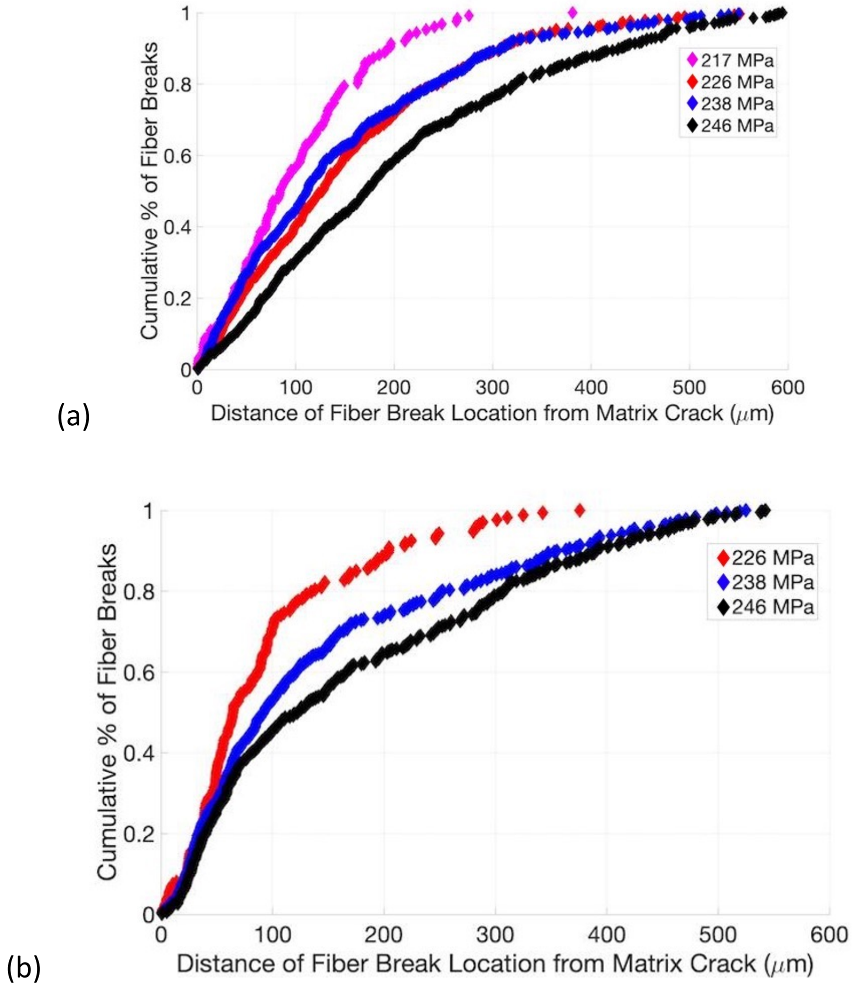

Figure 5.10 (a) Cumulative fraction of fiber breaks as a function of their distance away from Crack A in Specimen 2 (b) Cumulative fraction of fiber breaks as a function of their distance away from Crack B in Specimen 2

5.4 Fiber Fragmentation Opening Measurements

The height, or opening, of each fiber fragmentation was measured using the volume obtained from segmentation techniques. Knowing the volume of a cylindrical fiber and using a radius of 7.5 μm, the average fiber radius for Hi-Nicalon Type S fibers, the height of each fiber fragmentation was determined. The average fiber fragmentation opening for each specimen at each increasing stress increment is presented in Figure 5.11. At the lower applied stresses (210-228 MPa) the average fiber fragmentation opening was between 1-2 μm for both specimens, although the resolution was 1.3 μm/voxel therefore these opening values are near the resolution limit. The measured fiber break opening increased as applied stress increased for both specimens however the openings in Specimen 1 increased more on average than those in Specimen 2. For Specimen 1, the average fiber fragmentation opening tripled from approximately 2 μm to 6 μm. Whereas the average fiber fragmentation opening for Specimen 2 approximately doubled from 1.5 μm to 2.8 μm. It is interesting that the two specimens have large differences in their damage evolution, with Specimen 2 having both fewer number of detected fiber fragmentations and less of an increase in the fiber fragmentation openings but yet both Specimen 1 and Specimen 2 had relatively similar UTS (ultimate tensile strength) of approximately 250 MPa for both specimens. The results for fiber break opening in Specimen 1 are similar to the ones presented for unidirectional CMC specimens. However, as with the fiber fragmentation locations, there are so many fiber fragmentations that the average can be deceptive and therefore it is important to also examine the distribution of fiber break opening values.

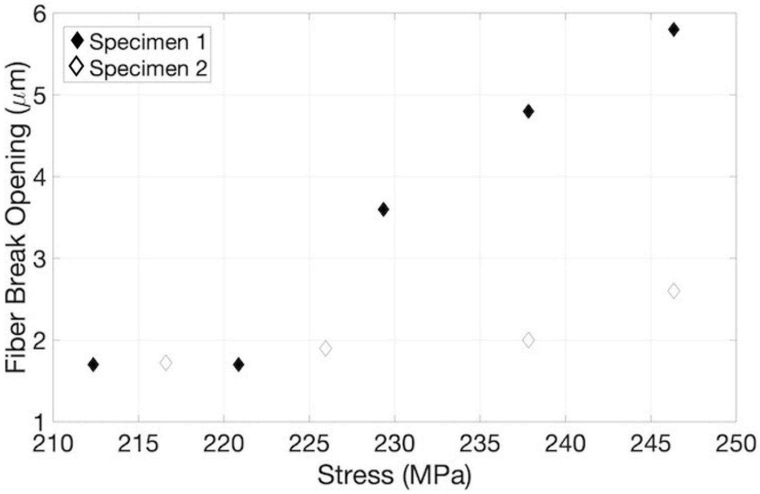

Figure 5.11 Fiber break opening values for both of the cross-ply specimens as a function of applied stress.

Since there were over 2000 fiber fragmentations detected at higher applied stresses and each fragmentation had a different opening value, the distributions of fiber break opening values for Specimen 1 and Specimen 2 are shown in Figures 5.12a and 5.12b. The 25th and 80th percentile of each distribution at increasing stress increments is also plotted for both specimens as a function of applied stress.

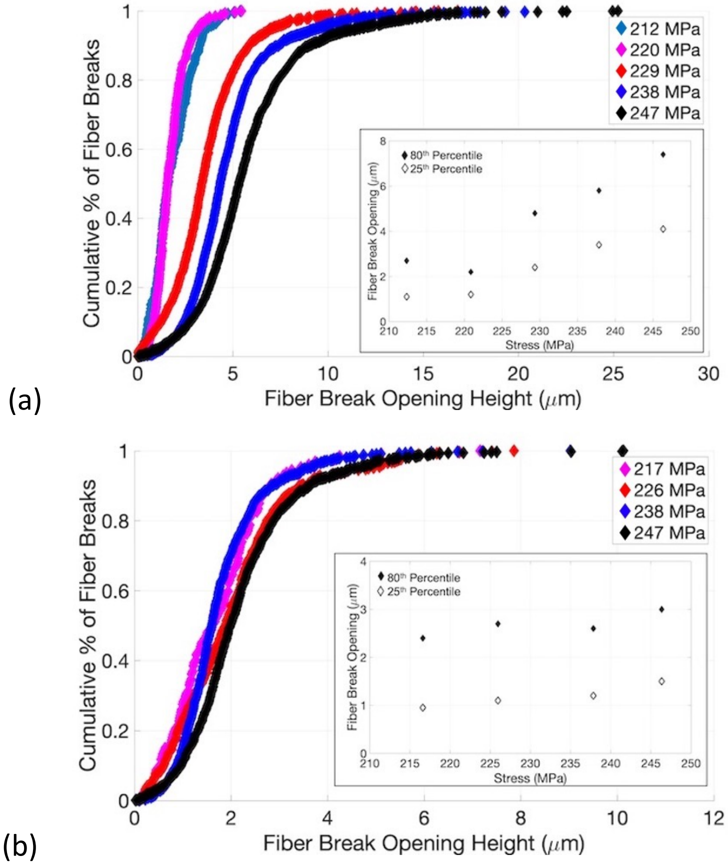

Figure 5.12 (a) Fiber break opening distribution at each stress increment for Specimen 1 with the smaller graph representing the 25th and 80th percentile of fiber break opening at each stress increment (b) Fiber break opening distribution at each stress increment for Specimen 2 with the smaller graph representing the 25th and 80th percentile of fiber break opening at each stress increment.

For Specimen 1, the measured opening of the fiber fragmentations continued to increase with applied stress. Initially at 212 MPa, 80% of the measured fiber fragmentations had an opening of at least 2.5 µm and by 246 MPa, the 80th percentile had increased to almost 8 µm. For Specimen 2 it was observed in Figure 5.12b for the average fiber break openings measured, were far less than the openings measured in Specimen 1 and the distribution plot in Figure 5.12b is comparable. The 80th percentile only slightly increased from 2.5 µm at 217 MPa to 3 µm at 246 MPa which was a great deal smaller than the openings measured at 246 MPa for specimen 1. Although the fiber fragmentations measured in Specimen 2 had smaller opening values, when comparing the fiber fragmentations at each stress increment it was observed that the fiber fragmentations continue to increase albeit in much smaller increments as seen from Figure 5.12b. The largest fiber fragmentation measured at 217 MPa was approximately 4 µm while the largest measured fiber fragmentation at 246 MPa was approximately 10 µm. As with the unidirectional specimens, it was observed that the opening or height of fiber fragmentations increased with stress as the fiber continued to slide along the debond length. It was also observed that for fiber breaks that occurred at higher applied stresses, the fiber break opening value was larger than that of a break that was detected at a lower initial applied stress. This observation is also consistent with behavior observed in the unidirectional materials.

5.4.1 Fiber Break Opening in Comparison to Matrix Crack Opening Displacement

The fiber break opening is often compared to the opening of the matrix crack, also known as the crack opening displacement (COD), as it is often extremely difficult to measure matrix crack opening displacement. In Chapter 2 it was shown that this assumption isn't necessarily true for unidirectional specimens where the fiber fragmentation openings themselves are varied and many of the observed fragmentations had openings that were three-four times larger than the matrix crack opening. However, the matrix crack opening detected within the cross-ply specimens was larger than that in the unidirectional specimens and as a result the fiber fragmentations that occurred seemed to be within the range of the crack opening displacement. The matrix crack opening was still too small to be accurately measured but Figures 5.13a-c depict fiber fragmentations observed near a matrix crack at 246 MPa in Specimen 1. In Figures 5.13a and 5.13b it can be seen that the fiber break opening is similar to the matrix crack opening. However, in Figure 5.13c it can be observed the fiber fragmentation is larger than the matrix crack opening. One major difference between Figure 5.13a/5.13b and Figure 5.13c is that in the first two images there is only one detected matrix crack in the ply whereas in Figure 5.13c the matrix crack is bifurcated through the ply and each bifurcation has a smaller opening. Although the observed matrix cracks were larger in the cross-ply specimen, the opening was still on the order or resolution and definitive quantitative value could not be determined.

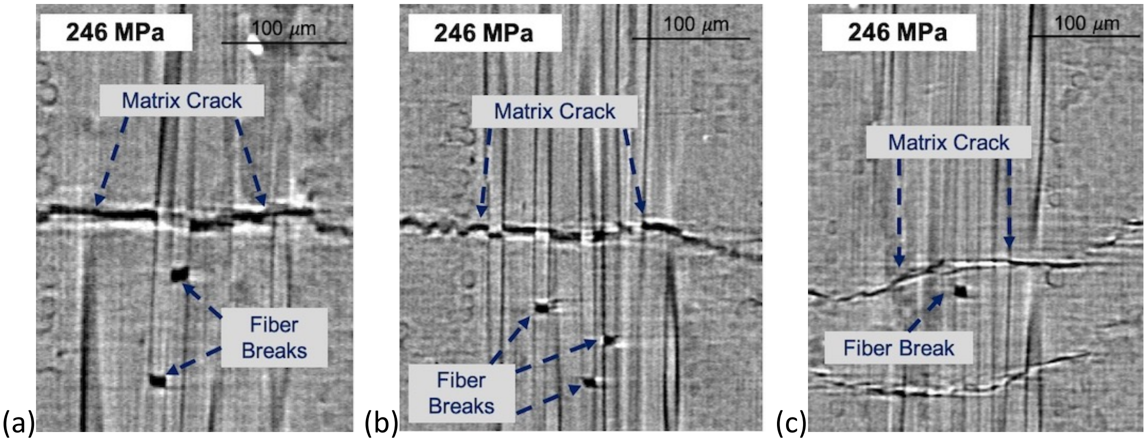

Figure 5.13 images of fiber fragmentation openings in comparison to matrix crack opening at various locations within cross-ply Specimen 1 at 246 MPa where it can be seen that (a) the fiber break opening looks comparable to matrix crack opening (b) the fiber break openings are once again comparable to the matrix crack opening and both the first two images are for linear matrix crack through the longitudinal ply whereas (c) depicts a bifurcation in the matrix crack which seems

to result in a smaller matrix crack opening which causes the fiber break opening height to be greater than the matrix crack opening.

5.5 Comparing Damage Measurements and Mechanisms Between the Unidirectional and Cross-ply Specimens[4]

It has been briefly stated throughout this body of work that acoustic emission was performed on these materials in conjunction with the micro-CT imaging. Using AE allowed for real-time information about the damage accumulation within the composite specimen in order to image an area within the specimen with known damage. Also, since AE events are not visual observations, though spatial positions of AE events can be estimated, it is useful to compare the damage observations using micro-CT with AE. This section will focus on relationships between the two major types of damage, matrix cracking and fiber fragmentations, and AE at a global level (number of AE events and cumulative AE energy). The results for both a unidirectional specimen and a cross-ply specimen will be described. Detailed information about the AE set-up can be found in the published manuscript.

5.5.1 Damage Detection Using Acoustic Emission

For these materials, matrix cracking is often represented by high energy, low frequency events while fiber fragmentations often produce low energy, high frequency events. Matrix crack lengths were measured at five locations in each ply and the surface area of each matrix crack was determined based on ply-level crack length measurements. For a crack in a transverse ply, crack

---

[4] This section is taken from manuscript published in the Journal of European Ceramic Society with permission from the corresponding authors: Maillet E, Singhal A, Hilmas A, Gao Y, Zhou Y, Henson G, et al. Combining in-situ synchrotron X-ray microtomography and acoustic emission to characterize damage evolution in ceramic matrix composites. J Eur Ceram Soc. 2019; 39(13):3546-3556.

area was calculated by multiplying average crack length within the ply by ply thickness. In a longitudinal ply, the matrix represents about 60% of any cross section, the other 40% being occupied by fibers and coatings. The area fraction of matrix can vary between samples but over a limited range. Therefore, variability in matrix area fraction was neglected. Crack area was considered as 60% of the average crack length within the ply multiplied by ply thickness. The fiber fragmentations that were discussed in previous sections are also compared to acoustic emission events.

5.5.2 AE Measurements for Unidirectional Specimen

The damage detected by AE was compared to the damage quantified using x-ray tomography. The overview of damage in Specimen 1 is shown in Figure 5.14 where the total matrix crack area and the number of fiber fragmentations at each stress increment is indicated. The total matrix crack area and the total number of fiber breaks detected at each stress increment for specimen 1 is depicted in Figure 5.14. The total matrix crack area increased to 7 mm^2 , and the number of fiber breaks increased to 1600 breaks by 550 MPa as previously discussed in Section 5.2

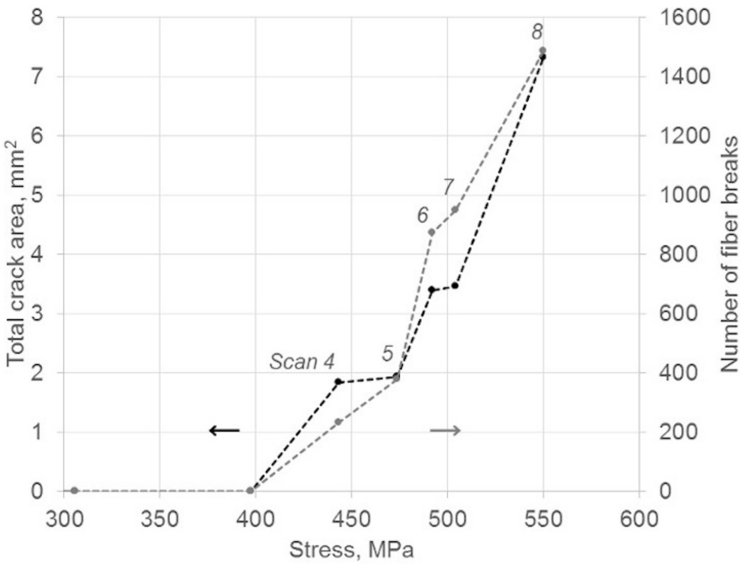

Figure 5.14 Total crack area and number of fiber fragmentations at each stress increment determined from x-ray tomography for unidirectional Specimen 1. The data is plotted to depict the quantification of the two types of damage mechanisms at each stress increment

Since matrix cracking results in high energy events, Figure 5.15a represents the comparison between cumulative AE energy and total matrix crack area at each stress increment which shows a strong linear trend over the entire test with an intercept close to zero. This suggests that AE energy is directly proportional to transverse matrix crack area. Although matrix cracking produces high energy events, there is often a greater number of low energy, high frequency events detected by AE in these composites due to fiber fragmentations. The comparison of cumulative number of AE events with the number of fiber breaks is shown in Figure 5.15b and shows a strong trend, although the trend is nonlinear indicating an increase in sensitivity of AE to fiber fragmentations throughout the test. A strong trend is observed from Scan 5 (475 MPa) onward showing the sensitivity of AE to fiber fragmentations. This increase in sensitivity to fiber fragmentations corresponds to the end of matrix cracking but the continuation of fiber fragmentations and as a result the low energy fiber fragmentation events are not competing against the high energy matrix cracking events within the AE sensors. At the last scan, the number of AE events corresponded to about 40% of the number of fiber breaks.

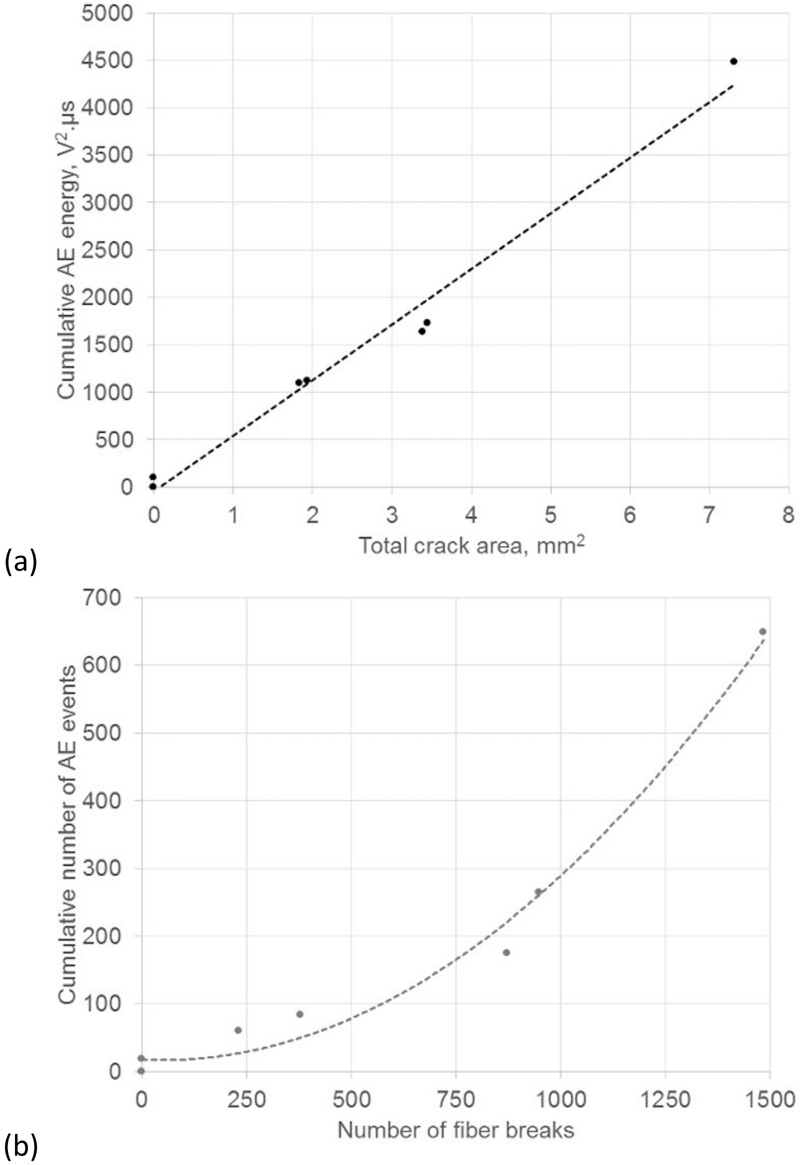

Figure 5.15 (a) Cumulative AE energy vs. total matrix crack area for unidirectional Specimen 1 (b) Cumulative number of AE events vs. number of fiber breaks for unidirectional Specimen 1

5.5.3 AE Measurements for Cross-ply Specimen

As with the unidirectional specimens, the damage quantified using x-ray CT was used to compare to the obtained AE data. The total matrix crack area and the total number of fiber breaks detected at each stress increment is presented in Figure 5.16. However, these values for the crack total crack area at each stress increment and the number of fiber fragmentations at each stress increment can be compared to the cumulative AE energy and cumulative number of AE events respectively.

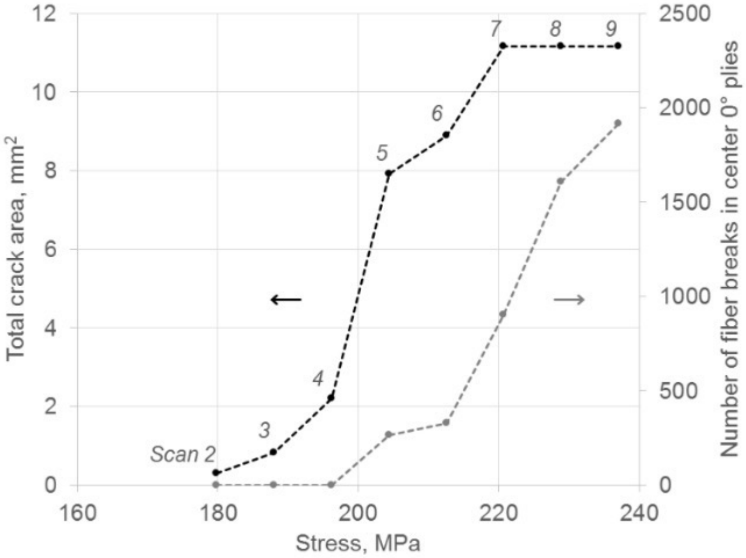

Figure 5.16 Total matrix crack area and number of fiber fragmentations at each stress increment determined from x-ray tomography for cross-ply Specimen 1

The cumulative AE energy at each stress increment in comparison to the total matrix crack area is shown in Figure 5.17a. It was difficult to extract a meaningful trend in this case because most of the energy observed from matrix cracking, i.e. the onset of cracking occurred over a narrow stress range (195 to 212 MPa) between two scans. Note, however, that the significant increase in crack area between Scans 4 and 5 was accompanied by a significant release of AE energy. Moreover, very limited AE energy was recorded between Scans 7 and 9 (229 MPa - 246 MPa) during which no matrix crack growth was observed. Cumulative AE events and the number of fiber fragmentations in the center longitudinal plies are compared in Figure 5.17b. It is worth noting, however, that only a small fraction of fiber breaks was detected. Assuming that a similar number of fiber breaks was present in the surface longitudinal 0° plies (not measured), only about 10% of fiber breaks were detected by AE.

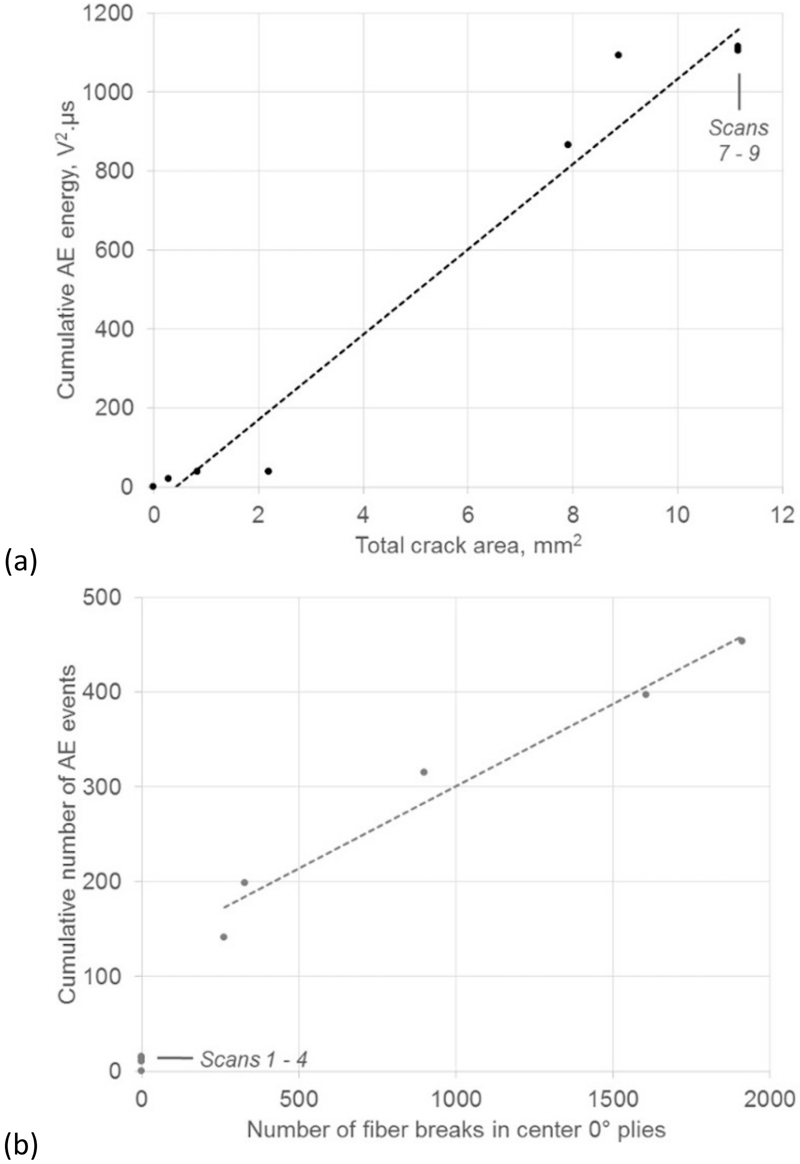

Figure 5.17 (a) Cumulative AE energy vs. total crack area for cross-ply Specimen 1 (b) Cumulative number of AE events vs. number of fiber breaks for cross-ply Specimen 1

5.5.3 Comparison of Damage Evolution in Unidirectional and Cross-ply Specimens

When comparing the damage between the unidirectional and cross-ply specimens, one of the major differences between the two is the way in which the damage evolved. For both architectures, initial matrix cracking was always observed before initial fiber fragmentations were detected. The cumulative AE energy compared to the cumulative number of AE events, including both high and low energy events, is shown in Figures 5.18a and 5.18b for the unidirectional and cross-ply specimen respectively. For the unidirectional specimen the overall AE activity was characterized by few high-energy events (matrix cracking) separated by large number of low-energy events (fiber fragmentations). Very limited activity was recorded during each scan at fixed crosshead displacement. The general trend observed for the unidirectional specimen was that the fiber breaks appeared over a timescale similar to that of the matrix cracks which is why the cumulative AE energy and the cumulative AE events increase at approximately the same rate at each stress increment or each scan shown in Figure 5.18a. It can be observed at scan 8 that there is only a minimal increase in AE energy but a large increase in the cumulative number of AE events. From the micro-CT it was observed that at this stress increment (550 MPa) there was no additional matrix cracking but a large increase in the number of fiber fragmentations which account for the increase in the cumulative number of AE events. After scan 8 in Figure 5.18a, there is a drastic increase in the cumulative AE energy most likely in relation to failure of the composite. As the composite fails, fibers will continue to break and as a result the cumulative number of AE events will increase. Overall, the overlap of few high-energy AE events with large numbers of low-energy AE events is in line with matrix cracking and fiber fragmentations occurring simultaneously throughout the test.

In comparison to the unidirectional specimen where fiber fragmentations and matrix cracking appeared in a more simultaneous manner, the damage mechanisms detected within the cross-ply specimen appeared in two distinct phases. The cumulative AE energy compared to the cumulative number of AE events for the cross-ply specimen is shown in Figure 5.18b. The first distinct phase was the initial matrix crack, Crack A, observed between scan 4 and 5 (230 MPa and 240 MPa) where the cumulative AE energy increased drastically to approximately 800 $V^2, \mu s$ while the number of total AE events recorded was less than 100 events. After the initial matrix crack there was a slight number of fragmentations detected in correlation with the first matrix crack shown by scan 5 in Figure 5.18b where the energy didn't increase but the number of total detected events increased to approximately 150 events. Next, Crack B, the second matrix crack, was detected between scan 5 and 6 (240 MPa and 250 MPa) where it can be seen that the cumulative energy increased by 300 $V^2, \mu s$. It is known from the micro-CT images that there were only two matrix cracks within the field of view. After the second matrix crack occurred there wasn't much of an increase in AE energy. However, the number of fiber fragmentations increased significantly as shown by the increase of cumulative number of AE events from 175 events to over 500 events between scan 6 and scan 9. The general behavior observed in the cross-ply specimen was that there were two distinct phases with a clear transition between the end of matrix-dominated damage phase and the beginning of the fiber-dominated damage phase leading to final failure.

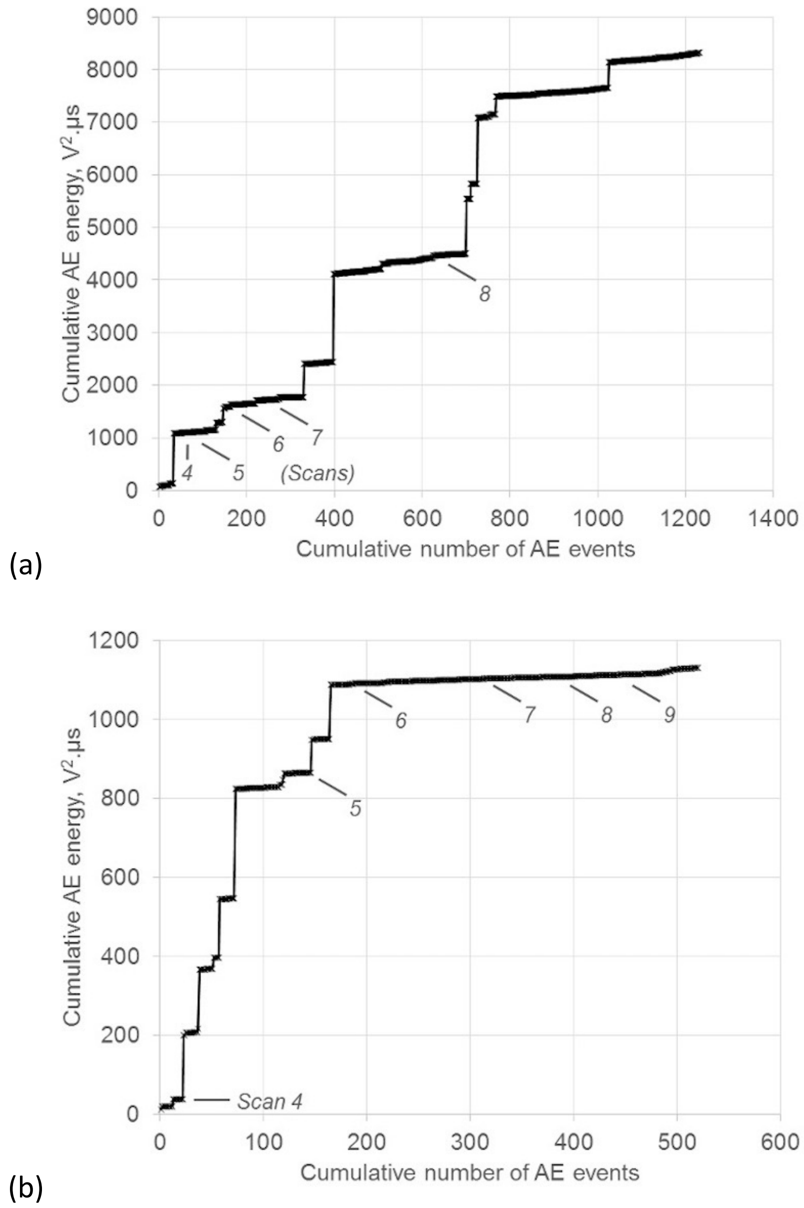

Figure 5.18 (a) AE results for cumulative number of AE events and AE energy vs. time for the unidirectional specimen (b) AE results for cumulative number of AE events and AE energy vs. time for the cross-ply specimen

The difference in the timescale for matrix cracking and fiber fragmentation in the two types of specimens is most likely due to the difference in stress on the fibers. Because matrix cracking occurred at higher composite stress in the unidirectional sample, stresses on fibers were high enough to cause fiber failures. The average fiber stress across a matrix crack can be estimated by dividing the applied composite stress by fiber volume fraction in the longitudinal direction. When the difference in fiber volume fraction in the longitudinal direction is considered (double in the unidirectional sample compared to cross-ply), stress on the fibers at onset of fiber failure and final composite failure are in excellent agreement between sample types.

5.6 Conclusion

Fiber fragmentations were quantified using micro-CT techniques in two separate cross-ply SiC/SiC CMC specimens. The damage evolution behavior was relatively similar between the two specimens although Specimen 2 experienced less damage than Specimen 1 even though it had a similar ultimate tensile strength. The location of the detected fiber fragmentations in each specimen were compared to the location of each matrix crack. In Specimen 1, the location of the initial fiber fragmentations were within 200 µm of the matrix crack but as composite stress increased, the number of detected fragmentations increased and their location in relation to matrix crack A increased to 300 µm with the most distant fiber fragmentation being measured at a distance 600 µm away from matrix Crack A. The behavior for fiber fragmentations in relation to each matrix crack in Specimen 2 was similar to that observed in Specimen 1.

The opening of the fiber fragmentation in each specimen were also measured and when comparing Specimen 1 and Specimen 2, the fiber break opening continued to increase for Specimen 1 with 80% of the fiber fragmentation openings detected at 246 MPa being measured with an opening of approximately 6.5 µm and the largest opening being detected at slightly greater than 25 µm. For Specimen 2, the measured openings didn’t significantly increase with composite stress and 80% of the openings were measured at 3 µm with the largest opening being measured at 11 µm. The discrepancy could be due to the crack failure outside the field of view and there a more detailed analysis in terms of where the field of view is located in relation to the failure crack would need to be performed. The fiber break openings in relation to the matrix crack opening for both of the cross-ply specimens appear, via qualitative visual comparison, more similar to those observed in the unidirectional specimen.

Lastly the damage observed and quantified using micro-CT was compared to the damage measured using acoustic emissions. These results could be used to support the development and validation of analytical models. Acoustic emission was able to reveal differences in damage progression between the unidirectional and cross-ply specimens. Strong empirical relationships were observed between matrix crack area and AE energy, as well as between number of fiber breaks and number of AE events. Also, a new graphical representation of AE data was proposed (cumulative energy vs. cumulative events), which has potential for real-time use to help identify the interplay between matrix cracking and fiber breaks.

Chapter VI. Fiber Failure in Groupings and Fiber Fragmentation Clustering in Comparison to Fiber Microstructure Distribution

6.1 Introduction: GE Research Developing Mechanical Model

It is known that fiber failure is a dominate damage mechanism in ceramic matrix composite systems. Because of this it is important to understand the distribution of the SiC fibers within the composite microstructure and the distribution of the subsequent fiber fragmentations under applied composite load. Engineers at GE Research (formally known as GE Global Research) are currently developing a mechanical model based on the stress distribution and failure process near a single matrix crack and the model is dependent on understanding how damage evolution correlates to the composite microstructure.[1] Using micro-CT imaging allows for a more in-depth comparison between the composite microstructure and the damage evolution through the volume of a CMC.

The motivation behind this work is to better under the microstructure and the evolution of fiber failures in a unidirectional CMC in order to provide more detailed inputs for a mechanical model under development by engineers at GE Research. This model is being developed in order to better predict tensile failure for the CMC systems where composite failure is controlled by fiber failure due to matrix cracking. The model scope is based on the stress distribution and fiber failure process near a single matrix crack. The model includes variability in fiber failure caused by variability in the microstructure and other constituent properties such as: fiber radius, fiber coating thickness, ineffective fibers, and fiber groupings.

6.1.1 GE Model Assumptions

The definition of fiber groupings is neighboring fibers that are touching in a SiC/SiC CMC as shown in Figure 6.1. The objective is to better understand how fibers within a fiber grouping behave. There are three separate assumptions regarding fiber groupings (i) each fiber within the grouping fails independently, (ii) if one fiber is ineffective, the entire grouping is ineffective, , (iii) if any fiber within the grouping fails, the entire grouping fails. Ineffective fibers are defined as fibers with discontinuous coatings, and/or a debond energy such that they would not debond around a matrix crack and would therefore be assigned a strength of zero in a matrix crack plane. Assumptions two and three result in a significant decrease in the ultimate tensile strength for high fractions of groupings and ineffective fibers, and results from assumption three differ from assumption two only for cluster fractions above 30%. Returning back to Figure 6.1, it can be seen that all of the fibers within the grouping broke on the same plane and there is very little pullout but it is unknown how these fibers behaved while under load, what their individual stress states were, and whether fibers fractured all at once, sequentially or without any correlation. Using the information obtained from the X-ray CT image datasets, a better understanding of the microstructure and the fiber fragmentations can be used to validate inputs for this model.

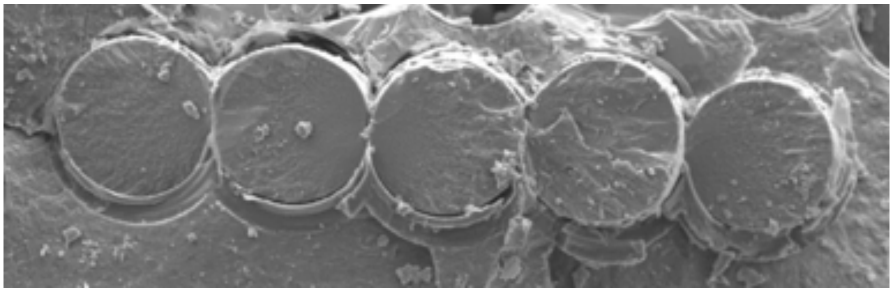

Figure 6.1 example of fiber grouping in CMC microstructure[1]

6.1.2 Chapter Layout and Organization

The layout describing the order in which the results will be discussed is shown in Figure 6.2. In order to understand fiber failure evolution, the initial fiber microstructure needs to be described. For that reason, the distribution of the fibers within the microstructure itself was studied and the average nearest neighbor distance for each individual fiber was measured. Next, the fiber *fragmentations* that were detected at 445 MPa and 550 MPa, as a result of applied tensile load to Specimen 1, were analyzed in several ways. First, the average nearest neighbor distance of each fiber fragmentation was compared to the average nearest neighbor distance of the intact fiber microstructure. Second, the fiber fragmentation datasets at two increments (the lowest and the highest applied stresses at which fiber fragmentations were detected) were further analyzed using a clustering workflow algorithm. This clustering workflow algorithm was utilized to determine if there were regions where fiber fragmentations appeared to be clustered when compared to the distribution of the fiber fragmentation of the entire volume. Lastly, any fiber fragmentations that were identified as being clustered by the clustering algorithm were then investigated further to determine if the fiber fragmentations identified as part of a cluster could also be defined as failing within a fiber grouping.

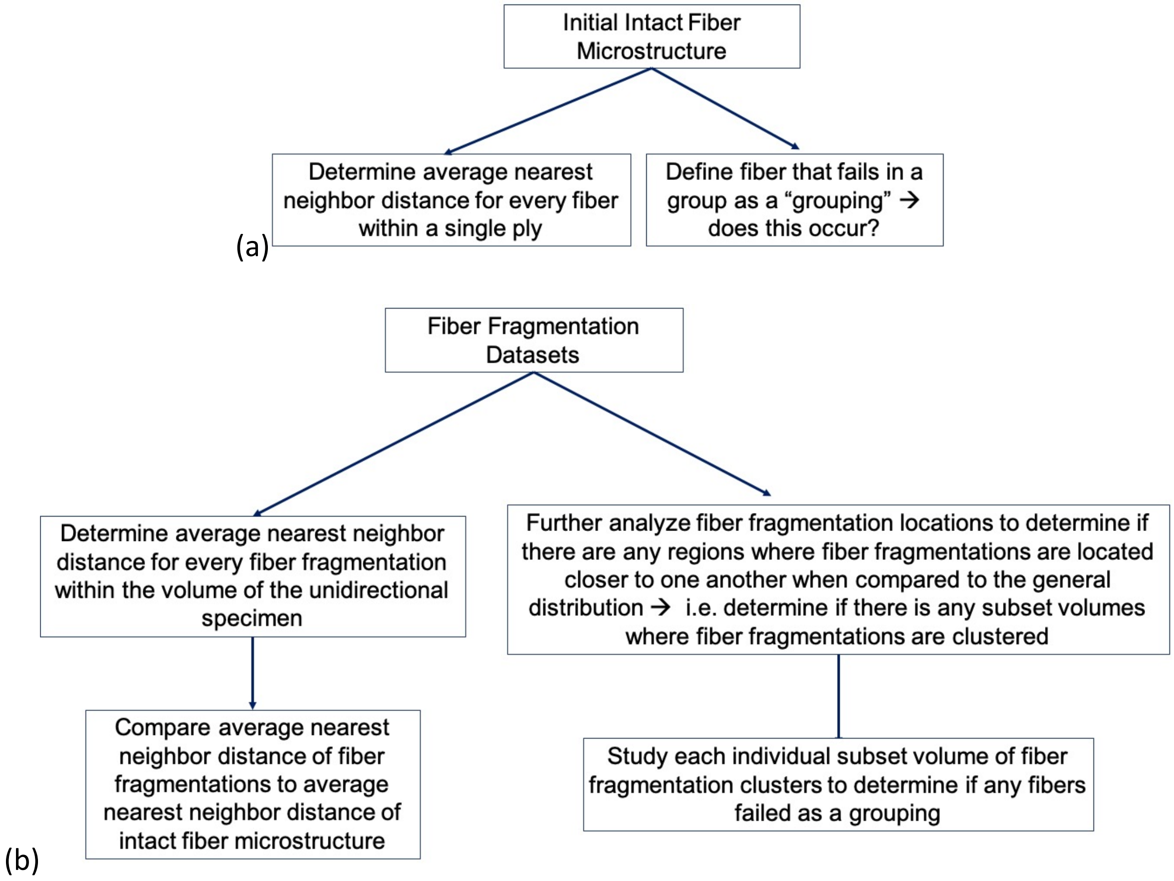

Figure 6.2 The order in which the results will be presented throughout this chapter for (a) the intact fiber microstructure and (b) fiber fragmentation analysis

6.2 Fiber Distribution of Composite Microstructure

The distribution of intact fibers that make up a single ply within a unidirectional specimen was determined using a single micro-CT slice from with the volume of an imaged specimen. Various image modifications such as image thresholding were performed on the image in ImageJ in order to use particle analysis to obtain the centroid of each fiber within the slice. The 2D slice that was utilized for fiber particle analysis is shown in Figure 6.3a and the final imaged used for particle analysis, post-thresholding, in ImageJ is shown in Figure 6.3b. In theory it would have been ideal to image an undamaged specimen in order to obtain and analyze the original, as manufactured, fiber microstructure. Unfortunately, an image of an undamaged specimen was not obtained and as a result the slice shown in Figure 6.3a is from a micro-CT dataset of a damaged specimen where the dark black “fibers” that are visible are holes where broken fibers have been pulled out. In order to understand the undamaged fiber microstructure and distribution it was assumed that all fibers were intact and unbroken. It should also be noted that although these specimens are made up of two plies, only a single ply (Ply 1) was taken into consideration when analyzing the location of these fibers. The area of the image was 0.33 mm^2 with a total of 250 fibers within the field of view.

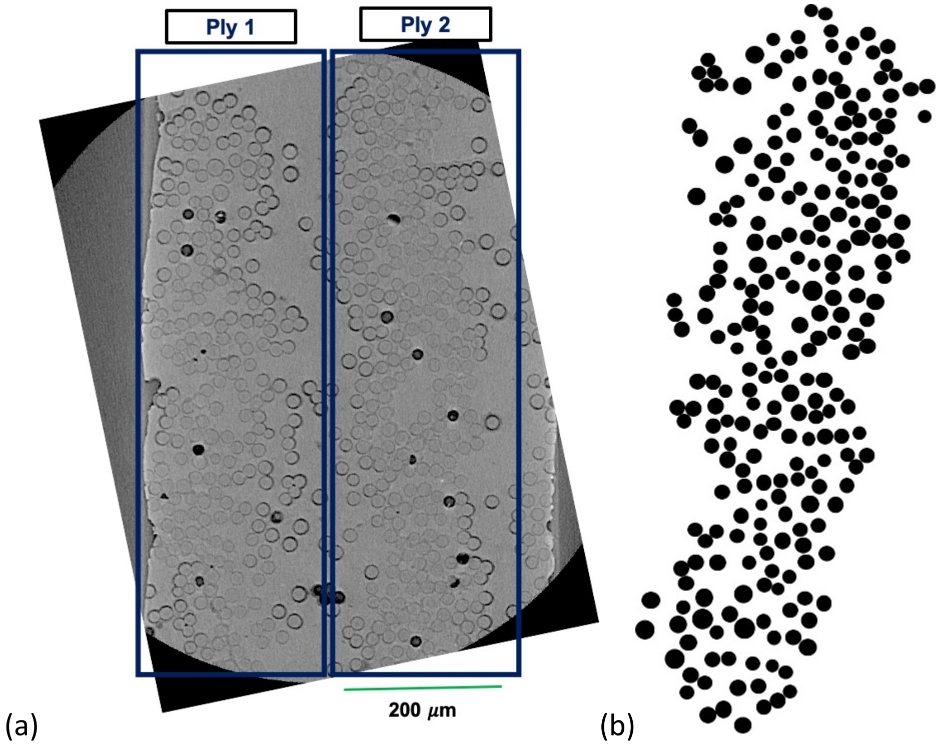

Figure 6.3 (a) x-ray CT slice depicting two plies, used for fiber analysis (b) threshold image of Ply 1 used for fiber analysis to determine nearest neighbor distances

Using particle analysis, the centroid for each fiber was determined and the nearest neighbor distance associated with each individual fiber was calculated using MATLAB. The average nearest neighbor for all 250 fibers was 31.4 ± 30.7 μm. The fiber diameters for each fiber are not equivalent but assuming the fibers have a diameter of 16 μm, then the smallest nearest neighbor distance possible for the fibers to actually be touching would be 16 μm.

The probability density of the nearest neighbors measured is shown in Figure 6.4 and it can be seen that the distribution is slightly non-uniform, pointedly at the low and high ends. These non-uniformities are due to two things: fiber tows and "isolated" fibers. Fiber tow groupings result from the way in which these melt-infiltrated composites were manufactured. For the melt-infiltration process, when the fibers are coated with BN, they are coated in bundles called tows that are approximately 1.14 mm in width and 0.19 mm in height and are usually made up of approximately 500 fibers. After the tows are coated, many of them are processed together to form a single ply. The fibers within each tow bundle are not distributed evenly throughout the layup and therefore the fibers in the final composite are often still grouped within their tows. This trend is evident when looking at the fiber coating of each individual fiber. The fibers that are located near the edge of the tow have a thick, well-defined BN fiber coating while the fibers located within the center of a tow have minimal fiber coating. In relation to the measured nearest neighbor distance for the microstructure, the probability of experiencing a nearest neighbor at the lower end of the distribution (20 μm - 30 μm nearest neighbor distance) is higher for the fibers within each tow where the BN interface coating is thinner. A high probability of large nearest neighbor distance is typically associated with "isolated" fibers which are fibers that end up in a denser matrix region and farther away from the ply. Figure 6.5 presents examples of isolated fibers within in the composite microstructure.

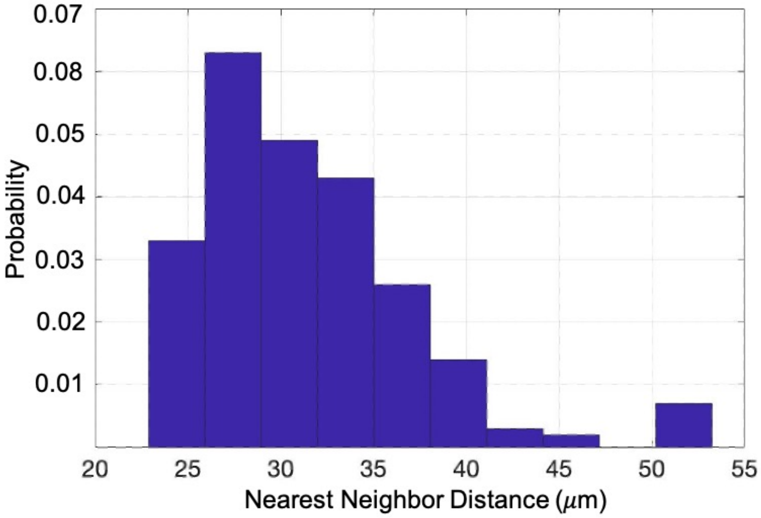

Figure 6.4 Nearest Neighbor Distance distribution in observed microstructure

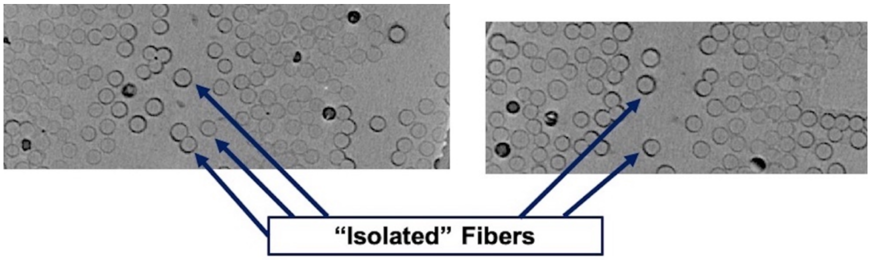

Figure 6.5 example of fiber microstructure with "isolated" fibers or fibers that occur outside of the assumed width of the ply.

Knowing the nearest neighbor distance for the fibers within the microstructure allows for an approximation of the distance required to define fiber grouping. To begin with, a fiber grouping will be considered fibers who have a nearest neighbor distance less than or equal to 31.4 μm since that was the average nearest neighbor distance for all of the fibers within the microstructure and a fiber grouping is considered fibers that are touching. Next, the fiber fragmentation data will be analyzed first by comparing the average nearest neighbor of the fragmentations, and then by determining if fibers failed as fiber groupings.

6.3 Average Nearest Neighbor of Fiber Fragmentation

The previous section detailed average nearest neighbor distance for the intact fiber microstructure within an X,Y plane because the fibers are continuous lines in the Z-direction. This next section will detail the observations of fiber fragmentations (fibers that broke while under load) within the unidirectional specimen in terms of nearest neighbor distance and clustering effects. The X,Y,Z centroids of the fiber fragmentations were obtained from segmentation techniques and were used to determine the nearest neighbor distance of each fiber fragmentation.

Logically, it is anticipated that at lower applied stress increments the average nearest neighbor distance will be greater accompanied by a larger deviation. This is due to fewer fiber fragmentations and the tendency of fiber fragmentations to occur near the plane of a matrix, as was shown in Chapter 3. Therefore, fiber fragmentations might occur very close to one another if both fragmentations occurred near the same matrix crack, but if another fragmentation was a result of a different matrix crack at a distant location then it will have a greater nearest neighbor distance. However, at higher applied stress increments, the matrix crack spacing becomes more uniform, and as a result it is expected that the fiber fragmentations will have smaller average nearest neighbor values along with decreased standard deviations. In theory when a composite specimen fractures, every fiber has failed and therefore the nearest neighbor distance for every failed fiber should be equivalent to that of the initial intact fiber microstructure.

The average nearest neighbor distances for fiber fragmentations detected at each stress increment (shown as % of Failure Stress) for unidirectional Specimen 1 and Specimen 2, are depicted in Figure 6.6 by the black diamonds and the green diamonds respectively. Overall, the results are comparable to the anticipated outcomes outlined above. At lower stress increments (70-80% of the failure stress), the average nearest neighbor distance was slightly less than 80 μm with large standard deviations. The average nearest neighbor distance continued to decrease, as did standard deviations as a function of applied stress. The average nearest neighbor distance at failure (100% of failure stress) in both specimens was reported as approximately 48 μm ± 13 μm which is slightly greater than the nearest neighbor distance measured for the intact fiber microstructure (31.4 μm ± 30.7 μm) depicted by the red square. For the failure stress the images used to determine nearest neighbor distance were taken away from the fracture plane and therefore the fracture plane itself was not taken into consideration since 100% of the fibers would have been broken. The entire gauge length of the tensile specimen was not imaged and therefore not every fiber failure was detected but the nearest neighbor distance at failure was close to the expected intact microstructure. There also appeared to be a linear decrease for the average nearest neighbor distance as composite stress increased.

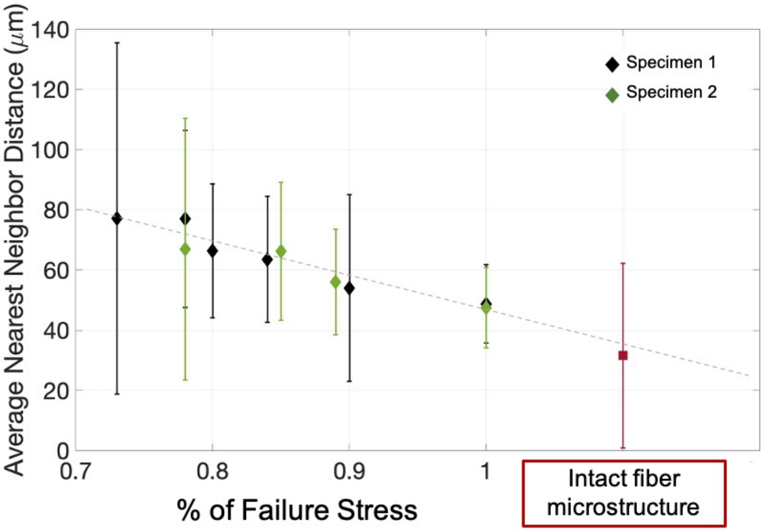

Figure 6.6 Average nearest neighbor distance and standard deviation for all of the fiber fragmentations detected at each stress increment for Specimen 1 and Specimen 2. The red datapoint represents the nearest neighbor distance for the intact fiber microstructure

General observations from the overall fiber fragmentation nearest neighbor distances suggest that there doesn't appear to be any severe fiber clustering and it is apparent that the if fibers are failing as fiber groupings then the number of failed fiber groupings is most likely relatively small. However, a more in depth examination of fiber fragmentation datasets is needed to understand if any clustering occurred and to determine if fibers failed in fiber groupings.

6.4 Analysis of Fiber Fragmentation Clustering and Fiber Failure Grouping

The large number of fiber fragmentations detected at 550 MPa, 3000 breaks, results in a large dataset to work with when looking at various nearest neighbor distances. In order to help decrease processing time and complexity, the fiber fragmentation datasets were analyzed using a clustering workflow algorithm to determine if there were subset regions within the volume of the specimen where fiber fragmentations appeared more clustered, or had smaller nearest neighbor distances, when compared to the rest of the fiber fragmentation population. It is important to note here the difference between clustering and grouping. A fiber grouping are fibers that are actually neighbor and near each other in the microstructure that fail as a grouping whereas clustering is a group of fiber fragmentations that appear closer together, or more clustered, when compared to the rest of the fiber fragmentation locations. The fiber fragmentations that are considered part of a cluster will be further analyzed to determine if the fiber fragmentations are actually grouping.

Finding clusters within the fiber fragmentation data serves two main purposes. First, establishing which fiber fragmentations are clustered can reduce the number of fragmentations that can be possibly considered as failing in fiber groupings. If the nearest neighbor distance between two fiber fragmentations is not small enough to be considered a cluster, then it can be assumed that the nearest neighbor distance is too small for either fiber fragmentation to be considered part of a fiber grouping as well. Second, clusters of fiber fragmentations could indicate areas where more damage is occurring within a subset volume of the composite specimen and could be used in future work for mechanical model predictions.

6.4.1 Clustering Workflow Algorithm

A clustering workflow algorithm was developed at the University of Michigan for identifying clustering of atoms within atom probe tomography datasets by Ghamarian and Marquis.[2] The clustering workflow algorithm was used to obtain information from fiber fragmentation datasets pertaining to whether clustering of fiber fragmentations occurred within the volume of the specimen. A detailed description of the workflow and example data sets can be found in Ghamarian and Marquis's body of work and the developed code for their study is available online.[3] The general method of the workflow applies hierarchical clustering and classification algorithms to determine if clusters are present.[4-5] This is determined by finding the maximum connected components of the high density regions associated with the probability density function representing the distribution of fiber fragmentations in a dataset. Thus, clusters were defined as regions in which the ratio between the probability that a group of neighboring fiber fragmentations forms a cluster and the volume of this cluster is large.

The main process for the algorithm uses hierarchical density-based spatial clustering of applications with noise (HDBSCAN).[5] In HDBSCAN, a distance metric is introduced, designated as the core-distance, and is defined as the distance from a fragmentation to its *k*th nearest neighbor. Another metric, the mutual reachability distance is utilized to determine outliers. Figure 6.7 is taken from Ghamarian and Marquis[2] and describes the process of determining both the core distances and the mutual reachability distance for three points (X_1, X_2, and X_3) within a dataset (Figure 6.7a) where k was set equal to 4. The core distance for points X_1 and X_2 shown in Figure 6.7b is depicted by blue and green arrows respectively while the actual distance between these two points is shown by a double-sided purple arrow. Since the actual distance between these two points is larger than their core-distance values, the mutual reachability distance is equivalent to the real distance between X_1 and X_2. In contrast, the mutual reachability distance between points X_1 and X_3 is equal to the core-distance of X_3 as shown in Figure 6.7c and thus, point X_3 is considered an outlier. These distance metrics are used as parameters in order to identify clustering.

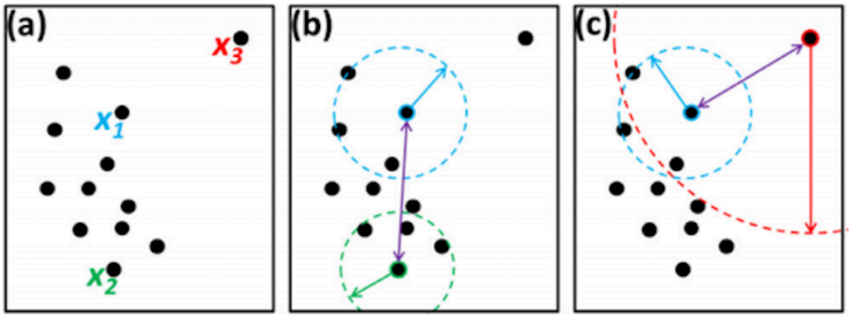

Figure 6.7 (a) A 2D distribution of points. Mutual reachability distance for (b) points X_1 and X_2 and (c) point X_2 and X_3 with *kth* nearest neighbor set to 4. Image taken from Ghamarian and Marquis manuscript[2]

6.4.2 Clustering Within Fiber Fragmentation Datasets

The clustering workflow algorithm at the University of Michigan was used to detect regions where clustering of fiber fragmentations occurred within the volume of the specimen. The clustering algorithm was utilized for fiber fragmentation datasets obtained at two different stress increments. The stress increments of 445 MPa and 550 MPa were chosen because they were the lowest and highest stress increment at which fiber fragmentations were detected. Note that these two datasets were run through the algorithm independently and the clustering data from one dataset is in no way dependent or connected to the results from another. For example, the algorithm determines clusters based on the *k*th nearest neighbor where for these datasets, *k* was set to 5. So for the fiber fragmentations at 445 MPa, there may be fiber fragmentations that are considered clustered based on their nearest neighbor distances but these same fiber fragmentations at the same location in the dataset at 550 MPa will most likely not be considered part of the same cluster or possibly part of any cluster due to new fiber break locations changing the location and distance of the *k*th nearest neighbor. All of the work presented in relation to this clustering work flow analysis was obtained from unidirectional Specimen 1.

The clustering algorithm recognized a total of four clusters, or four regions, where the fiber fragmentations distances from one another were closer together, i.e. clustered, compared to the distance of fragmentations experienced by the general population within the volume at 445 MPa. The number of clusters detected at 550 MPa using the clustering algorithm was 17 clusters. The number of fiber fragmentations within each identified cluster at either stress increment varies. Figure 6.8 plots the number of fiber fragmentations within each cluster at each stress increment of 445 MPa and 550 MPa. Figure 6.8 and is not plotted as a function of stress but rather to provide information about each cluster at each individual stress increment. Each cluster detected at 445 MPa is depicted by a red diamond where it can be seen that the smallest cluster consisted of 10 fragmentations, while the largest cluster consisted of 32 fragmentations. At 550 MPa, each cluster is depicted by a green diamond in Figure 6.8 where the average number of fiber fragmentations in a cluster was 20 fragmentations with the largest cluster containing a total of 51 fragmentations.

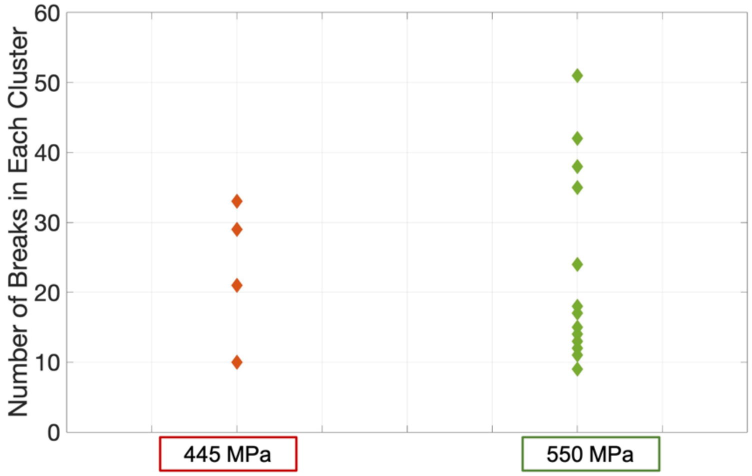

Figure 6.8 the number of fiber fragmentations that were identified as part of each detected cluster at each analyzed stress increment

The centroid of each detected cluster for each stress increment is plotted in Figure 6.9. The four clusters that were detected at 445 MPa are relatively close to clusters that were detected at 550 MPa. According to global load sharing, once a fiber fails within the composite, the load that the fiber was carrying before fracture is distributed equally to the remaining intact fibers. This load redistribution should maintain conditions such that the next fiber failure location should be dependent solely on the stochastic strength of the fibers themselves. However, the clustering observed at an applied stress of 445 MPa, and the additional clustering within the same vicinity at 550 MPa, seem to indicate either true global load sharing is not occurring or that global load sharing is combined with some form of local load sharing. Local load sharing causes the load to increase locally when one fiber fails, making a failure of nearby fibers, and hence clustering, more likely. Persistence, or growth, of clusters as stress increases would support an argument for local load sharing in these CMCs. Additional analysis of these data sets for cluster persistence or growth would be beneficial for future model development.

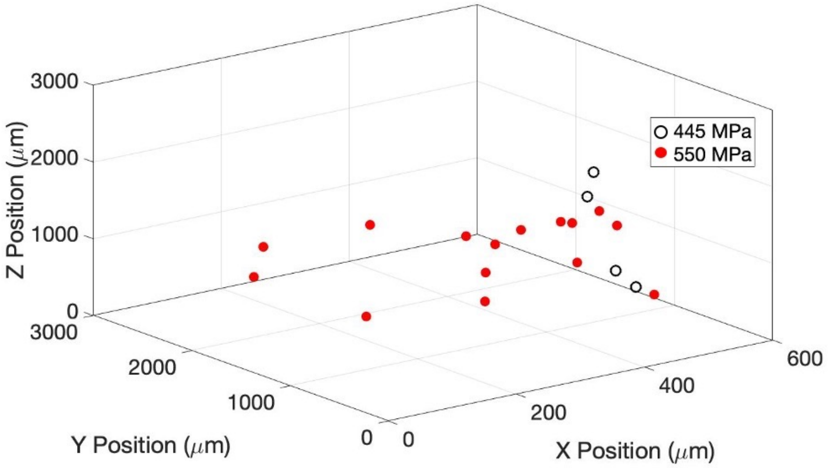

Figure 6.9 the centroid location of each cluster detected at 445 MPa (open black circles) and 550 MPa (filled red circles).

The clustering algorithm assisted in narrowing down the number of possible fiber fragmentations that might have failed in fiber groupings. However, the algorithm only determined if points in space are located closer together in comparison to other points in space and did not actually determine if fibers failed as a fiber grouping. Therefore, it is necessary to further examine the fiber fragmentations that were considered part of a cluster to determine if fiber fragmentations identified as clusters are actually clustered, i.e. do they have a closer nearest neighbor distance than the original undamaged microstructure. The clusters will be studied to determine if there is any overlap in fiber cluster results from the original microstructure and the fiber break cluster results to try and determine if fibers fail in groupings.

6.4.3 Verification of Clustered Fiber Fragmentations and Determine if Fibers Failed in Groupings

Now that the fiber fragmentations dataset for each stress increment has been analyzed using a clustering workflow algorithm, the average nearest neighbor distance for the fiber fragmentations within each individual cluster will be measured and compared to the initial nearest neighbor distance for the entire fiber fragmentation dataset previously presented. If the fiber fragmentations within the cluster are truly “clustered” then the fiber fragmentations that are a part of a cluster should have a smaller nearest neighbor distance, and deviation, when compared to the entire fiber fragmentation dataset.

The average nearest neighbor distance for each fragmentation in both the full set of fiber fragmentations and the detected cluster, at each stress increment of 445 and 550 MPa, is shown in Figure 6.10. The average nearest neighbor distance for each cluster at 445 MPa (depicted as blue circles) varied but in general the nearest neighbor distance for each cluster detected at 445

MPa was approximately 57 μm ± 21 μm. The average nearest neighbor distance for all of the detected fiber fragmentations within the entire dataset at 445 MPa (depicted as the black square) was 77 ± 58 μm. Both the nearest neighbor distance and deviation measured for all of the detected clusters are smaller than the overall nearest neighbor distance for the entire dataset of fiber fragmentations at 445 MPa. This confirms that the regions perceived as clusters by the algorithm are actually regions where nearest neighbor distances are less than other regions.

At 550 MPa, the average nearest neighbor distance for all of the 17 detected clusters ranged from 25 – 48 μm (depicted as yellow circles). The average nearest neighbor distance and deviation for the identified clusters was 40 ± 9 μm. This average nearest neighbor distance for the clusters is approximately 15 μm smaller than the average nearest neighbor distance for all of the fiber fragmentations detected at 550 MPa (depicted as green squares) and the corresponding deviation for the clusters is extremely small. Both of these factors suggest that most of the fiber fragmentations identified by the algorithm as part of a cluster at 550 MPa were indeed clustered in comparison to the distribution of all of the fiber fragmentations detected at 550 MPa.

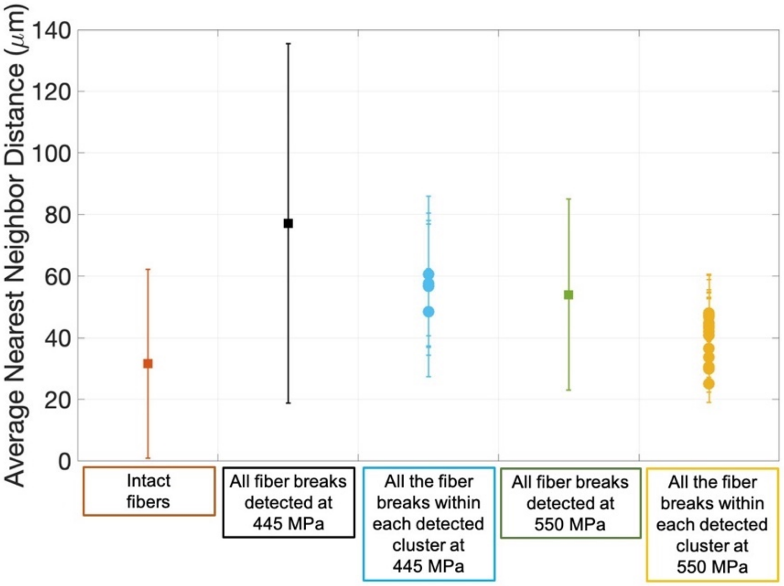

Figure 6.10 Average nearest neighbor distances measured for: the fiber microstructure (depicted by the red square), the entire fiber fragmentation dataset at 445 MPa (depicted by the black square) and 550 MPa (depicted by the green square), and the fiber fragmentations that were identified as part of a cluster at 445 MPa (depicted by the blue circles) and at 550 MPa (depicted by the yellow circles)

Although it is apparent that the fiber fragmentations that were identified as part of a cluster within each stress increment dataset are more than likely actually “clustered” closer together, it is less apparent that these clusters directly correspond to fiber groupings. Recall, the model identified failure of a group of fibers detrimentally impacting strength. Also recall that a fiber grouping was defined as any two fibers or fiber fragmentations that have a nearest neighbor distance of 31.4 μm, or less as determined from the intact fiber microstructure. Based on this definition, the fiber fragmentations that were considered part of each cluster at 445 MPa are more than likely not fiber failures that failed as fiber groupings. The average nearest neighbor distance for the clusters at 445 MPa is approximately 20 μm larger than 31.4 μm and even the standard deviation is barely within the range of what is considered a fiber grouping. At 550 MPa it is probable that at least a few of the clusters identified within the volume are fiber fragmentations that failed as fiber groupings. By comparing solely the average nearest neighbor values, at least four of the identified 17 clusters have nearest neighbor values that are less than 31.4 μm. However, taking the standard deviation into consideration it is possible that even more clusters could also be considered fiber groupings. Future work should be done in order to compare the centroid of these clusters to the location within the 3D dataset to confirm whether the fibers fragmentations correspond to fiber groupings.

One of the objectives of this work was to provide information about the number of fibers that failed as fiber groupings as this can affect the mechanical model for specimens that observed large amounts of fibers that fail as fiber groupings. For the fiber fragmentations detected at 445 MPa, it was determined based on the clustering information that there were few to no fibers that failed as fiber groupings. At 550 MPa, it was determined that some fibers failed as fiber groupings, but exactly how many is unclear. However, a number can be estimated by assuming that every fiber fragmentation that was identified by the algorithm as being part of a cluster also failed as a fiber grouping. In total there were 341 fiber fragmentations in the 17 clusters identified at 550 MPa. These 341 fiber fragmentations made up only 15% of the total number of detected fiber fragmentations and only 11% of the total number of fibers within the composite specimen. Therefore, from this very preliminary study, even if all of these clustered fiber fragmentations failed as a fiber grouping, the effect of these groupings is limited in relation to the mechanical model. Further work is needed to determine if a single fiber failure within a grouping results in the remaining intact fibers continuing to carry the load or causes those fibers to become ineffective.

6.5 Conclusion

Preliminary work was done to study the distribution of the SiC fibers within the SiC matrix and to quantify clustering in the as-processed microstructure via a nearest neighbor distance. The nearest neighbor distances for the intact fiber microstructure were compared to nearest neighbor distances of detected fiber fragmentations at increasing stress increments in order to better understand the in situ fiber failure process under applied tensile load. Clustering of fiber fragmentations was identified at 445 MPa and 550 MPa via a clustering algorithm and through comparison of nearest neighbor distances between the full fiber fragmentation dataset and possible clustered subsets. The clustering at 445 MPa more than likely did not correlate to fibers failing as a fiber grouping. At 550 MPa, directly before failure, there were 17 clusters detected that had average nearest neighbor distances similar to that of the intact fiber microstructure. This indicated that the fiber fragmentation within these clusters probably did correspond to fibers failing as a fiber grouping. The effect of these clusters on damage progression was most likely limited. Assuming that all 341 fiber fragmentations in the clusters identified using the clustering algorithm were actually fibers that failed as a fiber grouping, those fiber fragmentations only make up 15% of the total number of fiber breaks and 11% of the total number of fibers within the volume. As a result, it was determined that fibers that fail as an entire fiber grouping do not contribute to the damage model in a significant way.

References

1. E. Maillet* 1 ; D. Dunn1, “Microstructure-based modeling of the ultimate tensile strength of ceramic matrix composites” Presentation: ICACC-S1-057-2018
2. Ghamarian I, Marquis EA. Hierarchical density-based cluster analysis framework for atom probe tomography data. Ultramicroscopy 2019;200:28-38.
3. E.A. Marquis, https://github.com/emarq/HDBSCAN_DeBaCl_APT_V1_Public/, (2019).
4. B.P. Kent, A. Rinaldo, T. Verstynen, DeBaCl: a Python package for interactive DEnsity-BAsed CLustering, arXiv:1307.8136 (2013).
5. L. McInnes, J. Healy, S. Astels, HDBSCAN: hierarchical density based clustering, J. Open Sour. Softw. 2 (11) (2017) 205.
6. E.A. Marquis, https://github.com/emarq/HDBSCAN_DeBaCl_APT_V1_Public/, (2019).
7. B.P. Kent, A. Rinaldo, T. Verstynen, DeBaCl: a Python package for interactive DEnsity-BAsed CLustering, arXiv:1307.8136 (2013). [36] J.A. Hartigan, Consistency of single linkage for high-density clusters, J. Am. Stat. Assoc. 76 (374) (1981) 388–394.
8. L. McInnes, J. Healy, S. Astels, HDBSCAN: hierarchical density based clustering, J. Open Sour. Softw. 2 (11) (2017) 205.

Chapter VII. Summary, Conclusion, and Future Work

Ceramic matrix composites, specifically SiC/SiC CMCs are currently being utilized in hot sections of gas turbine engines due to their high temperature capabilities and improved toughness. Many theoretical mechanical models have been developed to predicted damage evolution within these composites. However, due to their complex microstructure it is often difficult to experimentally validate these models. This dissertation presents experimental results for various damage mechanisms within two SiC/SiC ceramic matrix composite architectures as outlined below

1. Unidirectional Specimens: matrix cracking observations
    - Matrix cracking evolution was detailed for two unidirectional specimens as a function of applied stress.
    - The matrix crack planes were non-linear and often showed bifurcations. Most mechanical models assume a linear matrix crack plane
    - Some matrix cracks observed never extended through the width or thickness of the entire specimen. This differs from assumptions that matrix cracks occur instantaneously through the entire specimen
    - The onset of matrix cracking in these unidirectional specimens was compared to three well-known mechanical models. The matrix crack

observations compared relatively well to two models; one that considered interfacial sliding stress and one that considered debonding mechanisms. It is most likely that both interfacial sliding stress and debonding mechanisms are occurring and an improved model would need to be developed to incorporate both mechanisms.

2. Unidirectional Specimens: Fiber Fragmentation Observations
    - It is known that fiber failures occur but damage observations are often made by surface microscopy techniques which requires polishing a specific face of the specimen which damages the fibers making it difficult to capture the fiber fragmentations
    - This is one of the first reports to quantify fiber fragmentation positions, distributions, and sizes within an entire volume of a specimen.
    - The number of fiber fragmentations was quantified and appeared to increase linearly with applied stress.
    - Fiber fragmentations occurred in correlation to matrix cracking. It was determined that most fiber fragmentations occur with 200 um of a matrix crack which compared well to predicted values
3. Cross-ply Specimens: matrix cracking
    - The onset of matrix cracking in the form of “tunnel” cracks was observed for each specimen and the matrix crack evolution was detailed.
    - The stresses at which the onset of matrix cracking occurred, matrix cracking extension into longitudinal plies, and the composite failure were determined. All

values compared well to predicted stresses and to previously published experimental results

- The matrix crack opening, or crack opening displacement, was observed to be larger for the cross-ply specimens than in the unidirectional specimens.

4. Cross-ply Specimens: fiber fragmentations
    - The fiber fragmentation observations were similar to those observed in the unidirectional specimen in terms of opening and distance from corresponding matrix cracks
    - The fiber break distances from a matrix crack and calculated debond lenghs were compared. From the comparison it was suggested that the distance of a fiber fragmentation from a matrix crack plane could compare well to debond length which could be studied in future work
    - The fiber fragmentation openings qualitatively compare well to the matrix crack opening when the matrix crack is singular and no bifurcations are present but a more quantitative study is needed for a more direct comparison.
5. Fiber Fragmentation Clustering
    - The objective was to determine if fibers fail within fiber groupings. From preliminary results, it was determined using nearest neighbor distance and a clustering workflow algorithm that only a minimal number of fibers could have possibly failed within a fiber grouping

- The number of fibers that failed as a fiber grouping was small enough that it was concluded that effect of fibers failing as fiber groupings is negligible and can be ignored in mechanical modeling of these CMCs.

6. Future Work

- The quantifications of fiber fragmentations can be used for future work regarding the mechanics of these CMCs
  - The quantifications can be used for statistical significange for the input for mechanical models
- Oxidation Modeling
  - The quantification of matrix cracks both in the unidirectional and cross-ply specimens can be used as inputs in terms of surface area in relation to where oxygen can infiltrate into the specimen.
  - The observations of the non-linearity of the matrix cracks is also useful in terms of oxidation modeling where many of the oxidation models assume linear cracks.
  - The fiber break opening values and the location of fiber fragmentations will be on of the most useful inputs into for oxidation models. In current oxidation models for CMCs, fiber fragmentations are not taken into consideration. However, using the data obtained from this work, the location of fiber fragmentations within a specimen, and an estimate of their surface area can now be used for inputs.
- Future Micro-CT work

  - It would be useful to do more in situ micro-CT work including high temperature in situ testing. High temperature in situ micro-CT testing could be used to help validate the oxidation models and to visually quantify the combination of oxidation and mechanics of the CMC.
- UHT-CMCs: Ultra High Temperature – CMCs
  - Understanding the mechanics and oxidation of SiC/SiC CMCs is important in order to extend the research into ultra high temperature ceramic matrix composites for hypersonic applications